



UNIVERSITÀ DEGLI STUDI DI MILANO
FACOLTÀ DI SCIENZE E TECNOLOGIE

Physics Department

**LOCALIZATION AND ERGODICITY IN THE
DISCRETE NON-LINEAR SCHRÖDINGER
EQUATION**

Internal Supervisor:
Prof. Sergio CARACCILO

External Supervisor:
Prof. Antonello SCARDICCHIO

Candidate:
Carlo VANONI
Matr. n. 939430

A.Y. 2019-2020

Abstract

Since the pioneering works of Fermi, Pasta, Ulam and Tsingou [1], it is known that the presence of non-linearities contrasts equipartition of excitation energy. Instead, Many-Body localization provides a generic mechanism for the failure of thermalization in many-body quantum systems, despite the presence of non-linear interactions that tend to thermalize the system.

It has been recently demonstrated [2] that classical models described by a Non-Linear Schrödinger Equation on a lattice (DNLSE) display a localized phase. This localization phenomenon manifests itself as a condensation of a finite fraction of the energy on few lattice sites, giving rise to localized excitations, called breathers. This phase is described by non-Gibbs states, which means that standard statistical mechanics is no more valid: the equivalence between statistical ensembles does not hold.

This thesis work has a dual purpose: the first one is to investigate the presence of non-Gibbs states in the Josephson Junction Array model [3] with periodic boundary conditions. This system is described by equations similar to the DNLSE and is currently of interest due to its possible applications in the fields of metrology and quantum information. Our second aim is that of investigating the persistence of such localized phase also in the quantum regime of the DNLSE, i.e. in the Bose-Hubbard model, and if such localization phenomenon in the quantum regime is stronger or weaker compared to the classical case.

These purposes are pursued using both analytical and numerical techniques: in particular, a novel geometrical picture representing the phase space of our systems is introduced. This allowed us also to develop a stochastic numerical model adapt for the study of the DNLSE both in its classical and quantum regimes.

To my family

"Most people who haven't been trained in physics probably think of what physicists do as a question of incredibly complicated calculations, but that's not really the essence of it. The essence of it is that physics is about concepts, wanting to understand the concepts, the principles by which the world works."

Edward Witten

Contents

1	Introduction	1
1.1	Anderson and Many-Body Localization	1
1.2	Non-linear systems	5
1.3	Outline	7
2	A review of the most recent results	9
2.1	Non-Gibbs states and Ergodicity Breaking	9
2.2	The classical Discrete Non-Linear Schrodinger Equation	10
2.2.1	The microcanonical partition function	12
2.2.2	Analytic properties of the partition function	14
2.2.3	<i>Matching</i> regime: the non-analytic contribution	17
2.3	The Josephson Junction Array	21
3	A closer look at the JJA and the DNLSE	23
3.1	Classical Lagrangian for the DNLSE	24
3.2	Inverse participation ratio	25
3.3	The JJA grand-canonical partition function	26
3.4	Geometric construction	29
3.5	Upper and lower bounds to the total energy for the DNLSE	35
3.5.1	Modified lower bound with hopping contribution	36
3.6	The particular case $N = 3$	36
4	Quantum DNLSE	39
4.1	Symmetries, basis vectors and Hilbert space	40
4.2	The Quantum dynamics	42
4.2.1	The $N = 3$ case	42
4.3	Quantum tunnelling	44

CONTENTS

4.3.1	Classical trajectories	46
4.3.2	Quantum Tunnelling: the general case ($Q \gg 1$)	49
4.4	$N = 2$ quantum dynamics	52
4.4.1	Leading contribution to the tunnelling time τ	54
4.4.2	Inference of the Q and t dependence of τ/τ_{sc}	56
5	A stochastic model for the DNLSE	60
5.1	Classical stochastic model results	63
5.2	Quantum stochastic model results	67
5.2.1	Varying \hbar	68
5.3	Universality	73
5.3.1	Interpretation of the results	78
6	Conclusions and outlooks	79
7	Acknowledgements	81
A	Large Deviation Principle	82
B	Saddle Point Method	84
C	Condensation Phenomena from the Large Deviation Theory	86
C.1	Zero Range Process	86
C.2	Condensation in models with factorisable steady state	87
C.3	Interpretation as sum of Random Variables	89
D	Generation of the basis elements for the Quantum DNLSE and the Hamiltonian	90
E	Reflection above a barrier	94
F	Microcanonical random variables	97
F.1	An application	97

List of Figures

1.1	Thermalization vs Many-Body Localization	2
1.2	Anderson model for the localization transition	3
1.3	Diffusion vs Anderson Localization	3
1.4	Diffusion coefficient	4
2.1	DNLSE equilibrium phase diagram	11
2.2	Analytic structure of the partition function of the DNLSE	16
2.3	Josephson Junction Array setup	21
3.1	Inverse participation ratio	26
3.2	Variable space 2D and 3D	30
3.3	Variable space 4D connected	31
3.4	Variable space 4D disconnected	31
3.5	JJA variable evolution	34
3.6	Variable space DNLSE vs JJA	34
3.7	DNLSE solution of the equations of motion for different values of the hopping strength	38
4.1	IPR Bose-Hubbard	43
4.2	IPR vs occupation number Bose-Hubbard	44
4.3	IPR period in function of the hopping strength	45
4.4	Classical trajectories 2-site Bose-Hubbard hamiltonian	47
4.5	Classical trajectory 2-site Bose-Hubbard limiting case	49
4.6	Quantum tunnelling	50
4.7	Transition amplitude in function of time	53
4.8	Semi-classical transition time	55
4.9	Semi-classical transition time theoretical vs simulation	57

LIST OF FIGURES

4.10	Semi-classical transition time theoretical vs simulation	57
5.1	Geometric foundation of the stochastic algorithm	61
5.2	Correlation functions $N = 32, Q = 20, \hbar = 0$	64
5.3	Correlation functions $N = 64, Q = 30, \hbar = 0$	64
5.4	Classical correlation functions fixed breather size	65
5.5	Classical correlation functions fixed initial condition	66
5.6	Correlation functions $N = 32, Q = 20, \hbar = 1$	67
5.7	Correlation functions $N = 64, Q = 30, \hbar = 1$	68
5.8	Correlation functions fixed initial conditions with different \hbar	69
5.9	Coefficient γ vs \hbar	70
5.10	Coefficient θ vs \hbar	70
5.11	Correlation functions $N = 32, Q = 20, \hbar = 10$	71
5.12	Correlation functions $N = 64, Q = 30, \hbar = 10$	71
5.13	Mean Participation Ratio for $Q = 20, L = 32$ varying \hbar	72
5.14	Mean Participation Ratio for $Q = 30, L = 64$ varying \hbar	72
5.15	Mean Participation Ratio	73
5.16	Universality $N = 64, Q = 30, \hbar = 0$	74
5.17	Universality $N = 64, Q = 30, \hbar = 1$	75
5.18	Universality $N = 64, Q = 30, \hbar = 10$	75
5.19	Correlation function rescaling factor varying breather size	76
5.20	Universality for different \hbar	77
5.21	Rescaling factor dependence on \hbar	77
D.1	Bose-Hubbard hamiltonian matrix	92

List of Tables

4.1	Fit results for Eq. (4.53)	56
4.2	Fit values of Eq. (4.56)	58
5.1	Fit coefficients for Eq. (5.16)	69
5.2	Fit coefficients for the correlation functions of Fig. (5.16), Fig. (5.17), Fig. (5.18)	76

1 | Introduction

1.1 Anderson and Many-Body Localization

Experimental progress of the last few years has enabled the realization of isolated quantum many-body systems that evolve under their intrinsic dynamics. There are many examples of such systems, as trapped ions, ultracold atoms in optical lattices as well as nuclear and electron spin associated with impurity atoms in diamond. One may wonder if there are conditions under which these systems fail to thermalize, that is, even at long times, the conventional equilibrium configuration is not reached. In statistical mechanics, the mechanism for thermalization, as well as the approach to thermal equilibrium in different systems, are issues of central importance.

Commonly, dynamics leads to thermalization: this happens in ergodic systems, where different degrees of freedom can exchange energy and information. Consequently, these systems effectively reach a state of thermal equilibrium, even if, as a whole, they remain in a pure quantum state. Quantum statistical mechanics governs the stationary states in such systems. While it is known that there exist different regimes of thermalization, it is of particular interest to find systems that do not reach thermal equilibrium (see Fig. (1.1)). In this case, initial state information is still contained in the final state of the system; the initial state governs, therefore, the dynamics at long times and the steady state. The essence of ergodic dynamics is that the system as a whole acts a thermal reservoir for its subsystems, provided that these are small enough. Consequently, thermalization requires that different parts of ergodic systems exchange energy and particles, and thus thermal systems must be conducting. Insulating systems, therefore, naturally break ergodicity. The celebrated Anderson Localization is a well-studied example of insulating behaviour in non-interacting disordered

systems.

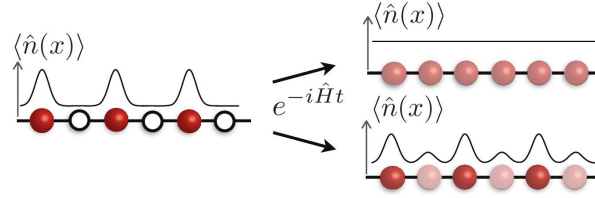


Figure 1.1: Interacting particles are initially prepared in a state with non-uniform density. After unitary evolution, the thermalizing system reaches the state where all lattice sites are equally populated, with uniform density profile (at the top). The many-body localized state, instead, retains memory of the initial state even at infinite time (bottom)

In the seminal paper [4], Anderson analysed the problem of the propagation of a quantum particle in a disordered potential under unitary evolution (see [5] for a review). The essence of Anderson localization is that a disordered potential can drastically change the nature of single-particle eigenstates in a regular lattice. Instead of propagating Bloch states, similar to plane waves, in fact, wave functions become localized in some region of space, decaying exponentially far away from that region. To better understand how this can happen, consider the Hamiltonian (see also Fig. (1.2)):

$$H := -g \left(\sum_{\langle ij \rangle} c_i^\dagger c_j + c_j^\dagger c_i \right) + \sum_i \epsilon_i c_i^\dagger c_i \quad (1.1)$$

on a d -dimensional lattice. The operators (c_i^\dagger, c_i) are the fermionic creation and annihilation operators, $g \geq 0$ is the hopping amplitude and ϵ_i are the on-site energies, that are independent and identically distributed random variables uniformly chosen in $[-W/2, W/2]$, where W is the amplitude of the disorder.

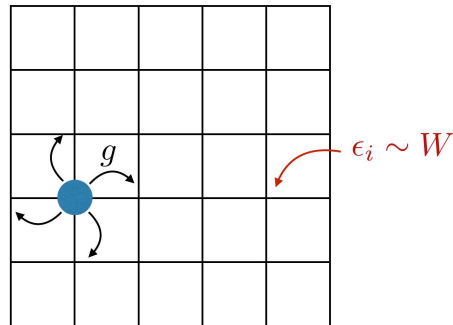


Figure 1.2: Anderson model for the localization transition

Consider, for simplicity, the strong disorder case, in which the variance of the random potential, W , is much larger than the tunnelling between neighbouring sites of the lattice, g . In this limit, it is impossible to have resonant transitions between neighbouring sites, and the same holds for sites separated by long distances. The tunnelling process between two sites at distance of $\sim n$ lattice sites apart, indeed, typically occurs as a n -th level perturbation theory phenomenon, and it is suppressed as $t_n \sim (g/W)^n$. On the other hand, the typical energy difference between two sites, δ_n , decays only algebraically with the distance, $\delta_n \sim W/n^d$. This naive argument explains why long-range hopping processes are off-resonant and the wave functions are localized in the strong disorder limit. This means that Anderson localization leads to the absence of diffusion, suppressing transport (see Fig. (1.3)).

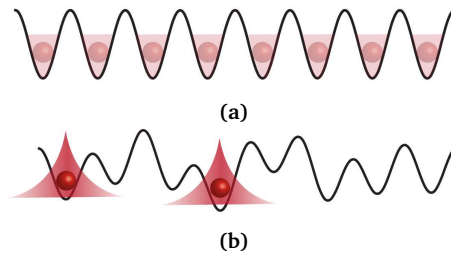


Figure 1.3: Fig. (1.3a): in a clean crystal, eigenstates are Bloch waves extended through the sample. For. (1.3b): with sufficiently strong disorder there is a vanishing probability for a particle to make a resonant transition between two spatially separated sites.

In order to make the above argument more quantitative, we may look at the diffusion coefficient D for the motion on the lattice. For simplicity, let us consider first the two opposite regimes of disorder-free and infinite disorder

systems:

- Disorder-free ($W = 0$): in this situation, the eigenfunctions of the Hamiltonian, that is translationally invariant, are plane waves; in the thermodynamic limit the center of the wave packet remains at $x_t = 0$ while the mean-square displacement diverges ballistically as $\Delta x_t^2 = 2dg^2t^2$;
- Infinite disorder case ($g/W = 0$): in this limit the problem is trivial, since the density of states remains discrete distribution corresponding to a pure point spectrum $\rho(j, E) = \delta(E - \epsilon_j)$ for every value of L .

The interesting question is about what happens in between, that is, for finite and non-vanishing disorder. From a classical perspective, the motion of the particle leads to diffusive motion with $\Delta x_t^2 \simeq Dt$ for times t much larger than the typical time τ between scattering over impurities. Using the semi-classical approximation, it is possible to show that the diffusion coefficient D should depend on the disorder W as:

$$D \sim \frac{g^3}{W^2} \quad (1.2)$$

This means that localization should appear only in the infinite disorder limit, as, in the semi-classical case, the diffusion coefficient never vanishes for finite values of W . However Anderson, in his work [4] predicted that the diffusion coefficient might vanish for a sufficiently strong but finite disorder $W > W_c$: in this localized phase Δx_t^2 remains finite for all t . (see Fig (1.4)).

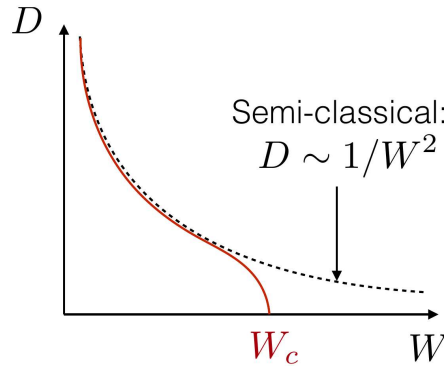


Figure 1.4: The diffusion coefficient of a quantum particle in a disordered potential vanishes with probability 1 for a finite value of the disorder strength.

The Many-Body and the Anderson localization problems are closely related;

in particular, we can obtain the defining Hamiltonian for the first by adding to the Anderson Hamiltonian Eq. (1.1) a two-body local interaction potential:

$$H := -g \left(\sum_{\langle ij \rangle} c_i^\dagger c_j + c_j^\dagger c_i \right) + \sum_i \epsilon_i c_i^\dagger c_i + \frac{1}{2} \frac{\lambda}{v} \sum_{ij} c_i^\dagger c_j^\dagger u(i-j) c_j c_i \quad (1.3)$$

where $u(i-j)$ is a short-ranged interaction kernel. As we mentioned previously, the Hamiltonian Eq. (1.3) displays many-body localization if the system does not thermalize under its own unitary dynamics when starting from a generic many-body state $|\psi\rangle$. In general, we say that a many-body system thermalizes if and only if the following relation holds:

$$\lim_{t \rightarrow \infty} \lim_{L \rightarrow \infty} \langle \psi(t) | O_\lambda | \psi(t) \rangle = \lim_{L \rightarrow \infty} \text{Tr} \left(O_\lambda \frac{e^{-\beta(H-\mu N)}}{Z} \right) \quad (1.4)$$

In the non-interacting case ($\lambda = 0$) thermalization breaks down, as we pointed out. However, in general, one may expect that interacting many-body systems do thermalize. A characterization for non-thermalization can be given by considering the eigenstates of the many-body Hamiltonian: qualitatively, if these eigenstates are weak deformations of the non-interacting eigenstates, we say that thermalization breaks down. This statement is the content of the ETH (eigenstates thermalization hypothesis): it consists in assuming that generic Hamiltonians are thermal if typical eigenstates $|\psi_\mu\rangle$ are thermal, in the sense of Eq. (1.4). Notice, for instance, that the ETH is only a sufficient condition for thermalization: it is not true, indeed, for many-body Anderson localized systems (see [6] for example). It is evident that many-body localization is a highly non-trivial problem and there is not a general technique to solve it.

1.2 Non-linear systems

In the previous section we have seen that disordered quantum system may display localization phenomena: however, there are other systems that can present the same feature. In particular, non-linear systems can provide it.

A system is non-linear if its output is not proportional to the input. Mathematically, the signature of a non-linear system is the breakdown of the superposition principle, which states that the sum of two solutions of the equations

describing the system is again a solution. Consequently, in non-linear systems the physical behaviour of the whole is more than the sum of its parts.

The non-linearity of a system makes it highly non-trivial and its analysis difficult. As an example, consider that:

- In a non-linear system a small disturbance, such as a little modification of the initial conditions, can lead to a big difference in the behaviour of the system at a later time. This could make the behaviour of a non-linear system very complex, as happens for chaos.
- When the equations describing the non-linear system are known, the breakdown of the superposition principle makes the Fourier transform technique inapplicable. Moreover, there is not another systematic method in solving non-linear equations.
- In many cases such equations are not even known, as in many complex and economic systems.

It is clear, then, that the use of computers is unavoidable in the study of non-linear systems. Indeed, the birth of non-linear science dates back to 1953 when E. Fermi, J. Pasta, S. Ulam and M. Tsingou (FPUT) conducted numerical experiments on the MANIAC computer of a vibrating string subject to quadratic and cubic forces [1]. The aim of Fermi was to simulate the one-dimensional analogue of atoms in a crystal: a long chain (i.e. a discrete set) of particles linked by springs obeying Hooke's law with a weak non-linear correction. Since then, non-linear dynamics has emerged in a wide variety of models appropriate for describing important physical systems. Among them there are: the Ginzburg-Landau theory of superconductivity, with the non-linearity given by the powers of the order parameter in the expression for the free energy; the order parameter description of superfluidity, that yields to the Gross-Pitaevskii; the soliton solutions to the Korteweg - de Vries equations (the continuum limit of the FPUT problem) and the consequent widespread applications of the Non-Linear Schrödinger Equation.

In particular, the Discrete Non-Linear Schrödinger Equation (DNLSE) (see Eq. (2.1) and Eq. (2.3)) is one of the most fundamental non-linear lattice dynamical models. Its importance is mainly due to two important facts. On the one hand, the DNLSE can be obtained by discretizing its famous and integrable continuum counterpart, namely the non-linear Schrödinger Equation

(NLSE)(see [7]), that is the relevant model for describing the self-focusing and collapse of Langmuir waves in plasma physics [8], the freak waves in the ocean [9] and also the electric field in optical fibers ([10] for example). On the other hand, the DNLSE is by itself a model of particular interest for a variety of systems it can describe.

The first set of experimental survey that gave rise to an intense interest in the DNLSEs was in the area of non-linear optics. In this research field, a multiplicity of phenomena such as discrete diffraction, Peierls barriers, diffraction management and gap solitons were observed experimentally([11], [12], [13]). This gave rise to a tremendous increase also on the theoretical side of studies inspecting such discrete media.

Another area where the DNLSE gives accurate predictions, even though it is not the prototypical model, is in the non-linear localized modes in optically induced lattices in photorefractive media. The possibility of the presence of non-linear waves and solitons in periodic, mainly two-dimensional, lattices was first predicted in [14] and then experimentally realized (in [15] for example). Since then, an explosive growth in this area took place and an ever-growing set of structures has been predicted and obtained experimentally in lattices induced with self-focusing non-linearities.

Another completely different physical setting where the DNLSE is a relevant tool is that of atomic physics; in particular the most recently discovered state of matter, Bose-Einstein condensates (BEC), may be trapped in a periodic optical lattice [16]. Analysing a BEC distributed in the minima of the potential generated by the optical lattice, assuming that particles on different minima interact weakly due to tunnelling, and taking into account the two-body scattering effect, one can arrive at the DNLSE. It is also possible to obtain it from the Gross-Pitaevskii equation for a BEC in a periodic potential.

1.3 Outline

Recently, the presence of a high-energy phase characterized by the condensation of energy in the form of breathers in non-linear systems has attracted the attention of many scholars. As we will discuss more in detail in the following chapter, it has been found (see, [2] and [17] for example) that the Discrete Non-Linear Schrödinger Equation displays a phase characterized by the non-equivalence between microcanonical and canonical ensembles, thus yielding to non-Gibbs

states and negative temperatures. Moreover, it has been claimed in [3] that a model closely related to the DNLSE, the Josephson Junction Array model, presents a similar phase in the quantum regime and that such phenomenon may possibly survive in the classical limit.

After this Introduction, the thesis is organized as follows:

- In Chapter 2 we introduce the DNLSE and JJA models, reviewing their known properties and showing, in particular, how to identify the presence of a phase described by non-Gibbs states from the computation of the partition function.
- In Chapter 3 we use the partition-function approach to prove that the JJA does not display a localized phase in the classical limit. Moreover, a geometric construction is introduced for the study of the phase-space of our systems: it will allow us to have a clearer view on the localization transition in the DNLSE and on the absence of transition in the JJA.
- In Chapter 4 we quantize the DNLSE and we address the question of determining whether the localized phase survives also in the quantum limit.
- In Chapter 5 we introduce a simplified computational model for the study of the DNLSE both in its classical and quantum versions, based on a stochastic evolution rather than the Hamilton equations of motions.
- In Chapter 6 we give the conclusions, summarizing the results obtained and suggesting some possible directions for further investigations.

2 | A review of the most recent results

In this section we will give a review the one-dimensional DNLS model presented in [2], performing the main mathematical steps needed to understand the reasoning and the fundamental results obtained, and then introduce the Josephson Junction Array model.

2.1 Non-Gibbs states and Ergodicity Breaking

In a macroscopic system characterized by the presence of only one conserved quantity (i.e. the energy E), thanks to the equivalence between statistical ensembles, the canonical distribution function enables us to map any value of the average energy density $e = E/N$ (with N being the number of lattice sites) to a positive value of the inverse temperature β of the canonical distribution. Notice that this fact holds independently of whether the microcanonical dynamic is ergodic or not. Of course, this statement is correct if the equivalence of ensembles holds.

Things change if there is a second conserved quantity, as happens in the Discrete Non-Linear Schrodinger Equation (see Sec. (2.2)). Indeed, it has been shown in [18] that an approach based on the canonical ensemble yields to negative temperature phase at high energies, which contradicts the existence of a Gibbsian measure, as we stated above. This means that, in such regime, the equivalence between ensembles is no more valid, and the thermodynamics of this model is well-defined only in the microcanonical ensemble. As shown in [2] and as we will resume in Sec. (2.2), the non-equivalence between statistical en-

sembles can be understood as a consequence of the non-analytic structure of the microcanonical partition function in the high-energy phase, that does not allow us to perform the inverse Laplace transform, which is the mean for connecting the different ensembles. Therefore, the microcanonical dynamics at equilibrium (if existent) is defined by two densities $e = E/N$ and $a = A/N$, where A is the second conserved quantity. In the thermodynamic limit $N \rightarrow \infty$ it can be found (see Sec. (2.2)) that the Gibbs grand-canonical formalism can be applied to the microcanonical dynamics only for energy densities $e \leq 2a^2$, referring to the hamiltonian Eq. (2.1). However, the microcanonical dynamics can address also states with $e > 2a^2$.

It has also been addressed the question of whether the non-Gibbs phase of the DNLSE is ergodic or not. It has been shown in [19] that the dynamic stays ergodic, even though the relaxation times rapidly grow in the deep non-Gibbs phase; this turns the system into a dynamical glass, which can be treated as non-ergodic for any practical purpose. Microscopically, the motivation for this slow dynamics is due to the presence of long-lived discrete breathers that, in the high-energy limit, where the system is almost integrable, have a low probability of resonant interactions with the nearest neighbours.

2.2 The classical Discrete Non-Linear Schrodinger Equation

The **Discrete Non-Linear Schrodinger Equation** (DNLSE) model consists of a complex scalar field z_j defined on a one-dimensional lattice with periodic boundary conditions made of N sites, described by the Hamiltonian:

$$\mathcal{H} = \sum_{j=1}^N (z_j^* z_{j+1} + z_j z_{j+1}^*) + \sum_{j=1}^N |z_j|^4 \quad (2.1)$$

The canonical variables are $q_j \equiv z_j$ and $p_j \equiv -iz_j^*$ with c.c.r. $\{q_j, p_j\} = \delta_{ij}$. The dynamics of the system is thus governed by the equations of motion:

$$\dot{q}_j = \frac{\partial \mathcal{H}}{\partial p_j} \quad (2.2)$$

$$i\dot{z}_j = -(z_{j+1} + z_{j-1}) - 2|z_j|^2 z_j \quad (2.3)$$

These equations of motion conserve not only the total energy but also the quantity:

$$\mathcal{A} \equiv \sum_{j=1}^N |z_j|^2 \quad (2.4)$$

(a sort of squared norm of the “wave function”) because of the quantum origin of the problem. \mathcal{A} can also be intended as the total number of particle of the problem. The overall scenario is described in the phase diagram Fig. (2.1), where $a = \mathcal{A}/N$ and $e = E/N$. There is a region contained between the the

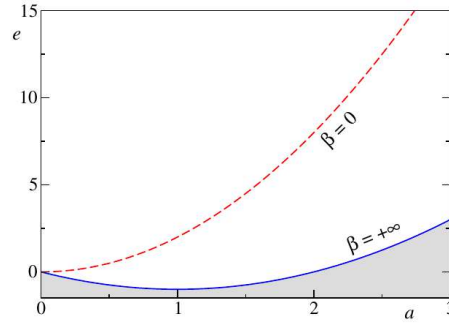


Figure 2.1: Equilibrium phase diagram in the plane ($a = \mathcal{A}/N$, $e = E/N$) for the DNLSE

zero temperature line ($\beta = +\infty$) and the infinite temperature line ($\beta = 0$) where the dynamics is controlled by standard thermodynamics evolution, while above the $\beta = 0$ line, in any finite lattice, the dynamics is characterized by the birth of long-living localized non-linear excitations.

The Hamiltonian Eq. (2.1) can be rewritten in a different form, by means of the following change of variables:

$$z_j = \sqrt{A_j} e^{i\phi_j} \quad (2.5)$$

yielding the Hamiltonian:

$$\mathcal{H} = \sum_j 2\sqrt{A_j A_{j+1}} \cos(\phi_j - \phi_{j+1}) + \sum_j A_j^2 \quad (2.6)$$

In order to quantify what we have just described, we have to compute the microcanonical entropy of the DNLSE Hamiltonian Eq. (2.1) for fixed values of E and \mathcal{A} near the $\beta = 0$ line. In general we can write:

$$S_N(\mathcal{A}, E) = \log \Omega_N^0(\mathcal{A}, E) \quad (2.7)$$

where, having set the Boltzmann constant k_B to unity, the microcanonical partition function is:

$$\begin{aligned} \Omega_N^O(\mathcal{A}, E) = \int \prod_{j=1}^N d\mathfrak{R}(z_j) d\mathfrak{J}(z_j) & \delta \left(\mathcal{A} - \sum_{j=1}^N |z_j|^2 \right) \cdot \\ & \cdot \delta \left(E - \left[\sum_{i=1}^N (z_i^* z_{i+1} + z_i z_{i+1}^*) + \sum_{i=1}^N |z_i|^4 \right] \right) \end{aligned} \quad (2.8)$$

where, from now on, we will call $d\mu(z_j) \equiv d\mathfrak{R}(z_j) d\mathfrak{J}(z_j)$. Let us fix the specific energy to the value $e = E/N$ and choose a rescaling of the variables z_j so that the total local energy is always of order $\mathcal{O}(1)$, and thus we use $\hat{z}_j := z_j/e^{1/4}$. In terms of these new variables the Hamiltonian is:

$$\mathcal{H} = \sqrt{e} \sum_{j=1}^N (\hat{z}_j^* \hat{z}_{j+1} + \hat{z}_j \hat{z}_{j+1}^*) + e \sum_{j=1}^N |\hat{z}_j|^4 \quad (2.9)$$

It is evident, then, that in the large- e limit the hopping term is sub-leading w.r.t. the local non-linear quartic self-interaction term, and thus we will neglect it. This is meaningful since we are interested in the limit of large temperature (near the $\beta = 0$ line). In this region we are also in the high-energy limit and thus, if we ideally fix the energy per site, is evident that the hopping term is negligible w.r.t. the other term. It can be shown that this approximation is exact in the thermodynamic limit. Therefore the partition function can be written in this approximation as:

$$\Omega_N(\mathcal{A}, E) = \int \prod_{j=1}^N d\mu(z_j) \delta \left(\mathcal{A} - \sum_{j=1}^N |z_j|^2 \right) \delta \left(E - \sum_{i=1}^N |z_i|^4 \right) \quad (2.10)$$

2.2.1 The microcanonical partition function

Now we analyze the explicit calculations of the partition function $\Omega_N(\mathcal{A}, E)$ using a large deviation technique.

In order to compute $\Omega_N(\mathcal{A}, E)$ it is convenient to express the variables in their polar form $z_j = \rho_j e^{i\phi_j}$, and performing a trivial integration over the angular

variable, obtaining:

$$\Omega_N(\mathcal{A}, E) = (2\pi)^N \int_0^\infty \left[\prod_{j=1}^N d\rho_j \rho_j \right] \delta \left(\mathcal{A} - \sum_{j=1}^N \rho_j^2 \right) \delta \left(E - \sum_{i=1}^N \rho_i^4 \right) \quad (2.11)$$

In order to resolve the constraint over \mathcal{A} we perform a Laplace transform:

$$\begin{aligned} \tilde{\Omega}_N(\lambda, E) &= \int_0^\infty d\mathcal{A} e^{-\lambda\mathcal{A}} \Omega_N(\mathcal{A}, E) = \\ &= (2\pi)^N \int_0^\infty \left[\prod_{j=1}^N d\rho_j \rho_j \right] e^{-\lambda \sum_{j=1}^N \rho_j^2} \delta \left(E - \sum_{i=1}^N \rho_i^4 \right) \end{aligned} \quad (2.12)$$

Now we can re-obtain the partition function inverting the Laplace transform:

$$\Omega_N(\mathcal{A}, E) = \frac{1}{2\pi i} \int_{\lambda_0 - i\infty}^{\lambda_0 + i\infty} d\lambda e^{\lambda\mathcal{A}} \tilde{\Omega}_N(\lambda, E) \quad (2.13)$$

where λ_0 must be such that the integration contour lies in the domain of convergence of $\tilde{\Omega}_N(\lambda, E)$ (we will be more specific about this later). Let us introduce a further change of variables $\rho_j^4 = \epsilon_j$, yielding:

$$\begin{aligned} \tilde{\Omega}_N(\lambda, E) &= \left(\frac{\pi}{2} \right)^N \int_0^\infty \prod_{j=1}^N \frac{d\epsilon_j}{\sqrt{\epsilon_j}} e^{-\sum_{i=1}^N \sqrt{\epsilon_i}} \delta \left(E - \sum_{i=1}^N \epsilon_i \right) = \\ &= \left(\frac{\pi}{\lambda} \right)^N \mathcal{Z}_N(\lambda, E) \end{aligned} \quad (2.14)$$

where

$$\mathcal{Z}_N(\lambda, E) = \int_0^\infty \prod_{j=1}^N d\epsilon_j f_\lambda(\epsilon_j) \delta \left(E - \sum_{i=1}^N \epsilon_i \right) \quad (2.15)$$

and $f_\lambda(\epsilon_j)$ is a normalized distribution function given by:

$$f_\lambda(\epsilon) = \theta(\epsilon) \frac{\lambda}{2\sqrt{\epsilon}} e^{-\lambda\sqrt{\epsilon}} \quad (2.16)$$

From Eq. (2.15) it is evident that the calculation of $\mathcal{Z}_N(\lambda, E)$ coincides with the computation of the probability distribution for N independent and identically distributed random variables (ϵ_i) described by the probability distribution $f_\lambda(\epsilon_i)$ with the global constraint $\sum_{i=1}^N \epsilon_i = E$. As it is shown in Appendix (C), global constraints, as the one for the total energy, given on the sum of random

variables, give rise to condensation phenomena when the individual probability fulfils the bounds:

$$\exp(-\epsilon) < f_\lambda(\epsilon) < \frac{1}{\epsilon^2} \quad (2.17)$$

as shown in Eq. (C.8). According to Eq. (2.16), this is exactly the case of the partition function Eq. (2.15). Following the argument presented in Appendix (C), it is easily found that the condensation phenomenon occurs when the total energy E overtakes a threshold value E_{th} that is equal to the average total energy, i.e.:

$$E > E_{th} = N\langle\epsilon\rangle \quad (2.18)$$

where the average $\langle \rangle$ is taken over the distribution $f_\lambda(\epsilon)$. In the localized phase it is more convenient for the system to condensate the excess energy $\Delta E = E - E_{th}$ in a finite region of the lattice.

We can easily calculate the first two momenta and the variance of the probability distribution Eq. (2.16).:

$$\langle\epsilon\rangle = \frac{2}{\lambda^2} \quad (2.19)$$

$$\langle\epsilon^2\rangle = \frac{24}{\lambda^4} \quad (2.20)$$

$$\sigma^2 = \langle\epsilon^2\rangle - \langle\epsilon\rangle^2 = \frac{20}{\lambda^4} \quad (2.21)$$

2.2.2 Analytic properties of the partition function

We want now to proceed with the calculation of the partition function; in order to do this, we perform its Laplace transform with respect to E , introducing β as the conjugate variable. In general $\beta \in \mathbb{C}$:

$$\begin{aligned} \tilde{z}_N &:= \int_0^\infty dE e^{-\beta E} z_N = \int_0^\infty d\epsilon_1 \dots d\epsilon_n e^{-\sum_{j=1}^N \epsilon_j} \prod_{j=1}^N f_\lambda(\epsilon_j) = \\ &= \left[\int_0^\infty d\epsilon e^{-\beta\epsilon} f_\lambda(\epsilon) \right]^N =: e^{N \log[z(\lambda, \beta)]} \end{aligned} \quad (2.22)$$

where we have defined:

$$z(\lambda, \beta) = \int_0^\infty d\epsilon e^{-\beta\epsilon} f_\lambda(\epsilon) = \sqrt{\pi} \frac{\lambda}{2\sqrt{\beta}} \exp\left(\frac{\lambda^2}{4\beta}\right) \text{Erfc}\left(\frac{\lambda}{2\sqrt{\beta}}\right) \quad (2.23)$$

and

$$\operatorname{Erfc}\left(\frac{\lambda}{2\sqrt{\beta}}\right) = \frac{2}{\sqrt{\pi}} \int_{\lambda/(2\sqrt{\beta})}^{\infty} e^{-t^2} dt \quad (2.24)$$

is the complementary error function defined in the complex β -plane, with a brunch cut on the negative real semiaxis. Eq. (2.23) can be easily derived using the definition of $f_\lambda(\epsilon)$.

We can recover the original partition function by performing the inverse Laplace transform of $\tilde{Z}_N(\lambda, \beta)$:

$$Z_N(\lambda, \beta) = \int_{\beta_0 - i\infty}^{\beta_0 + i\infty} d\beta \exp[\beta E + N \log[z(\lambda, \beta)]] \quad (2.25)$$

Form the theory of Laplace transform, we know that $\beta_0 \in \mathbb{R}$ and moreover it must be located at the right of all the singularities. Since $z(\lambda, \beta)$ has a brunch cut for $\beta < 0$, then $\beta_0 \geq 0$. We are performing the integral of an exponential function, so we would like to use the saddle-point method; if the saddle-point equation:

$$\frac{E}{N} = -\frac{1}{z(\lambda, \beta)} \frac{\partial z(\lambda, \beta)}{\partial \beta} \quad (2.26)$$

has a real and positive solution, we can use this solution as β_0 . In this case β_0 can be interpreted as a negative temperature and the value of the integral can be approximated as:

$$Z_N \sim \exp[\beta_0 E + N \log[z(\lambda, \beta_0)]] \quad (2.27)$$

In the model we are studying, i.e. in the DNLSE, when $E < E_{\text{th}}$, there exist a real positive solution to Eq. (2.26) and thus the partition function can be calculated using the saddle-point method; the integration contour is represented by the blue dashed line in Fig. (2.2).

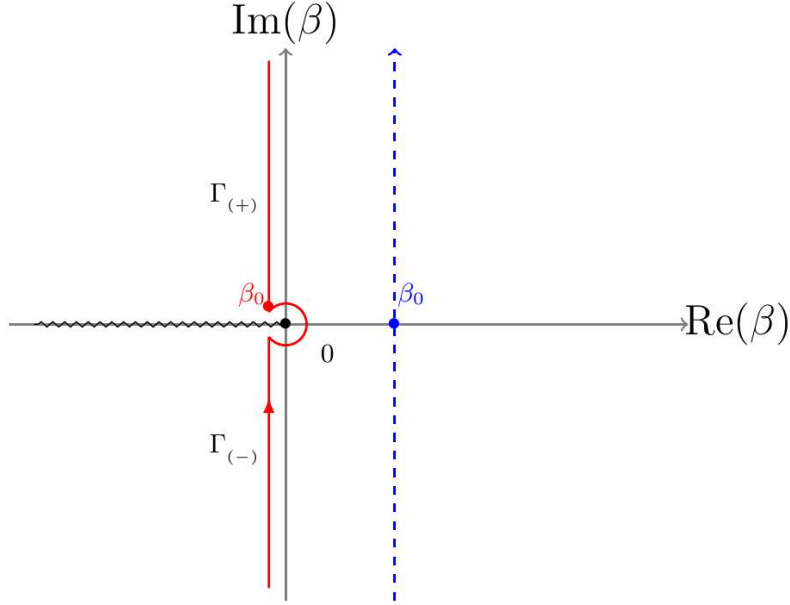


Figure 2.2: Analytic structure of the function $z(\beta, \lambda)$ in the complex β plane, λ is fixed to a real positive value. The wiggly line is the brunch cut on the real negative axis, while the dashed blue line is the Bromwich contour for the calculation of the partition function $Z(\lambda, E)$ when $E < E_{th}$, with β_0 indicating the location of the saddle-point. The continuous red line is the Bromwich contour for the calculation of the partition function $Z(\lambda, E)$ when $E > E_{th}$, β_0 is the new saddle-point.

Conversely, for $E > E_{th}$ there is no positive real solution to Eq. (2.26) and thus the Bromwich integral as to be performed using another technique (see [20]). For $E \gtrsim E_{th}$, the new saddle point would be close to the origin and we can choose the Bromwich contour to be the one represented by the red line in Fig. (2.2). Moreover, we will have to expand the integrand near the origin in order to find the scaling properties of \mathcal{Z}_N via integration. In other words, we are choosing $\beta_0 = 0$ and we will perform the integral expanding its argument near the origin, where there will be a non-analytic contribution because of the branch cut (the calculation is explained in Sec. (2.2.3)).

If we want to evaluate $\mathcal{Z}_N(\lambda, \beta)$ at the energy scale $\Delta E = E - E_{th} \sim N^\gamma$, we have to retain the the leading terms only up to a given order in the expansion of $z(\lambda, \beta)$. For example, if one sets $\gamma = 1/2$ (*Gaussian regime*), by expanding $z(\lambda, \beta)$ near $\beta = 0$ only the terms up to order $\beta \sim -1/2$ are needed; in this case

one obtains:

$$z_N = \frac{1}{\sigma\sqrt{2\pi N}} \exp\left[-\frac{(E - E_{th})^2}{2\sigma^2 N}\right] \quad (2.28)$$

which is obvious because of the Central Limit Theorem.

On the other hand, if we want to study the case $\gamma = 1$, called the *extreme large deviation* regime, we have to keep, in the expansion of $z(\lambda, \beta)$, the terms up to order $\beta \sim 1/N$, and one obtains:

$$z_N \sim \exp\left(-\sqrt{E - E_{th}}\right) \quad (2.29)$$

As we will discuss later, the *Gaussian* regime corresponds to a delocalized phase, while the *extreme large deviation* regime corresponds to a localized phase. If we want to understand if the transition between these two phases occurs as a real thermodynamic phase transition, we should study the intermediate *matching* regime, that we can heuristically identify by:

$$\frac{(E - E_{th})^2}{2\sigma^2 N} \sim \sqrt{E - E_{th}} \quad (2.30)$$

and the intermediate scale is therefore:

$$E - E_{th} \sim N^{2/3} \quad (2.31)$$

2.2.3 Matching regime: the non-analytic contribution

As we announced in the previous subsection, we are interested in studying the *matching* regime of the partition function: in this situation we can perform the integration using the expansion of $z(\lambda, \beta)$ near the origin, as we discussed previously.

Since for $E > E_{th}$ the saddle point Eq. (2.26) has no real solution, we have to analytically continue $z(\lambda, \beta)$ in the complex β plane and perform the expansion near $\beta = 0$ separately along the upper and lower brunch cut, thus for $\Re(\beta) < 0$:

$$\begin{aligned} \lim_{\delta \rightarrow 0} z(\lambda, \beta + i\delta) &= z(\lambda, \beta + i0) \\ \lim_{\delta \rightarrow 0} z(\lambda, \beta - i\delta) &= z(\lambda, \beta - i0) \end{aligned} \quad (2.32)$$

The expansion of $z(\lambda, \beta)$ near $\beta = 0$ has to be carried out carefully: the branch-cut of z is due to $\text{Erfc}\left(\frac{\lambda}{2\sqrt{\beta}}\right)$, whose expansion is given by:

$$\text{Erfc}\left(\frac{a}{\sqrt{x}}\right) = \frac{1}{a} e^{-a^2/x} \frac{\sqrt{x}}{\sqrt{\pi}} \left[1 - \frac{x}{2a^2} + \frac{3x^2}{4a^4} + \dots \right] + (-1)^{\lfloor (\arg(x)+\pi)/2\pi \rfloor + 1} + 1 \quad (2.33)$$

where $\arg(\cdot)$ is the complex argument function and the expansion is done around $x = 0$. In our case it assumes the form:

$$\text{Erfc}\left(\frac{\lambda}{2\sqrt{\beta}}\right) = \frac{2}{\lambda} e^{-\lambda^2/4\beta} \frac{\sqrt{\beta}}{\sqrt{\pi}} \left[1 - \frac{2\beta}{\lambda^2} + 12\frac{\beta^2}{\lambda^4} + \dots \right] + (-1)^{\lfloor (\arg(\beta)+\pi)/2\pi \rfloor + 1} + 1 \quad (2.34)$$

Since we are interested in performing the integral Eq. (2.25) with $\beta_0 = 0$ from $-i\infty$ to $+i\infty$, we have that $\arg(\beta - i0^-) = -\pi + \varepsilon$ and $\arg(\beta + i0^+) = -\pi - \varepsilon$. Therefore we get:

$$\begin{aligned} z(\lambda, \beta + i0^+) &= \sqrt{\pi} \frac{\lambda}{2\sqrt{\beta}} e^{\lambda^2/4\beta} \left[\frac{2}{\lambda} e^{-\lambda^2/4\beta} \frac{\sqrt{\beta}}{\sqrt{\pi}} \left(1 - \beta \langle \epsilon \rangle + \frac{\beta^2}{2} \langle \epsilon^2 \rangle + \dots \right) + 1 \right] \\ z(\lambda, \beta + i0^-) &= \sqrt{\pi} \frac{\lambda}{2\sqrt{\beta}} e^{\lambda^2/4\beta} \left[\frac{2}{\lambda} e^{-\lambda^2/4\beta} \frac{\sqrt{\beta}}{\sqrt{\pi}} \left(1 - \beta \langle \epsilon \rangle + \frac{\beta^2}{2} \langle \epsilon^2 \rangle + \dots \right) \right] \end{aligned} \quad (2.35)$$

and thus:

$$\begin{aligned} z(\lambda, \beta + i0^+) &= 1 - \langle \epsilon \rangle \beta + \frac{\beta^2}{2} \langle \epsilon^2 \rangle + \mathcal{O}(\beta^3) + \sqrt{\frac{2\pi}{\beta \langle \epsilon \rangle}} \exp\left(\frac{\lambda^2}{4\beta}\right) \\ z(\lambda, \beta + i0^-) &= 1 - \langle \epsilon \rangle \beta + \frac{\beta^2}{2} \langle \epsilon^2 \rangle + \mathcal{O}(\beta^3) \end{aligned} \quad (2.36)$$

Observe that, since $\Re(\beta) < 0$, the exponential term in $z(\lambda, \beta + i0^+)$ is exponentially suppressed.

With this expansion, we can now compute the partition function:

$$\mathcal{Z}_N(\lambda, E) = \mathcal{J}^{(+)}(\lambda, E) + \mathcal{J}^{(-)}(\lambda, E) \quad (2.37)$$

where

$$\begin{aligned} \mathcal{J}^{(+)}(\lambda, E) &= \int_{\Gamma^{(+)}} \frac{d\beta}{2\pi i} \exp \left[\beta(E - E_{th}) + \frac{N}{2} \sigma^2 \beta^2 + N \mathcal{O}(\beta^2) + N \sqrt{\frac{2\pi}{\beta \langle \epsilon \rangle}} \exp \left(\frac{1}{2 \langle \epsilon \rangle \beta} \right) \right] \\ \mathcal{J}^{(-)}(\lambda, E) &= \int_{\Gamma^{(-)}} \frac{d\beta}{2\pi i} \exp \left[\beta(E - E_{th}) + \frac{N}{2} \sigma^2 \beta^2 + N \mathcal{O}(\beta^2) \right] \end{aligned} \quad (2.38)$$

Using a scaling ansatz for β in the matching regime, i.e. $\beta \rightarrow \beta/N^{1/3}$, we can write the partition function as:

$$\mathcal{Z}_N = \frac{1}{\sigma \sqrt{2\pi N}} e^{-N^{1/3} \frac{\zeta^2}{2\sigma^2}} + \mathcal{C}(\lambda, \zeta) \quad (2.39)$$

where $\zeta = \frac{E - E_{th}}{N^{2/3}}$ and

$$\mathcal{C}(\lambda, \zeta) = N \sqrt{\frac{2\pi}{\langle \epsilon \rangle}} \int_{\Gamma^{(+)}} \frac{d\beta}{2\pi i} \frac{1}{\sqrt{N^{1/3} \beta}} e^{N^{1/3} F_\zeta(\lambda, \beta)} \quad (2.40)$$

with

$$F_\zeta(\lambda, \beta) = \beta \zeta + \frac{1}{2} \sigma^2 \beta^2 + \frac{1}{2 \langle \epsilon \rangle \beta} \quad (2.41)$$

The integral in Eq. (2.40) can be performed by means of the saddle point method, yielding:

$$\int_{\Gamma^{(+)}} \frac{d\beta}{2\pi i} \frac{1}{\sqrt{N^{1/3} \beta}} e^{N^{1/3} F_\zeta(\lambda, \beta)} \approx e^{-N^{1/3} \chi(\zeta)} \quad (2.42)$$

where $\chi(\zeta)$ has the following asymptotic behaviours:

$$\chi(\zeta) = \begin{cases} \frac{3}{2} \left(\frac{\sigma}{\langle \epsilon \rangle} \right)^{2/3} & \zeta \rightarrow \zeta_l \\ \sqrt{\frac{2}{\langle \epsilon \rangle}} \sqrt{\zeta} - \frac{\sigma^2}{4\zeta \langle \epsilon \rangle} + \mathcal{O} \left(\frac{1}{\zeta^{3/2}} \right) & \zeta \gg 1 \end{cases} \quad (2.43)$$

and where ζ_l is the spinodal point for the localized phase, given by:

$$\zeta_l = \frac{3}{2} \left(\frac{\sigma^4}{\langle \epsilon \rangle} \right)^{1/3} \quad (2.44)$$

Now we can write the microcanonical partition function as:

$$\Omega_N(\mathcal{A}, \zeta) = \frac{e^{N \log \pi}}{2\pi i} \int_{\lambda_0 - i\infty}^{\lambda_0 + i\infty} d\lambda e^{N[a\lambda - \log \lambda]} \left[e^{-N^{1/3}\chi(\zeta)} + e^{-N^{1/3}\zeta^2/2\sigma^2} \right] \quad (2.45)$$

In the thermodynamic limit, the leading contribution is clearly given by the term $N[a\lambda - \log \lambda]$ which determines the value of the saddle point solution λ_0 :

$$\frac{\partial}{\partial \lambda} [a\lambda - \log \lambda] = 0 \implies \lambda_0 = 1/a \quad (2.46)$$

and thus:

$$\Omega_N(\mathcal{A}, \zeta) \approx e^{N[1 + \log(\pi a)]} \left[e^{-N^{1/3}\chi(\zeta)} + e^{-N^{1/3}\zeta^2/2\sigma^2} \right] \quad (2.47)$$

where $\sigma^2 = 20a^4$ and:

$$\langle \epsilon \rangle = 2a^2 \quad (2.48)$$

that is the condition identifying the $\beta = 0$ line.

From this we can determine the microcanonical entropy at leading and sub-leading order:

$$S_N(\mathcal{A}, \zeta) = N[1 + \log(\pi a)] - N^{1/3}\Psi(\zeta) \quad (2.49)$$

where the leading term:

$$S_N^{\text{background}}(a) = N[1 + \log(\pi a)] \equiv N s^{\text{background}}(a) \quad (2.50)$$

represents the background entropy and it clearly is an extensive quantity. Instead, the function $\Psi(\zeta)$ is defined as:

$$\Psi(\zeta) = \inf_{\zeta} \{\chi(\zeta), \zeta^2/(2\sigma^2)\} \quad (2.51)$$

This allows us to identify the matching regime easily, since it is clearly given by the value ζ_c of ζ that satisfies the relation:

$$\chi(\zeta_c) = \zeta_c^2/(2\sigma^2) \quad (2.52)$$

2.3 The Josephson Junction Array

The DNLS model (with periodic boundary conditions) can be used to describe a physical system composed of a closed chain of Josephson junctions (JJA). A Josephson Junction is basically formed by two superconducting materials separated by a thin metal or insulating barrier. A current can flow thanks to the tunnelling effect of the Cooper pairs through the barrier.

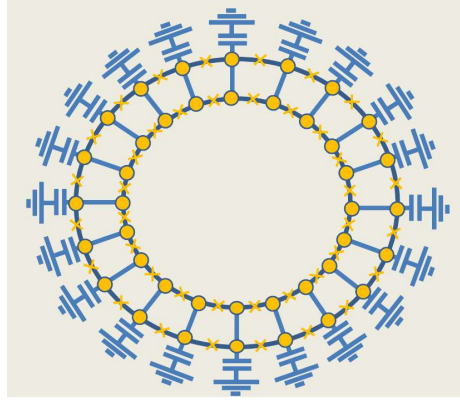


Figure 2.3: Schematic experimental Josephson-Junction array setup in a form of a closed loop.

As we will soon show, varying the thickness of the barrier and the quantity of charge stored in each superconductor, the whole JJA may behave (according to [3]) like an overall superconductor, a metal (ergodic and non-ergodic) or an insulator.

The Hamiltonian that describes the JJA is:

$$H = \sum_{i=1}^n \left[\frac{1}{2} E_C q_i^2 + E_J (1 - \cos(\phi_i - \phi_{i+1})) \right] \quad (2.53)$$

where q_i and ϕ_i are canonically conjugate variables: the q 's represent the charges located in each superconductor, while the ϕ_i 's represent the phases of the superconducting islands. As we will show in Sec. (3), the Hamiltonians Eq. (2.53) and Eq. (2.1) are very similar up to a change of variables.

In [3], a qualitative description of the phase diagram for the model Eq. (2.53) is given; the behavior of the system is governed by the reciprocal values of E_C and

E_J and by the magnitude of the q 's. In particular, the ground state (zero temperature) of the model is governed by the ratio of the Josephson (E_J) and charging (E_C) energies; for $E_J/E_C < \eta$ the system is an insulator and for $E_J/E_C > \eta$ the system is a superconductor. The quantum transition point is given by $\eta \approx 0.63$, and it belongs to the Kosterlitz-Thouless universality class (being a zero-T 1D quantum phase transition, equivalent to a classical thermal 2D phase transition). If we now go to small but finite temperature, then the system exhibits a metallic behaviour, with finite conductivity. If the temperature is raised to $T > E_J$, the system is in a phase usually called *bad metal*, since it has the metallic property of conductance growing with temperature, but its resistance can be arbitrarily high; in this phase the system shows non-ergodic properties. If, instead, the temperature overcomes the critical value $T_C \approx E_J^2/E_C$, the system undergoes a transition in a Many-Body Localized phase.

The qualitative explanation for this behaviour is the following: in a highly excited state $U \gg E_J$ and the leading contribution is given by $E_C q^2 \sim U \gg E_J$. Therefore, the value of the charges $|q_i|$ and charge difference between neighbouring sites $\delta q = q_i - q_{i+1}$ are of the order $q \sim \delta q \sim \sqrt{U/E_C}$. The energy cost for a transfer of a unit charge between two neighbouring sites is then given by $\delta E \sim E_C q$; this is a large quantity if the charge difference is big, i.e. when one of the two sites contains a breather. As a consequence, the charge transfer between a breather and a background site is strongly suppressed, and thus the breather survives for long times.

However, the results presented in [3] are almost qualitative and the numerical simulations performed are not sufficiently accurate to confirm the presence of a phase transition in the classical case in the thermodynamic limit.

3 | A closer look at the JJA and the DNLSE

In this section we will point out the connection between the models Eq. (2.1) and Eq. (2.53) and we will investigate the solutions of the equations of motion (E.o.M.) for the JJA model.

In order to show the connection between the two models, let us begin with the Hamiltonian Eq. (2.1) and make the following change of variables:

$$z_i(t) = \sqrt{q_i(t)} e^{i\phi(t)} \quad (3.1)$$

Since, as we pointed out in Sec. (2), z_i and $-iz_i^*$ are canonically conjugate variables, it is then easy to show that also q_i and ϕ_i are canonically conjugate.

We can thus substitute Eq. (3.1) into Eq. (2.1) to obtain:

$$H = \sum_{i=1}^N 2t\sqrt{q_i q_{i+1}} \cos(\phi_i - \phi_{i+1}) + E_C \sum_{i=1}^N q_i^2 \quad (3.2)$$

Comparing Eq. (3.2) and Eq. (2.53), we then see clearly the similarity between the two models of interest; the only difference at the Hamiltonian level between the two is that, in the JJA model, the hopping term does not have the prefactor $\sqrt{q_i q_{i+1}}$: in the limit of high energy per site this difference is not important, since the leading contribution will be given by the charging term. However, because of Eq. (3.1), in the DNLSE the q_i 's are positive variables, while in the JJA they can also be negative.

We can simply derive the equations of motion for the Hamiltonian Eq. (2.53):

$$\dot{q}_i = -\frac{\partial H}{\partial p_i} = -t (\sin(\phi_i - \phi_{i+1}) - \sin(\phi_{i-1} - \phi_i)) \quad (3.3)$$

and

$$\dot{\phi}_i = \frac{\partial H}{\partial q_i} = E_C q_i \quad (3.4)$$

3.1 Classical Lagrangian for the DNLSE

It may be useful to write also the Lagrangian of the DNLSE. Remind that the equations of motion are given by:

$$i\partial_t \psi_j + (\psi_{j+i} + \psi_{j-1}) + 2|\psi_j|^2 \psi_j = 0 \quad j = 1, \dots, N \quad (3.5)$$

with the usual periodic boundary conditions. These equations of motion are the Euler-Lagrange equations of the following Lagrangian:

$$\mathcal{L} = \sum_{j=1}^N \left[\frac{i}{2} (\psi_j^* \partial_t \psi_j - \psi_j \partial_t \psi_j^*) + (\psi_j \psi_{j+i}^* + \psi_{j+i} \psi_j^*) + |\psi_j|^4 \right] \quad (3.6)$$

It is straightforward to verify that:

$$\begin{aligned} \frac{\partial \mathcal{L}}{\partial \psi_j^*} &= \frac{i}{2} \partial_t \psi_j + \psi_{j+i} + \psi_{j-1} + 2|\psi_j|^2 \psi_j \\ \partial_t \frac{\partial \mathcal{L}}{\partial \partial_t \psi_j^*} &= -\frac{i}{2} \partial_t \psi_j \end{aligned} \quad (3.7)$$

thus yielding Eq. (3.5). We can now perform the usual change of variables:

$$\psi_j = \sqrt{A_j} e^{i\phi_j} \quad (3.8)$$

where both A_j and ϕ_j are functions of time. Notice that the second and third terms in the Lagrangian form the Hamiltonian Eq. (2.1), for which we already have the expression in polar coordinates (see Eq. (2.6)). We only have to com-

pute the first term:

$$\begin{aligned}
& \frac{i}{2} (\psi_j^* \partial_t \psi_j - \psi_j \partial_t \psi_j^*) = \\
& = \frac{i}{2} \left(\sqrt{A_j} e^{-i\phi_j} \partial_t \left[\sqrt{A_j} e^{i\phi_j} \right] - \sqrt{A_j} e^{i\phi_j} \partial_t \left[\sqrt{A_j} e^{-i\phi_j} \right] \right) = \\
& = -A_j \partial_t \phi_j
\end{aligned} \tag{3.9}$$

Thus we can rewrite the Lagrangian as:

$$\mathcal{L} = \sum_{j=1}^N \left[-A_j \partial_t \phi_j + 2\sqrt{A_j A_{j+1}} \cos(\phi_j - \phi_{j+1}) + A_j^2 \right] \tag{3.10}$$

From this expression we can clearly see the Legendre transform structure that connects Hamiltonian and Lagrangian.

3.2 Inverse participation ratio

In order to investigate whether there is a localization phenomenon during the time evolution of the equations of motion, we introduce the *inverse participation ratio*, defined in the following way:

$$Y_2 \equiv \frac{\left(\sum_{i=1}^N q_i^2 \right)^2}{\sum_{i=1}^N q_i^4} \tag{3.11}$$

This quantity can be used as an order parameter for the localized phase: indeed, if every site has energy of order $\mathcal{O}(1)$, then $Y_2 \sim N$; if, instead, there is a breather of size $\mathcal{O}(N)$ and the background is of order $\mathcal{O}(1)$, then $Y_2 \sim 1$, as one can easily see from the definition.

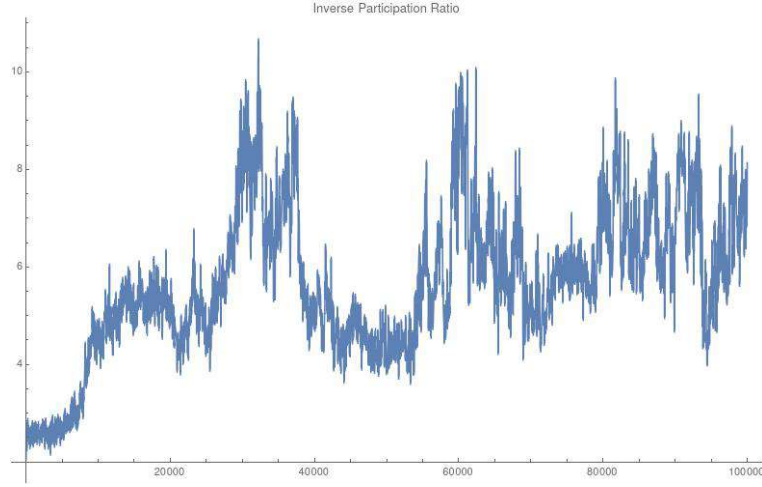


Figure 3.1: The plot of the inverse participation ratio for the JJ array model with $E_J = 4$, $E_C = 1$ and $N = 16$. The plot has been done using a symplectic algorithm, so that energy conservation is insured. The equations of motions have been solved numerically up to $t_{\max} = 100000$. Time is displayed on the horizontal axis. As initial condition, we randomly set the background charges, using the flat distribution between 0 and 1, and then we add two equidistant breathers whose charge is equal to the number of sites. The growth of the IPR with time means that the two breathers are vanishing, and thus the system is thermalizing

3.3 The JJA grand-canonical partition function

As shown in [18], from the grand-canonical partition function it is possible to identify, in the parameter space, the line $\beta = 0$, that separates the ergodic from the non-ergodic phases. Moreover, by means of the inverse Laplace transform, we can find the microcanonical partition function from the grand canonical one. In the case of the DNLSE (Eq. (2.1)) the grand-canonical partition function cannot be performed exactly, but in the case of the JJ array it can, because of the domain of the variables q_k 's, $q_k \in [-\infty, +\infty]$, $\forall k$. Consider the general expression:

$$\Omega_N(\beta, \lambda) = \int_{-\infty}^{\infty} \int_0^{2\pi} \prod_k dq_k d\phi_k \exp[-\beta(\mathcal{H} + \mu\mathcal{A})] \quad (3.12)$$

where μ is the chemical potential and we have defined $\lambda := \beta\mu$. The angular integral can be performed quite easily:

$$\int_0^{2\pi} \prod_k d\phi_k \exp \left[\beta E_J \sum_i \cos(\phi_{i+1} - \phi_i) \right] = (2\pi)^N I_0^N(\beta E_J) \quad (3.13)$$

where I_0 is the modified Bessel function defined as:

$$I_0(x) = \frac{1}{\pi} \int_0^\pi e^{x \cos \theta} d\theta \quad \text{for } \Re(x) > 0 \quad (3.14)$$

Thus we have

$$\Omega_N(\beta, \lambda) = (2\pi)^N I_0^N(\beta E_J) \int_{-\infty}^{\infty} \prod_k dq_k \exp \left[-\beta \sum_j E_C \frac{q_j^2}{2} - \beta\mu \sum_j q_j \right] \quad (3.15)$$

that is easily done yielding:

$$\Omega_N(\beta, \lambda) = \left[2(\pi)^{3/2} I_0(\beta E_J) \sqrt{\frac{2}{\beta E_C}} e^{\frac{\beta\mu^2}{2E_C}} \right]^N \quad (3.16)$$

In order to find the microcanonical partition function, we have to compute two inverse Laplace transforms, namely:

$$Z_N(E, \Lambda) = \frac{1}{2\pi i} \int_{\beta_0 - i\infty}^{\beta_0 + i\infty} \frac{1}{2\pi i} \int_{\lambda_0 - i\infty}^{\lambda_0 + i\infty} d\beta d\lambda e^{\lambda\Lambda} e^{\beta E} \Omega_N(\beta, \lambda) \quad (3.17)$$

Since we are interested in the high energy limit of this expression, we can neglect the hopping term in the Hamiltonian, thus giving the partition function:

$$\begin{aligned} \Omega_N(\beta, \lambda) &= \left(\frac{2\pi}{\lambda} \right)^N \left[\sqrt{2\pi} \frac{\lambda}{\sqrt{\beta E_C}} e^{\frac{\lambda^2}{2E_C\beta}} \right]^N \\ &= \exp [N \log (z(\beta, \lambda))] \end{aligned} \quad (3.18)$$

where

$$z(\beta, \lambda) = \frac{(2\pi)^{3/2}}{\sqrt{\beta E_C}} e^{\frac{\lambda^2}{2E_C\beta}} \quad (3.19)$$

We can now perform, firstly, the Laplace transform with respect to β . Notice that, for large q 's, the integral in Eq. (3.18) is dominated by the term proportional to β (remind that $\beta\mu = \lambda$); therefore there may convergence problems

depending on the sign of β , the sign of λ is irrelevant for the analytic properties. As pointed out in [2], the Bromwich integral can be performed by means of a saddle point approximation, where β_0 in Eq. (3.17) has to be the real positive solution of the saddle point equation:

$$\frac{E}{N} = -\frac{1}{z(\beta, \lambda)} \frac{\partial z(\beta, \lambda)}{\partial \beta} \quad (3.20)$$

If such a real positive solution exists, then β_0 can be regarded as the inverse temperature of the system and we can write:

$$\Omega_N(E, \lambda) \approx \exp[\beta_0 E + N \log(z(\beta_0, \lambda))] \quad (3.21)$$

If, instead, such real positive solution does not exist, then one has to solve the saddle point integral more carefully, as shown in [2]. In our case, however, we find that Eq. (3.20) reduces to the simple equation:

$$\beta^2 - \frac{N}{2E} \beta - \frac{N\lambda^2}{2EE_C} = 0 \quad (3.22)$$

that always has two real solutions and one of them is always positive:

$$\beta_0 = \frac{\frac{N}{2E} + \sqrt{\frac{N^2}{4E^2} + 2\frac{N\lambda^2}{EE_C}}}{2} \quad (3.23)$$

Therefore we can conclude that the negative temperature states that are present in the DNLSE do not appear here, because the now the charges can be negative (this corresponds to Cooper pairs holes).

Notice that this result ensures that the Josephson Junction Array model do not present a localization phenomenon analogous to the DNLSE one, contrarily to what has been claimed in [3], at least at the classical level. Recently, also Flach et al. in [21], have found, analysing the ergodization time T_E , that the concept of ergodicity is preserved in the JJA model and statistical physics continues to work. The ergodization time T_E is related to the properties of the statistics of charge fluctuation times: even if T_E grows anomalously fast reaching the integrable limit $E_J \rightarrow 0$, the dynamics stays ergodic and T_E is finite. Moreover, in [22], the authors have been able to conclude that the JJA model does not present a Gibbs - non-Gibbs transition line ($\beta = 0$ line) also at the quantum level, because of the possibility for the q 's to take all integer values.

3.4 Geometric construction

The same result can be seen in an alternative way, using a geometric construction.

If we consider the full DNLSE Hamiltonian Eq. (2.1), we see from the expression for the microcanonical partition function (see Eq. (2.11)) that the allowed values of the charges, in the high energy limit, must satisfy two constraints, namely $\sum_{i=1}^N \rho_i^2 = \mathcal{A}$ and $\sum_{i=1}^N \rho_i^4 = E$. By means of the trivial change of variables $x_i \equiv \rho_i^2$, we see that the quantities $\{x_i\}_{i=1,\dots,N}$ are positive and moreover they have to belong to the intersection between the standard $N - 1$ -simplex Δ^{N-1} and the $N - 1$ -sphere S^{N-1} , respectively described by the equations:

$$\begin{aligned} \sum_{i=1}^N x_i &= \mathcal{A}, \quad x_i \geq 0 \quad \forall i \\ \sum_{i=1}^N x_i^2 &= E \end{aligned} \tag{3.24}$$

Notice that, in this picture, the number of dimensions of the embedding space for Δ^{N-1} and S^{N-1} is equal to the size of the lattice of the model. The set described by Eqs. (3.24) can be easily visualized in the $N = 2$ and $N = 3$ case (see Fig. (3.2a) and Fig. (3.2b) respectively). It is clear that, varying the value of the total energy keeping the amplitude fixed, the intersection between Δ^{N-1} and S^{N-1} can be connected (i.e. a circle on the simplex) or not connected, forming three distinct arcs in the $N = 3$ case, as in Fig. (3.2b). In the latter case, one of three sites has much more energy than the other two and thus it can be interpreted as a breather. We have to notice, however, that the constraint $\sum_{i=1}^N \rho_i^4 = E$ represents energy conservation only if the hopping term is not present, i.e. in the high energy limit, where the transition to negative temperatures occurs.

Things become more complicated in higher dimensions; indeed, $N = 3$ has to be regarded as a particular case, since the intersection between Δ^2 and S^2 becomes a disconnected manifold when the hypersphere is tangent to the boundary of the simplex. This is not true in higher dimensions. Let us consider, for

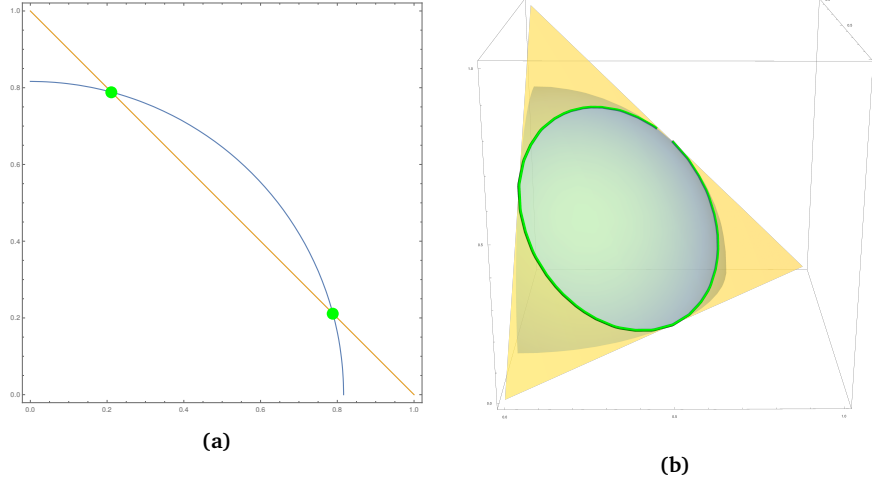


Figure 3.2: Intersection between the sphere S^{N-1} and the standard simplex Δ^{N-1} for $N = 2$ (Fig. (3.2a)) and $N = 3$ (Fig. (3.2b)). In Fig. (3.2a) the intersection between the circle and the segment is already disconnected. In Fig. (3.2b), instead, the transition point is represented; for larger values of the radius of the sphere, the intersection becomes disconnected.

instance, the $N = 4$ case: in order to visualize the situation we consider the hypervolume contained between the hypersphere S^3 and the simplex Δ^3 and we then project it on the hyperplane orthogonal to one of the basis vector of \mathbb{R}^4 . We obtain the relevant cases depicted in Fig. (3.3) and Fig. (3.4).

In particular, in Fig. (3.3) it is shown the case in which the hypersphere is cut by the boundary of the simplex $\partial\Delta^4$, but, differently from the $N = 3$ case, this is not enough to guarantee that the available surface for the variables is disconnected: this happens in Fig. (3.4). It is quite easy to determine analytically the relation that \mathcal{A} and E must satisfy in order to realize the conditions represented in Fig. (3.3) (condition 1.) and Fig. (3.4) (condition 2.). This can be done in the following way:

1. We have to determine the relation between e and a^2 so that the hypersphere is tangent to the boundary of the simplex. This is achieved by setting equal to zero one of the q 's and, by symmetry, setting the remaining $N - 1$ equal to each other, that is:

$$\begin{aligned} E &= (N - 1)x^2 \\ \mathcal{A} &= (N - 1)x \end{aligned} \tag{3.25}$$

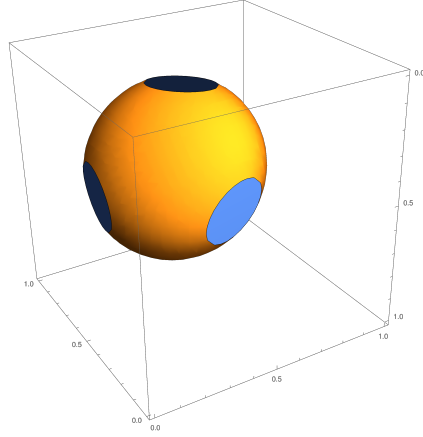


Figure 3.3: Projection on \mathbb{R}^3 of the 2-dimensional surface embedded in \mathbb{R}^4 that represents the intersection between S^{N-3} and Δ^{N-3} . The orange part represents the surface that can be visited by the variables of the problem, while the blue part the one that cannot be visited (is the surface that is cut by $\partial\Delta^4$). Notice that, in this case, the orange part is connected. The intersection between hypersphere and simplex is non-trivial for $e \geq 4/3a^3$.

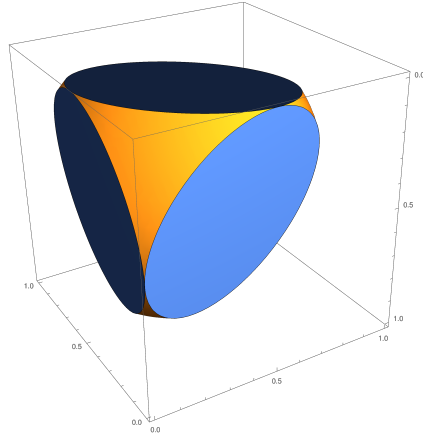


Figure 3.4: The same geometric construction represented in Fig. (3.3) but for a larger value of E ; in particular the value of E has been tuned to the minimum value for which the available surface for the variables is disconnected.

that yields to:

$$e = \frac{N}{N-1} a^2 \quad (3.26)$$

This relation is indeed verified in the cases plotted in Fig. (3.2) and Fig. (3.3).

2. Now we have to determine the relation that relates e to a^2 for which the

intersection between hypersphere and simplex is not connected. This can be done by imposing that $N-2$ of the q 's vanish and, by symmetry, setting equal to each other the remaining two (this is a naive argument, the proof will be given below):

$$\begin{aligned} E &= 2x^2 \\ \mathcal{A} &= 2x \end{aligned} \tag{3.27}$$

and thus:

$$e = \frac{N}{2}a^2 \tag{3.28}$$

With the help of *Mathematica* this has been verified for $N = 3, 4, 5$. Notice how Eq. (3.26) and Eq. (3.28) coincide for $N = 3$ as we described earlier. Notice also that for $N = 4$ this reduces to $e = 2a^2$, which is the condition for negative temperature states in the DNLSE; this is only an accident and this identification is only true for $N = 4$.

The results just presented and motivated quite naively have been demonstrated by a group of mathematicians of the ICTP -The Abdus Salam International Centre for Theoretical Physics, led by prof. Claudio Arezzo. We discussed with him our problem and he recently announced us to have a complete proof. Unfortunately a paper has not yet been published, but it is in preparation.

Therefore we have learned that the cases $N = 3$ and $N = 4$ are geometrically peculiar and in general the three phenomena:

- hypersphere tangent to the boundary of the simplex;
- $\beta = 0$ -line, identifying the transition line for non-Gibbs states;
- disconnection of the intersection between hypersphere and simplex

are distinct. As a consequence, the localization transition described in [2] does not happen when the intersection becomes disconnected, but for smaller values of e . Let us consider, then, the case $2a^2 < e < N/2a^2$; even though the intersection is classically connected, the dynamics of the system takes an enormous amount of time to visit a region different from the initial state one. This is due to the fact that the path connecting two such regions represents an entropic barrier for the classical motion. This means that, even if there are classical trajectories connecting two such regions, their number is strongly suppressed with

respect to the number of classical trajectories that remain in the same region. The name “entropic” here refers to the fact that the number of ways for passing between two regions is very small, even though different from zero. Indeed, the multi-breather states that are observed in the DNLSE last for long-times (usually referred to as “astronomical times”) but they can eventually move.

The presence of the entropic barrier is, however, due to the boundaries of the simplex: if, instead of a simplex, we would have a hyperplane, cases 1. and 2. would never happen and, consequently, there would be no entropic barrier. This is the case of the JJ array model: in fact, as we already mentioned earlier, it has an important difference with respect to the DNLSE: the charges are allowed to assume negative values, because of the possibility of having Cooper pairs holes in the superconductor. This drastically changes the geometric construction we have just described, since now the surface that represents the conservation of the amplitude \mathcal{A} is not a (standard) simplex, but a hyperplane. Accordingly, the intersection between this hyperplane and the hypersphere is always connected, and thus there is no negative temperature phase, as we pointed out computing the partition function, because of the absence of entropic barriers.

This can be seen in Fig. (3.5): in this plot we show the value of the charges of a 3-site JJA system during time evolution: it is interesting to notice that, with the initial conditions used, the DNLSE would be localised. This can be seen in Fig. (3.6a): the area between the couples of arcs is the available surface to the charges, that are also bonded to stay on the simplex. Therefore if the initial condition sets the initial value of the charges to a point in the upper sector, during time evolution the charges remain in that sector. The situation is different in the JJA case (see Fig. (3.6b)).

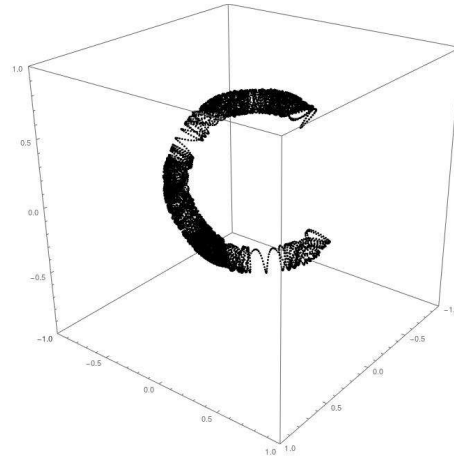


Figure 3.5: Plot of the values of the charges $q_1(t)$, $q_2(t)$, $q_3(t)$ during time evolution. The initial condition is given by the values $q_1(0) = \frac{1}{6}(2 - \sqrt{2})$, $q_2(0) = \frac{1}{6}(2 - \sqrt{2})$ and $q_3(0) = \frac{1}{3}(1 + \sqrt{2})$, $E_J = 0.04$, $E_C = 2$ and $t_{\text{max}} = 10000$, which satisfies $e > 3/2a^2$.

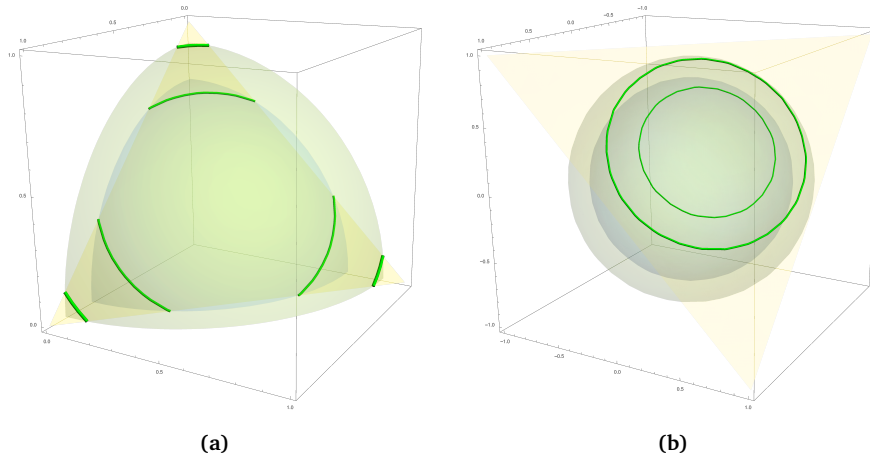


Figure 3.6: Plot of the different bonds for the DNLSE (Fig. (3.6a)) and the JJA (Fig. (3.6b)) models with the same initial conditions. It is clear that the DNLSE is localised in this case, while the JJA is not (here $e > 3/2a^2$), as effectively results from the simulation of the dynamics (see Fig. (3.5)).

3.5 Upper and lower bounds to the total energy for the DNLSE

For a fixed value of the total charge $\mathcal{A} = \sum_i q_i$ and a given N , the range of the possible values of the total energy $E = \sum_i q_i^2$ is easily found by considering two limiting cases:

- $q_1 = q_2 = \dots = q_N = \frac{\mathcal{A}}{N}$ gives the minimum value of the energy;
- $q_i = \mathcal{A}$ and $q_j = 0 \forall j \neq i$ gives the maximum value of the energy.

Using the construction presented in the previous section, we can give a simple geometrical interpretation to these bounds. As before, we are still neglecting the hopping contribution: the correction that takes it into account will be given in the next section. The smallest value of the total energy is given by the radius of the smallest hypersphere that has a non-empty intersection with the simplex. This is obtained by setting the radius of the hypersphere equal to the distance of the simplex from the origin:

$$d_{\text{hyp}}(\mathcal{O}) = \frac{\mathcal{A}}{\sqrt{N}} \equiv \sqrt{E_{\text{min}}} \implies E_{\text{min}} = \frac{\mathcal{A}^2}{N} \quad (3.29)$$

Obviously this coincides with the case in which we set all the charges equal, i.e. at the centre of the simplex.

The maximum value is also easily found, since it is obtained when the vertices of the simplex belong to the hypersphere, and thus:

$$E_{\text{max}} = \mathcal{A}^2 \quad (3.30)$$

Therefore we have the condition:

$$\frac{\mathcal{A}^2}{N} \leq E \leq \mathcal{A}^2 \quad (3.31)$$

in the limit of negligible hopping term. If we introduce the energy and amplitude density $e = E/N$ and $a = \mathcal{A}/N$ as in Sec. (2), we find the relation:

$$a^2 \leq e \leq a^2 N \quad (3.32)$$

Notice that the $\beta = 0$ line, the critical line for the transition to the localized phase, is identified by the equation:

$$e = 2a^2 \quad (3.33)$$

(see Eq. (2.48) or [23]) i.e. for specific energies very close to E_{\min}/N in the thermodynamic limit.

3.5.1 Modified lower bound with hopping contribution

In the previous sections we presented a geometric construction that allowed us to visualize the parameter space of the DNLSE, but we did it in the limit of high energy, i.e. for negligible hopping contribution. This is the relevant limit that we are interested in for the DNLSE. However, we can extend the treatment to the case of non-negligible hopping term, providing corrections to the total energy. In particular, consider the Hamiltonian in Eq. (2.6): the hopping term for $E \sim E_{\min}$ can be at most $|H_{\text{hopp}}| = 2\mathcal{A}$, when the charges are all equal to \mathcal{A}/N . Therefore:

$$E_{\min} = \frac{\mathcal{A}^2}{N} - 2\mathcal{A} \implies e_{\min} = a^2 - 2a \quad (3.34)$$

and this is the equation for the $\beta = \infty$ line in the phase diagram Fig. (2.1).

Notice that the upper bound is not modified, since it is obtained setting all the charges equal to zero except for one, that is equal to \mathcal{A} ; in that case however, the hopping term vanishes since there is the product of neighbouring charges and at least one of them is always zero. In conclusion we have:

$$a^2 - 2a \leq e \leq Na^2 \quad (3.35)$$

3.6 The particular case $N = 3$

Now we focus on the particular case of the DNLSE with $N = 3$ sites: this is an interesting case since it allows us to visualize the values of the charges located at each site and the time evolution of their values. We will study numerically this case.

First we notice that the charges must satisfy both energy and amplitude conservation. We have already pointed out in Sec. (3.3) that, keeping the value

of the total amplitude fixed and changing the total energy, there is a transition when the intersection between the standard simplex and the sphere is no more a connected line. In that case, however, we have not considered the hopping term. If we want to investigate the time evolution of the charges, we obviously have to keep it, and thus we will consider the following hamiltonian:

$$H = \sum_{k=1}^3 \left(\frac{1}{2} E_C q_k(t)^2 + t \sqrt{q_k(t) q_{k+1}(t)} \cos(\phi_k(t) - \phi_{k+1}(t)) \right) \quad (3.36)$$

Notice that this Hamiltonian coincides with Eq. (2.6) where we have introduced the control parameters E_C and t emulating the ones that are present in the JJ array model. Even if the total amplitude is still conserved in this case, the charges no more satisfy the equation $E = \sum_{i=1}^3 q_i^2$, but the full energy conservation. Therefore the allowed charges no more live on the line depicted in Fig. (3.2b). We should consider, instead, the intersection between the simplex, where the charges are always constrained to stay, with a (sort of) spherical shell with mean squared radius given by the total energy, modified by a quantity given by $\pm t \sqrt{q_k(t) q_{k+1}(t)}$. Different scenarios may appear if we vary the value of t keeping the value of total energy fixed. For small values of t , localization will persist, since in the worst case scenario, the hopping term can be at most equal to $\pm t\mathcal{A}$; this is obtained maximizing both the absolute value of the cosine (i.e. ± 1) and the value of $\sum_i \sqrt{q_i(t) q_{i+1}(t)}$ (i.e. \mathcal{A}), that is obtained when the three charges describe the centre of the simplex. We can therefore find the value of t , for given total energy E , for which there surely is localization. This is obtained looking for the lowest value of t for which the sphere:

$$\frac{E_C}{2} \sum_{k=1}^3 q_k^2 = E - t\mathcal{A} \quad (3.37)$$

is tangent to the boundary of the simplex

$$\sum_{k=1}^3 q_k = \mathcal{A} \quad (3.38)$$

This is given by the condition:

$$\sqrt{\frac{2(E - t\mathcal{A})}{E_C}} \geq \frac{\mathcal{A}}{\sqrt{2}} \quad (3.39)$$

and thus:

$$t \leq \frac{E}{\mathcal{A}} - \frac{\mathcal{A}E_C}{4} \quad (3.40)$$

Notice that this bound is not very accurate: we have approximated the hopping term with its maximum value, that clearly cannot be reached in the case we are investigating, i.e. when the charges are “isolated” in one corner of the simplex. However, this allows us to conclude that there is localization, because we have considered the worst case scenario.

If t is increased enough, the charge can move to other sectors of the simplex, but still cannot visit the centre of the simplex. This can be done increasing further the value of t . A plot of the possible outcomes is given in Fig. (3.7).

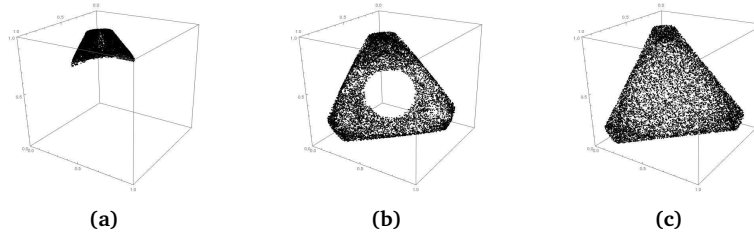


Figure 3.7: Plot of the value of the charges q_1 , q_2 and q_3 for different values of t . In particular in Fig. (3.7a) $t = 0.8$, in Fig. (3.7b) $t = 1$ and in Fig. (3.7c) $t = 1.5$. The initial conditions are $q_1(0) = \frac{1}{6}(2 - \sqrt{2})$, $q_2(0) = \frac{1}{6}(2 - \sqrt{2})$, $q_3(0) = \frac{1}{3}(1 + \sqrt{2})$ and $E_C = 10$. The equations of motion have been solved numerically till $t_{\max} = 10000$.

4 | Quantum DNLSE

In the previous sections we focused our attention on the Discrete Non-Linear Schrödinger Equation, which is a classical model that presents a peculiar localization transition into a negative temperature phase characterized by non-gibbsian states. In this section our aim is to quantize the DNLSE, that will give us the Bose-Hubbard model, and show that the localization transition of the DNLSE is present also in this context.

In order to quantize the DNLSE, we consider then the Hamiltonian of Eq. (2.1) and we introduce the bosonic creation and annihilation operators ψ_i and ψ_i^\dagger with commutation relations:

$$[\psi_i, \psi_j^\dagger] = \delta_{ij} \quad (4.1)$$

and

$$[\psi_i, \psi_j] = 0 \quad [\psi_i^\dagger, \psi_j^\dagger] = 0 \quad (4.2)$$

Therefore the Hamiltonian becomes:

$$\mathcal{H} = \frac{t}{2} \sum_{i=1}^N (\psi_i^\dagger \psi_{i+1} + \psi_{i+1}^\dagger \psi_i) + \frac{E_C}{2} \sum_{i=1}^N \psi_i^\dagger \psi_i \psi_i^\dagger \psi_i + g \sum_{i=1}^N \psi_i^\dagger \psi_i \quad (4.3)$$

where the couplings t and E_C have been introduced in analogy with the Josephson Junction Array model.

The term proportional to g has been introduced because of the ambiguity in the quantization of the quartic term: it can be defined indeed as $\sum_{i=1}^N \psi_i^\dagger \psi_i \psi_i^\dagger \psi_i$ or $\sum_{i=1}^N \psi_i^\dagger \psi_i^\dagger \psi_i \psi_i$ and they differ by $\sum_{i=1}^N \psi_i^\dagger \psi_i$. The g -term does not modify

the properties of the Hamiltonian, however, since the total number operator:

$$\mathcal{A} = \sum_{i=1}^N \psi_i^\dagger \psi_i = \sum_{i=1}^N \hat{n}_i \quad (4.4)$$

is still conserved, as one can easily verify performing the commutator between \mathcal{H} and \mathcal{A} that gives:

$$[\mathcal{H}, \mathcal{A}] = 0 \quad (4.5)$$

in virtue of the periodic boundary conditions. Notice that in Eq. (4.4) we have introduced the quantity $\hat{n}_i := \psi_i^\dagger \psi_i$, that is the number operator for the i -th site.

4.1 Symmetries, basis vectors and Hilbert space

The Hamiltonian Eq. (4.3) has several symmetries. The first one is a $U(1)$ global gauge symmetry that acts as:

$$\begin{aligned} \psi_i &\rightarrow \psi_i e^{i\theta} \\ \psi_i^\dagger &\rightarrow \psi_i^\dagger e^{-i\theta} \\ \hat{n}_i &\rightarrow \hat{n}_i \end{aligned} \quad (4.6)$$

There is then the translation symmetry, that acts as:

$$\begin{aligned} \psi_i &\rightarrow \psi_{i+1} \\ \psi_i^\dagger &\rightarrow \psi_{i+1}^\dagger \end{aligned} \quad (4.7)$$

The Hamiltonian is left invariant thanks to the periodic boundary conditions, as one can readily verify. We can introduce the following operator:

$$\hat{K} \equiv \sum_{q=0}^{N-1} \left(\frac{2\pi q}{N} \right) b_q^\dagger b_q \quad (4.8)$$

with the definition:

$$b_q^\dagger \equiv \frac{1}{\sqrt{N}} \sum_{j=1}^N e^{i(2\pi q j/N)} \psi_j^\dagger \quad (4.9)$$

The operator \hat{K} is the total quasi-momentum, while the operators b_i^\dagger and b_i are, respectively, the creation and annihilation operators for the Bloch states. In

terms of the operator \hat{K} we can express the action of the translations as:

$$\begin{aligned} e^{-i\hat{K}}\psi_i e^{i\hat{K}} &= \psi_{i+1} \\ e^{-i\hat{K}}\psi_i^\dagger e^{i\hat{K}} &= \psi_{i+1}^\dagger \end{aligned} \quad (4.10)$$

Therefore, the translation symmetry is associated with the conservation of the total quasi-momentum \hat{K} .

The third symmetry of the system is the reflection symmetry, that transforms the creation and annihilation operators as:

$$\begin{aligned} \psi_i &\rightarrow \psi_{N-i} \\ \psi_i^\dagger &\rightarrow \psi_{N-i}^\dagger \end{aligned} \quad (4.11)$$

Notice that the combination of translation and reflection symmetry gives the dihedral group Dih_N , and thus the Hamiltonian Eq. (4.3) is invariant under the group \mathcal{G} :

$$\mathcal{G} = \text{U}(1) \otimes \text{Dih}_N \quad (4.12)$$

Let us focus now on the basis vectors for the Hilbert space of our model: we can introduce the following operator: we can choose as a natural basis for our model the occupation number basis $\{|n_1, \dots, n_N\rangle\}$, that is defined as:

$$\hat{n}_i |n_1, \dots, n_N\rangle = n_i |n_1, \dots, n_N\rangle \quad (4.13)$$

and, as usual:

$$\begin{aligned} \psi_i |\dots, n_i, \dots\rangle &= \sqrt{n_i} |\dots, n_i - 1, \dots\rangle \\ \psi_i^\dagger |\dots, n_i, \dots\rangle &= \sqrt{n_i + 1} |\dots, n_i + 1, \dots\rangle \end{aligned} \quad (4.14)$$

For a given number of bosons $n_1 + \dots + n_N = N_b$, the dimension of the Hilbert space of the system \mathbb{H} is easily obtained:

$$D_{\mathbb{H}} = \binom{N_b + N - 1}{N_b} = \frac{(N_b + N - 1)!}{N_b!(N - 1)!} \quad (4.15)$$

that is the number of ways for arranging N_b objects in N places. In Appendix (D) we show how we generated the basis elements in the algorithm used to study the time evolution of a given initial condition.

4.2 The Quantum dynamics

As we did for the classical case, we would like to study the dynamics governed by the hamiltonian Eq. (4.3). The algorithm we use to this aim consists of a base generator, based on the procedure explained in Appendix (D). After the generation of the basis, we generate the Hamiltonian Eq. (4.3) by means of the algorithm presented in Appendix (D). Once the Hamiltonian is obtained, we solve numerically the time-dependent Shrödinger equation for a given initial condition. In particular, in order to compare the quantum results with the classical ones, we will set analogous initial conditions.

4.2.1 The $N = 3$ case

As we did for the classical case, also for the quantum case we will focus on the dynamics of a system described by the hamiltonian Eq. (4.3) on a 3-site lattice with p.b.c. with a given number of bosons (that will not change since the hamiltonian conserves the total number of particles). Let us remind that in the classical case, when the value of t is sufficiently small, the dynamics is necessarily localized, since a charge (i.e. particle) transfer between neighbouring sites would require to overcome a “potential barrier” due to the conservation of both energy and amplitude. In order to pass from a site to another, keeping the total amplitude conserved, energy should not be conserved, allowing the system to overcome the “potential barrier”. However, in the quantum system, even when we are in the regime where the classical dynamics is localized, we expect to have charge transfer due to tunnelling effect. In order to look into this phenomenon, we have to focus on the mean number of bosons per site during time evolution, that is, we have to look, during the dynamics, to the quantity:

$$n(k, t) = \sum_{\substack{n_1, n_2, n_3 \\ n_1 + n_2 + n_3 = N_b}} p(n_1, n_2, n_3; t) \langle n_1, n_2, n_3 | \hat{n}_k | n_1, n_2, n_3 \rangle \quad (4.16)$$

where $n(k, t)$ is the mean number of bosons at site k at time t and $p(n_1, n_2, n_3; t)$ is the probability that, a time t , the system is in the state $|n_1, n_2, n_3\rangle$. The probability $p(n_1, n_2, n_3; t)$ is obtained by the solution of the time-dependent Shrödinger equation. In Appendix (D) we explain how to accomplish this goal algorithmically. Notice that the quantity $n(k, t)$ is the analogous of $q_k(t)$ in the classical system. We can thus define the Inverse Participation Ratio also for the

quantum case as:

$$Y_2(t)^{(Q)} = \frac{\left(\sum_{k=1}^N n(k, t)^2\right)^2}{\sum_{k=1}^N n(k, t)^4} \quad (4.17)$$

In order to better clarify the meaning of the Inverse Participation Ratio, we show in Fig. 4.1 and Fig. 4.2 the IPR for a $N = 3$ -site Bose-Hubbard model. From Fig. 4.1 it is evident that, at least for small values of N , the IPR can be quasi-periodic in the quantum system. In Fig. 4.2 we show the value of IPR and $n(k, t)$ for $k = 1, 2, 3$: it is clear that, the IPR is maximum when all the sites have the same mean occupation number. Conversely, the IPR is minimum when the occupation of the sites is the most uneven possible.

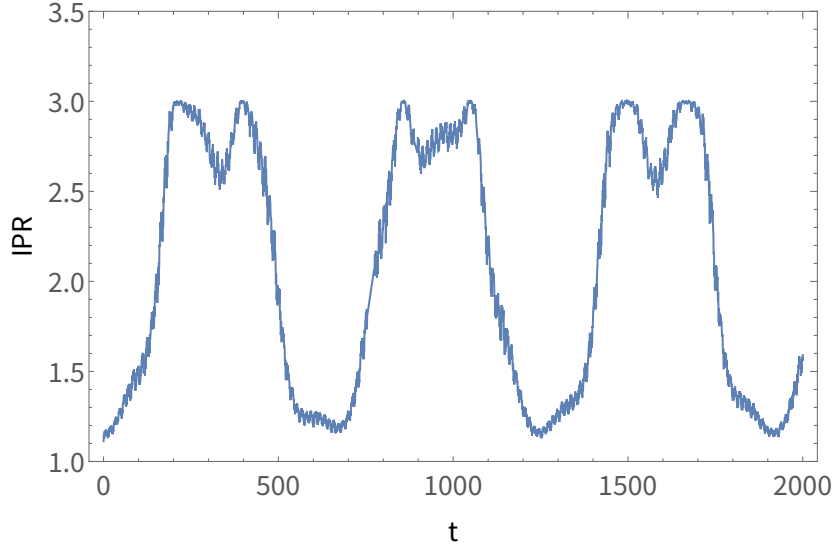


Figure 4.1: Plot of the Inverse Participation Ratio as a function of time for a system of $N_b = 8$ bosons and $N = 3$ sites, with initial configuration $|6, 1, 1\rangle$. The parameters in the Hamiltonian are set equal to: $E_C = 2$, $t = 0.8$ and the Schrödinger equation is solved till $t_{\max} = 2000$.

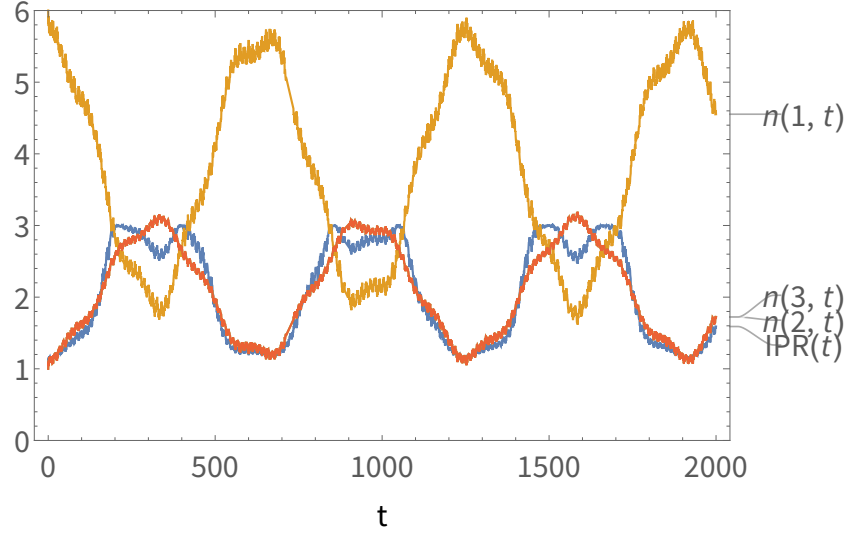


Figure 4.2: Plot of the Inverse Participation Ratio (blue), $n(1, t)$ (orange) and $n(2, t) \equiv n(3, t)$ (red). The initial conditions and the parameters are the same of Fig. 4.1

It is natural to expect that the IPR period, that can be easily found from Fig. 4.1, depends on the ratio t/E_C and on the number of bosons on the lattice. For instance, the bigger the ratio t/E_C (or t with fixed E_C) the smaller will be the IPR period, as bosons can move more easily thanks to a bigger hopping term. Instead, for larger values of N_b , we expect the IPR period to be larger, since the energy differences between neighbouring sites can be larger and thus off-resonance. In Fig. 4.3 we show the results of the numerical simulations performed for different values of N_b ; the IPR period has the features expected.

4.3 Quantum tunnelling

As we anticipated in the previous section, we expect that in the quantum regime there is the possibility of charge transfer between disconnected sectors of the space of variables because of quantum tunnelling. In order to be more quantitative, in this section we are interested in performing the amplitude for the transport of charge between two neighbouring sites $|Q, 0, 0, \dots\rangle \rightarrow |0, Q, 0, \dots\rangle$. To do this, we begin with the Hamiltonian Eq. (4.3) (we set $g = 0$, this makes

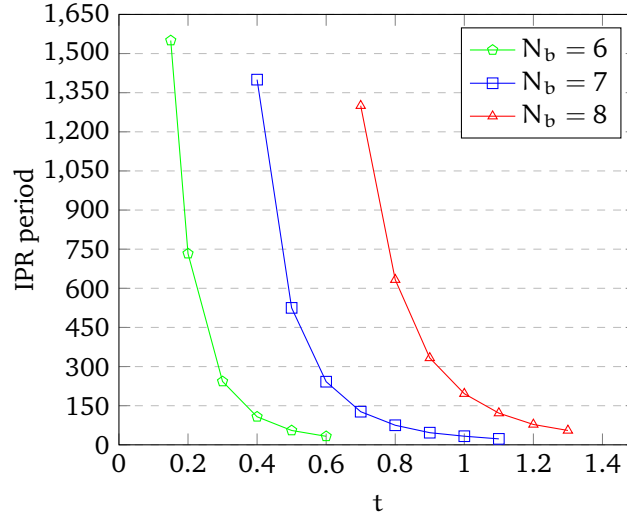


Figure 4.3: Plot of the dependence of the IPR period on the value of t for different values on N_b . We used the following initial conditions: $N_b = 6 \rightarrow |4, 1, 1\rangle, N_b = 7 \rightarrow |5, 1, 1\rangle, N_b = 8 \rightarrow |6, 1, 1\rangle$. In all cases we used $E_C = 2$ and $N = 3$

no difference) and we perform the canonical change of variables:

$$\begin{aligned}\psi_i &= \sqrt{q_i} e^{i\phi_i} \\ \psi_i^\dagger &= e^{-i\phi_i} \sqrt{q_i}\end{aligned}\quad (4.18)$$

with:

$$[q_i, \phi_j] = i\delta_{ij}\quad (4.19)$$

To simplify the analysis, let us consider the charge transfer involving only two sites: in that case the Hamiltonian reduces to:

$$\mathcal{H} = t(\sqrt{q_1} e^{i(\phi_1 - \phi_2)} \sqrt{q_2} + \text{h.c.}) + \frac{E_C}{2} (q_1^2 + q_2^2)\quad (4.20)$$

This simplification is motivated by the fact that, in the full Hamiltonian, the hopping term couples neighbouring sites; this means that, at least at leading order in perturbation theory, the transfer of particles occurs between adjacent sites. Moreover, we will perform a semi-classical calculation, and therefore we can safely neglect the commutator contributions, yielding the effective Hamiltonian:

$$\mathcal{H}^{(\text{eff})} = 2t\sqrt{q_1 q_2} \cos(\phi_1 - \phi_2) + \frac{E_C}{2} (q_1^2 + q_2^2)\quad (4.21)$$

We introduce now another set of canonically conjugate variables, defined as follows:

$$\begin{aligned}\phi_+ &= -\frac{\phi_1 + \phi_2}{\sqrt{2}}; & \phi_- &= -\frac{\phi_1 - \phi_2}{\sqrt{2}} \\ q_+ &= \frac{q_1 + q_2}{\sqrt{2}}; & q_- &= \frac{q_1 - q_2}{\sqrt{2}}\end{aligned}\quad (4.22)$$

that clearly satisfy the relation:

$$[\phi_a, q_b] = i\delta_{ab} \quad (4.23)$$

with $a, b = \pm$. Therefore the Hamiltonian becomes:

$$\mathcal{H}^{(eff)} = 2t\sqrt{\frac{q_+^2 - q_-^2}{2}} \cos(\sqrt{2}\phi_-) + \frac{E_C}{2}(q_+^2 + q_-^2) \quad (4.24)$$

We immediately see that (as we already know) the total number of particles $q_+ = \frac{Q}{\sqrt{2}}$ (total charge) is conserved, since there is not the conjugate variable in the Hamiltonian. In the following we will treat q_- as the momentum and ϕ_- as the position. We are interested in finding the probability that, starting with momentum $q_- = Q/\sqrt{2}$, we end up with momentum $q_- = -Q/\sqrt{2}$.

4.3.1 Classical trajectories

Before starting with the calculation of the quantum tunnelling coefficients, we have to study the classical trajectories allowed in the reduced Hamiltonian we are considering. To do so, let us rewrite the Hamiltonian Eq. (4.24) as:

$$H = t\sqrt{Q^2 - q^2} \cos(2\phi) + \frac{E_C}{4}q^2 = t\sqrt{Q^2 - q^2} \cos(\Phi) + \frac{E_C}{4}q^2 \quad (4.25)$$

where:

$$q = \sqrt{2}q_-, \quad Q = \sqrt{2}q_+, \quad \phi = \phi_-/\sqrt{2}, \quad \Phi = 2\phi \quad (4.26)$$

(q and ϕ are canonically conjugate variables). At the classical level it has a peculiar property when the initial condition is set to be $Q = q$. The trajectories associated to the solution of the equations of motion for the Hamiltonian Eq. (4.25) are given by the contour plot in Fig. (4.4), for different values of the initial energy (i.e. different values of the initial conditions). The separatrix is

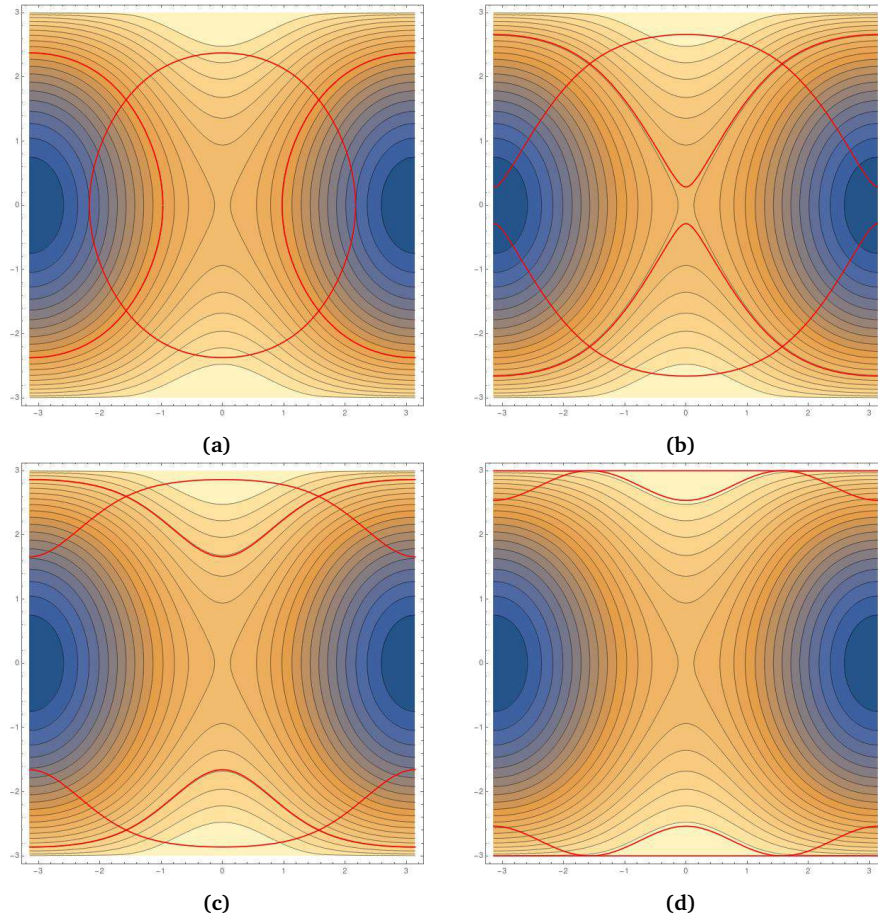


Figure 4.4: The contour plot shows the trajectory associated to the Hamiltonian Eq. (4.24). In red we have plotted the explicit solution to the equation of motion (the one that follows the contour plot lines) and the solution to the equations of motion if we invert the sign in front of the square root (see text).

the trajectory for which we pass from close to open orbits. The red lines are obtained by solving for q , the momentum of our system, the equation:

$$\mathbb{E} = t\sqrt{Q^2 - q^2} \cos(\Phi) + \frac{1}{4}q^2 \quad (4.27)$$

where we set, for simplicity, $E_C = 1$. However, we should be careful in solving this equation; indeed we have:

$$t \cos(\Phi) \sqrt{Q^2 - q^2} = \mathbb{E} - \frac{1}{4}q^2 \quad (4.28)$$

where, by definition, $q < Q$. This equation will lead to a second order equation, that has two solutions in general. However, depending on the sign of $\cos(\phi)$, we will have to take only one of them:

$$\begin{aligned} &\text{for } \Phi \in \left[-\frac{\pi}{2}, \frac{\pi}{2}\right] \rightarrow q^2 < 4E \\ &\text{for } \Phi \in \left[-\pi, -\frac{\pi}{2}\right] \wedge \left[\frac{\pi}{2}, \pi\right] \rightarrow q^2 \geq 4E \end{aligned} \quad (4.29)$$

This conditions select only one solution (namely the correct one). In Fig. (4.4) the red line following the contour lines is the correct solution. The other red line is the wrong solution, the one obtained by taking the wrong signs. We plotted it anyway because it gains an important role when $q = Q$; this situation is represented in Fig. (4.4d). As it is clear from the conditions Eq. (4.29), the two solutions (the right and wrong one) meet at $\Phi = \pm\pi/2$. The angle between the tangents at the intersection points become smaller as q approaches Q , being zero for $q = Q$. At this point, it happens that the solution to the equations of motion is no more unique: in fact, one of them is given by ordinary solution, that now assumes the form:

$$q = \begin{cases} \pm Q & \text{if } \Phi \in \left[-\pi, -\frac{\pi}{2}\right] \wedge \left[\frac{\pi}{2}, \pi\right] \\ \pm\sqrt{Q^2 - 16t^2 \cos^2(\phi)} & \text{if } \Phi \in \left[-\frac{\pi}{2}, \frac{\pi}{2}\right] \end{cases} \quad (4.30)$$

In addition, there is also another possible solution that conserves the energy and that solves the equations of motion, that is:

$$q = \pm Q \quad \forall \Phi \quad (4.31)$$

This is better shown in Fig. (4.5).

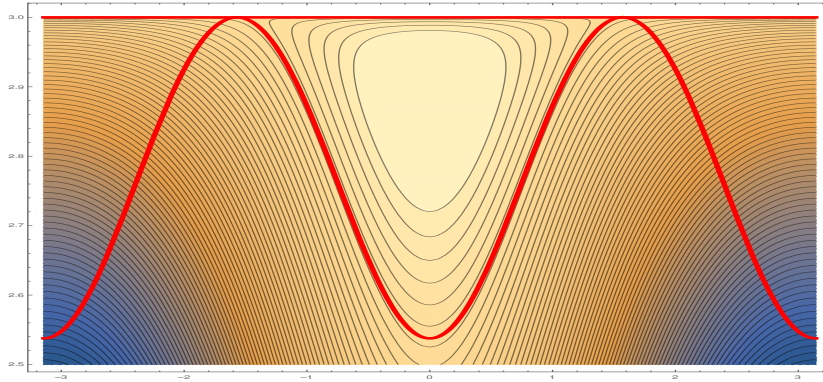


Figure 4.5: Trajectories for initial condition $q_0 = Q$

Therefore, for $\Phi \in [-\frac{\pi}{2}, \frac{\pi}{2}]$ also the “wrong” solution, the one that one obtains by choosing the wrong signs, is correct. What happens is that the two solutions to the equations of motion Eq. (4.30) constitute another separatrix of the phase space of the system.

4.3.2 Quantum Tunnelling: the general case ($Q \gg 1$)

Having studied the classical trajectories of the Hamiltonian (4.25), we can now proceed by studying the quantum tunnelling coefficients. As it is clear from Eq. (4.23), in our system q represents the momentum and ϕ the position. Since we would like to find the probability for the transition $q \rightarrow -q$ in classically forbidden regions, we have to study the phenomenon of “reflection above a barrier”. The phenomenon we are interested in is represented in Fig. (4.6).

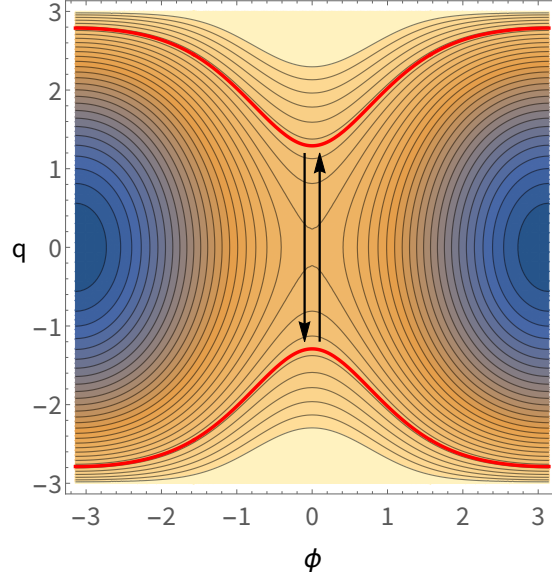


Figure 4.6: The quantum tunnelling phenomenon described in this section represents the transition $q \rightarrow -q$. Since q is the momentum of our system, we will have to calculate the coefficient for the reflection above a barrier.

As we discuss in Appendix (E), the amplitude for this process is given by:

$$|\mathcal{R}(E)|^2 = \exp\left(-\frac{4}{\hbar} \mathcal{I} \int_0^{z_0} dz p(z)\right) \quad (4.32)$$

where $p(z)$ is the momentum of the system and z_0 is such that $p(z_0) = 0$. Consider, then, the Hamiltonian Eq. (4.25) and the initial condition:

$$E = \frac{q^2}{4} + t\sqrt{Q^2 - q^2} \cos(2\phi) \equiv \frac{X}{4} \quad (4.33)$$

and define:

$$X := \hbar Q^2, \quad \cos(2\phi) = Q\kappa \quad (4.34)$$

then the expression for q as a function of κ is given by:

$$q = Q\sqrt{\hbar - 4\kappa t \left(2\kappa t + \sqrt{1 - \hbar + 4t^2\kappa^2}\right)} \quad (4.35)$$

In order to determine the reflection coefficient, we have to integrate over ϕ

Eq. (4.35) from 0 to the value of ϕ such that $q(\phi_0) = 0$, i.e.:

$$q(\kappa_0) = 0 \implies \kappa_0 = \frac{\hbar}{4t} \quad (4.36)$$

Since we are interested in the quantum reflection above the barrier, the value of ϕ_0 corresponding to the value of κ_0 given by Eq. (4.36) is pure imaginary. Therefore we define:

$$2\phi = i\hat{\phi} \implies \kappa = \frac{\cosh(\hat{\phi})}{Q} \quad (4.37)$$

We have to perform:

$$\omega = \int_0^{\hat{\phi}_0/2} d\phi q(\phi) \quad (4.38)$$

Given that:

$$\begin{aligned} d\kappa &= \frac{1}{Q} \sinh(\hat{\phi}) d\hat{\phi} = \frac{1}{Q} \sqrt{Q^2\kappa^2 - 1} d\hat{\phi} = \\ &= \sqrt{\kappa^2 - \frac{1}{Q^2}} d\hat{\phi} \end{aligned} \quad (4.39)$$

Then we find:

$$\omega = \frac{i}{2} \int_0^{\hat{\phi}_0} d\hat{\phi} q = \int_{1/Q}^{\hbar/4t} \frac{d\kappa}{\sqrt{\kappa^2 - \frac{1}{Q^2}}} Q \sqrt{\hbar - 4\kappa t (2\kappa t + \sqrt{1 - \hbar + 4t^2\kappa^2})} \quad (4.40)$$

Notice that the integral:

$$\int_a^{\kappa_0} \frac{d\kappa}{\sqrt{\kappa^2 - a^2}} = \Re \int_0^{\kappa_0} \frac{d\kappa}{\sqrt{\kappa^2 - a^2}} \quad (4.41)$$

where $a = 1/Q$. Now we make the change of variables $a = i\bar{a}$ and thus:

$$\int_a^{\kappa_0} \frac{d\kappa}{\sqrt{\kappa^2 - a^2}} = \Re \int_0^{\kappa_0} \frac{d\kappa}{\sqrt{\kappa^2 + \bar{a}^2}} \quad (4.42)$$

Then we have:

$$\begin{aligned} \int_0^{\kappa_0} \frac{d\kappa}{\sqrt{\kappa^2 + \bar{a}^2}} &= \log\left(\frac{2\kappa_0}{\bar{a}}\right) + \left(\frac{\bar{a}}{2\kappa_0}\right)^2 + \dots \\ \int_0^{\kappa_0} \frac{\kappa d\kappa}{\sqrt{\kappa^2 + \bar{a}^2}} &= (\kappa_0 - \bar{a}) + \frac{\bar{a}^2}{2\kappa_0} + \dots \end{aligned} \quad (4.43)$$

Let us define:

$$f(\kappa) = Q\sqrt{h - 4\kappa t \left(2\kappa t + \sqrt{1 - h + 4t^2\kappa^2} \right)} = Q \left[\sqrt{h} - 2\sqrt{\frac{1-h}{h}}\kappa + \mathcal{O}(\kappa^2) \right] \quad (4.44)$$

Therefore we get:

$$\int_0^{\kappa_0} d\kappa \frac{1}{\sqrt{\kappa^2 + \bar{a}^2}} f(\kappa) = f(0) \log \left(\frac{2\kappa_0}{\bar{a}} \right) + f'(0)(\kappa_0 - \bar{a}) + \mathcal{O}(\bar{a}^2) \quad (4.45)$$

from which:

$$\omega = \frac{Q}{2} \sqrt{h} \log \left(\frac{2\kappa_0}{\bar{a}} \right) - \frac{hQ}{4t} \sqrt{\frac{1-h}{h}} \quad (4.46)$$

and thus, at leading order:

$$|\mathcal{R}(E)|^2 = e^{-4\omega} = \left(\frac{hQ}{2t} \right)^{-2Q\sqrt{h}} = \left(\frac{2t}{Q(2x-1)^2} \right)^{2Q|2x-1|} \quad (4.47)$$

if we set as initial condition $q = Q(2x - 1)$ and use $Q \gg 1$. Notice that the reflection coefficient in Eq. (4.47) goes to zero, for large Q , faster than an exponential. This result qualitatively agrees with the ones found in Sec. (4.2.1), since it justifies the fact that, with the same conditions, the quantum dynamics is less localized than the classical one. This is a consequence of the tunnelling property of quantum systems. Notice that this is the opposite of what happens in systems that display Anderson or many-body localization (see [5]). As we mentioned in the Introduction (Sec. (1.1)), both Anderson and MB localization are phenomena that occur in quantum systems, disappearing in the semi-classical limit, and for strong enough disorder. The localization phenomenon that we are considering in this work is completely different, since our system does not have disorder and the classical case is “more localized” than the quantum one.

4.4 $N = 2$ quantum dynamics

In this section we want to relate the reflection coefficient obtained in the semi-classical calculation performed in Sec. (4.3.2) with the time τ such that:

$$|\langle Qx, Q(1-x) | e^{-iH\tau} | Q(1-x), Qx \rangle|^2 \simeq 1 \quad (4.48)$$

that can be obtained from numerical simulations. In Fig. (4.7a) and Fig. (4.7b) we show how the amplitude in Eq. (4.48) depends on t in two different cases.

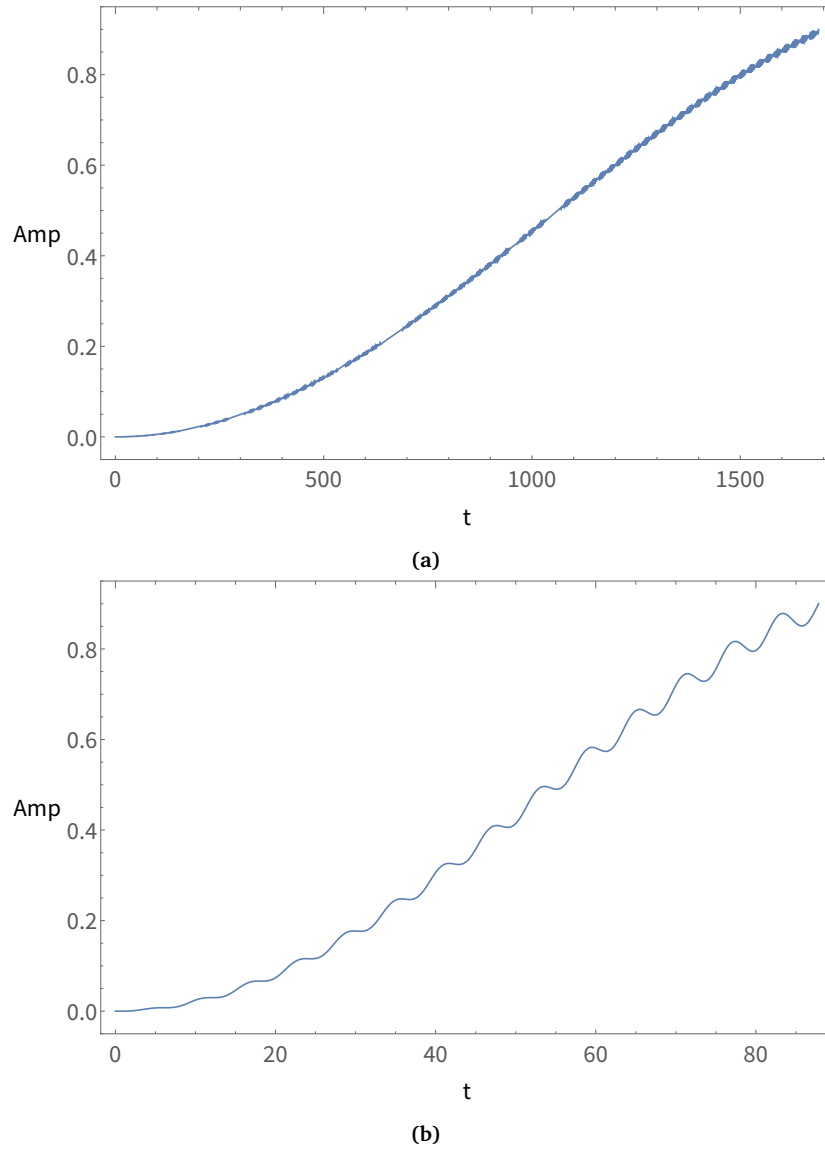


Figure 4.7: Plot of the amplitude $|\langle Qx, Q(1-x) | e^{-iHt} | Q(1-x), Qx \rangle|^2$ as a function of time with initial conditions $t = 0.1$, $Q = 5, x = 1/5$ in Fig. (4.7a) and $t = 0.1$, $Q = 4, x = 1/4$ in Fig. (4.7b).

Since $|R|^2$ is the probability of getting through the barrier (in momentum

space) on a single collision with the wall, the number of collisions needed will be of the order of $|R|^{-2}$, thus one expects that:

$$\tau \simeq \frac{\Delta t(Q, t, E_C)}{|R|^2} \implies \tau |R|^2 \simeq \Delta t(Q, t, E_C) \quad (4.49)$$

where $\Delta t(Q, t, E_C)$ is the proportionality constant between τ and $1/|R|^2$, that in general can depend on Q , t and E_C . Let us introduce the semiclassical time τ_{sc} defined as:

$$\tau_{sc} = \frac{1}{|R|^2} \quad (4.50)$$

since we expect that the time needed to go through the barrier (in momentum space) is proportional to the number of collisions with the wall. One expects that the behaviour of τ as a function of Q will be dominated by a contribution $Q \log Q$ as happens for $|R|^2$. Moreover the $\Delta t(Q, t, E_C)$ dependence on Q , t and E_C can be inferred from the τ/τ_{sc} dependence on the same variables.

At the moment we have been able to obtain few useful data and this is due to two issues: for small values of Q the semiclassical result is not reliable since the system is near the inversion points of the potential, where the semiclassical methods break down. On the other hand, for large value of Q the numerical simulations of the quantum system require much more computational power than the one used in obtaining the results presented.

4.4.1 Leading contribution to the tunnelling time τ

In this subsection we want to show that τ has the same leading contribution on Q as the reflection coefficient $1/|R|^2$ found in Sec. (4.3.2).

Let us remind Eq. (4.47), that we now express in terms of τ_{sc} :

$$\tau_{sc} = \left(\frac{Q(2x-1)^2}{2t} \right)^{2Q|2x-1|} \quad (4.51)$$

Remind also that x is the fraction of particles present in one of the two sites in the initial condition. Since we will fit the numerical results obtained with

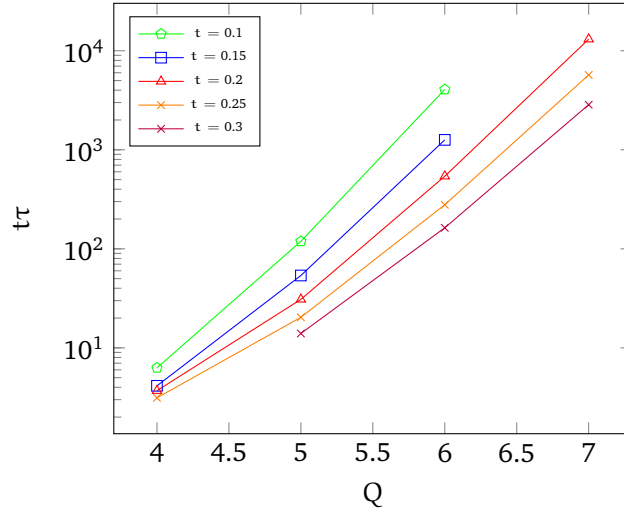


Figure 4.8: Plot of τ (in logarithmic scale) needed to obtain $|\langle Qx, Q(1-x) | e^{-iH\tau} | Q(1-x), Qx \rangle|^2 = 0.6$ with $x = 1/Q$.

$x = 1/Q$, let us express $\log \tau_{sc}$ with explicit Q dependence (for large Q):

$$\begin{aligned}
 \log \tau_{sc} &= 2Q|2x - 1| \log(Q(2x - 1)^2) + \mathcal{O}(Q) = \\
 &= (2Q - 4) \log Q + 2(2Q - 4) \log\left(1 - \frac{2}{Q}\right) + \mathcal{O}(Q) = \\
 &= (2Q - 4) \log Q + 2(2Q - 4) \left(-\frac{2}{Q} + \mathcal{O}\left(\frac{1}{Q^2}\right)\right) + \mathcal{O}(Q) = \\
 &= (2Q - 4) \log Q + \mathcal{O}(Q)
 \end{aligned} \tag{4.52}$$

Therefore we fit the results reported in Fig. (4.8) with:

$$\log \tau = a(2Q - 4) \log Q + bQ + c \tag{4.53}$$

since, from Eq. (4.52), we expect that the leading contribution has such a dependence. In particular, we should find $a \simeq 1$. In the following Table (4.1) we show the results of the fits for different values of t .

t	Fit
0.1	$3.75 - 1.35 Q + 1.04 (2Q - 4) \log(Q)$
0.15	$4.39 - 1.71 Q + 1.04 (2Q - 4) \log(Q)$
0.2	$5.68 - 2.16 Q + 1.05 (2Q - 4) \log(Q)$
0.25	$7.24 - 2.75 Q + 1.13 (2Q - 4) \log(Q)$
0.3	$3.97 - 1.77 Q + 0.90 (2Q - 4) \log(Q)$

Table 4.1: Fit of $\log \tau = a(2Q - 4) \log Q + bQ + c$ for different values of t

Form the results of the fits we find that the coefficient a is given by:

$$a = 1.03 \pm 0.08 \quad (4.54)$$

that is compatible with the value given by the semiclassical method, that is:

$$a_{\text{semiclassical}} = 1 \quad (4.55)$$

Therefore the leading contribution given by the semiclassical approximation correctly describes the quantum tunnelling phenomenon.

4.4.2 Inference of the Q and t dependence of τ/τ_{sc}

In the previous paragraph we have determined the leading contribution to the tunnelling time, and we have confirmed that it coincides, at leading order, with τ_{sc} , i.e. the tunnelling time calculated within the semi-classical method. Now we want to find the corrections to the semi-classical tunnelling time: these are found showing the dependence on Q and t of the ratio between the real tunnelling time τ (of the numerical simulations) with the semi-classical one τ_{sc} . The results are plotted in Fig. (4.9) and Fig. (4.10).

From Fig. (4.10) it is clear that there is an underlying law describing how τ/τ_{sc} depends on Q and t . In particular, since the y-axis is plotted in logarithmic scale, the Q -dependence is expected to be exponential. Notice that this behaviour is sub-leading with respect to the $Q \log(Q)$ dependence present both in τ and τ_{sc} (see Sec. (4.4.1)), which cancels considering the ratio τ/τ_{sc} . From Fig. (4.9) and Fig. (4.10) we can easily guess that the dependence of τ/τ_{sc} on

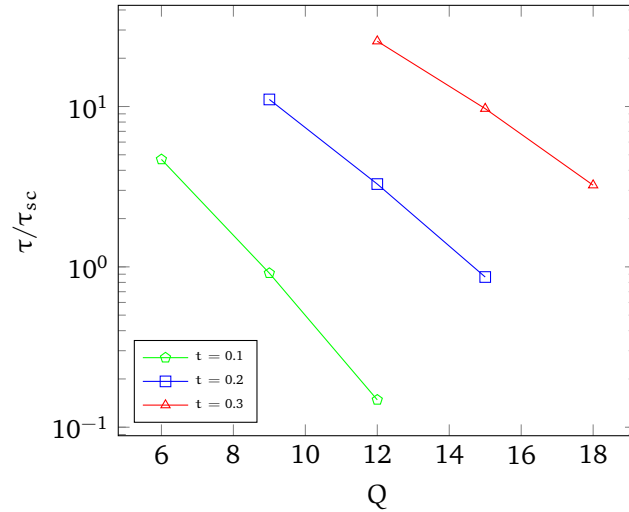


Figure 4.9: Plot of the product τ/τ_{sc} as a function of Q , with initial condition $(Q/3, 2Q/3)$, that is, $\chi = 1/3$. τ/τ_{sc} clearly depends both on Q and t , and the dependence appears to be exponential; this means it is subleading with respect to the Q^{-Q} leading dependence of τ_{sc} .

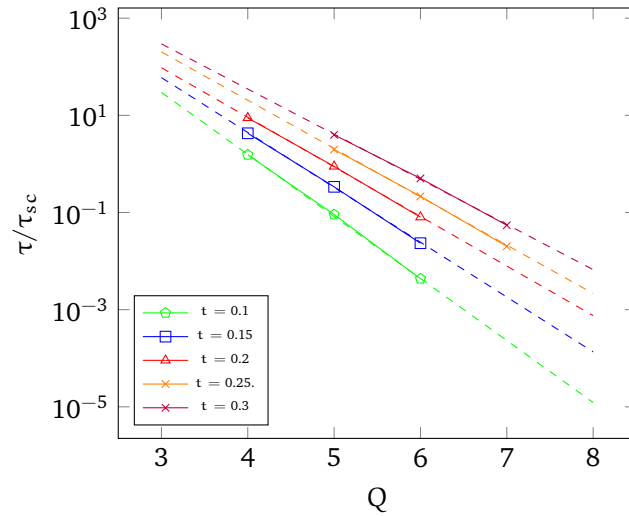


Figure 4.10: Plot of the product τ/τ_{sc} as a function of Q . In this plot we used $(1, Q - 1)$ as initial condition, that is, $\chi = 1/Q$. The dashed lines are the fits of Eq. (4.56). Notice that $\frac{\tau}{\tau_{sc}}$ is exponential in Q , which means that it is subleading with respect to the factorial dependence Q^{-Q} of τ_{sc} . Therefore, τ and τ_{sc} have the same leading contribution.

Q is linear; therefore we can do a fit with a linear law and we find:

$$\log\left(\frac{\tau}{\tau_{sc}}\right) \simeq a + b \cdot Q \quad (4.56)$$

t	a	b
0.1	12.21	-2.94
0.15	11.89	-2.60
0.2	11.61	-2.35
0.25	12.18	-2.29
0.3	12.11	-2.14

Table 4.2: Fit values of Eq. (4.56)

If we now exponentiate both sides of Eq. (4.56) we obtain a law of the form:

$$\frac{\tau}{\tau_{sc}} \propto e^{-f(t)Q} \quad (4.57)$$

where the proportionality between the two sides is given by the exponential of the coefficient a , while the coefficient b is replaced by a function of t , i.e. $f(t)$, to account for the residual dependence due to the hopping strength. A fit with the values presented in Eq. (4.56) and Table (4.2) gives, for $t < 1$:

$$f(t) \simeq 2.09 + \frac{0.09}{t} \quad (4.58)$$

Finally we find a law of the form:

$$\frac{\tau}{\tau_{sc}} \propto e^{-2Q - \frac{Q}{10t}} \quad (4.59)$$

for small values of t .

In conclusion, in this Chapter we have addressed the quantum version of the Discrete Non-Linear Schrödinger Equation, focusing, in particular, on quantum tunnelling. We found that quantum effects reduce the localization phenomenon, as particles can move in phase space even if it is not geometrically connected. Moreover, even when phase space is geometrically connected, so there are classical trajectories connecting different pieces of phase space, quantum effects

with its classically forbidden trajectories reduces the effect of entropic barrier, weakening localization.

5 | A stochastic model for the DNLSE

In the previous Chapters we have studied the DNLSE both in its classical and quantum regimes. The numerical simulations performed in order to validate the analytic results obtained have been done, so far, solving the full equations of motion of the model. This has been done using symplectic integrators in *Mathematica*, which are able to give a very precise numerical solution to the equations of motion, but this is only feasible for small times and small sizes of the lattice, at least on a standard computer.

Taking advantage of the geometric construction presented in Section (3.4) and the tunnelling probabilities calculated in the previous Chapter (4), we now introduce a simplified dynamical model for the DNLSE, both in the classical and quantum regimes. This model, instead of using the full hamiltonian evolution, uses a random sequential update rule, that in the following we will denote as “stochastic evolution”. This type of update rule has already been used, for example in [24] for studying similar classical models of mass transport. The advantage of this approach is that the numerical simulations based on random moves (e.g. Monte-Carlo steps) are much faster than numerical solvers for differential equations. Since this new model still has to reproduce the DNLSE phenomenology, the stochastic evolution has to conserve the quantities:

$$\mathcal{A} = \sum_{i=1}^N q_i \quad \mathbb{E} = \sum_{i=1}^N q_i^2 \quad (5.1)$$

In order to do this, we will focus on small number of neighbouring sites and update them according to a stochastic move that preserves the quantities in Eq. (5.1). We may then consider two adjacent sites and modify them randomly

so that:

$$q_i(t) + q_{i+1}(t) = q_i(t+1) + q_{i+1}(t+1) \quad q_i^2(t) + q_{i+1}^2(t) = q_i^2(t+1) + q_{i+1}^2(t+1) \quad (5.2)$$

However this process is trivial, since the only possible move is to exchange the values of q_i and q_{i+1} . The first non-trivial possibility is to consider three neighbouring sites and proceed so that it holds:

$$q_{i-1}(t) + q_i(t) + q_{i+1}(t) = q_{i-1}(t+1) + q_i(t+1) + q_{i+1}(t+1) \quad (5.3)$$

$$q_{i-1}^2(t) + q_i^2(t) + q_{i+1}^2(t) = q_{i-1}^2(t+1) + q_i^2(t+1) + q_{i+1}^2(t+1) \quad (5.4)$$

According to the different relative values of Eq. (5.3) and Eq. (5.4) there are two possible scenarios, displayed in Fig. (5.1a) and Fig. (5.1b).

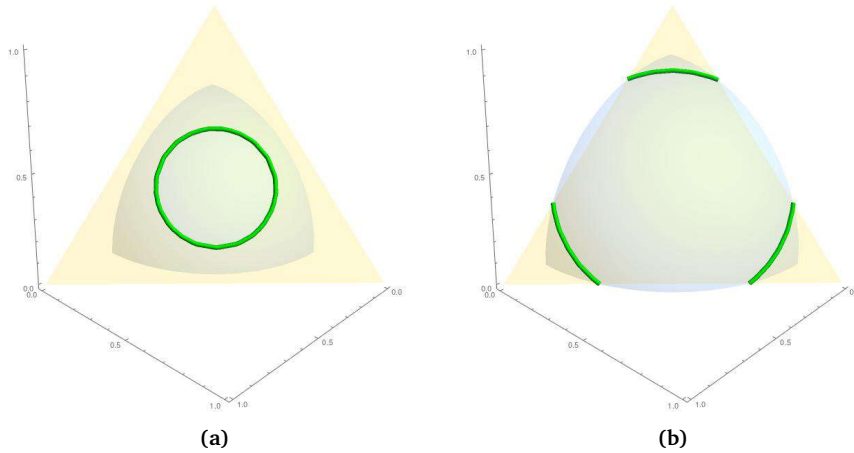


Figure 5.1: The two different scenarios that conditions Eq. (5.3) and Eq. (5.4) can generate.

The transition between the two possible cases, that is, between the circle and the three disjoint arcs, occurs when $\sum_{i=1}^3 q_i^2 = \frac{1}{2} \left(\sum_{i=1}^3 q_i \right)^2$, or equivalently, when $E = \frac{1}{2} A^2$. The stochastic update goes as follows:

- If $E \leq \frac{1}{2} A^2$ we are in the case depicted in Fig. (5.1a) and the new q_i 's are chosen at random on the circle so that conditions Eq. (5.3) and Eq. (5.4) are satisfied.
- If $E > \frac{1}{2} A^2$ we are in the case depicted in Fig. (5.1b) and the new q_i 's are chosen at random on the same arc the initial charges belonged to. This

way we still satisfy the conditions Eq. (5.3) and Eq. (5.4) and moreover we take into account the fact that the hamiltonian dynamics of the classical DNLSE does not allow to jump between disconnected arcs, since they represent disjoint sectors of phase space. This condition will be relaxed in the quantum version of the stochastic model.

In order to accomplish this goal, we introduce the quantity:

$$\vec{q}(\theta, E, \Lambda) = \frac{\Lambda}{\sqrt{3}} \vec{v}_0 + \sqrt{E - \frac{\Lambda^2}{3}} (\vec{v}_1 \cos \theta + \vec{v}_2 \sin \theta) \quad (5.5)$$

where:

$$\begin{aligned} \vec{v}_0 &= \left(\frac{1}{\sqrt{3}}, \frac{1}{\sqrt{3}}, \frac{1}{\sqrt{3}} \right) \\ \vec{v}_1 &= \left(-\frac{1}{\sqrt{6}}, -\frac{1}{\sqrt{6}}, \frac{2}{\sqrt{6}} \right) \\ \vec{v}_2 &= \left(\frac{1}{\sqrt{2}}, -\frac{1}{\sqrt{2}}, 0 \right) \end{aligned} \quad (5.6)$$

The vector \vec{v}_0 identifies the centre of the triangle in Fig. (5.1a) and Fig. (5.1b), while \vec{v}_1 and \vec{v}_2 are two orthonormal vectors that belong to the triangle. The combination Eq. (5.5) allows us to describe any point on the triangle, being θ the angle with respect to the upper vertex counted counter-clockwise.

The initial condition is extracted using the procedure described in Appendix (F), that is, generating N exponentially distributed random variables normalized so that the sum is fixed to the desired value. Moreover, one of the random variables can be setted by hand so that it reproduces the presence of a breather in the initial state.

In the numerical simulations performed we will initialize the value of the charges as follows:

$$q_i(0) = \begin{cases} e^{y_i} & \text{if } i = 1, \dots, N-1 \\ Q_B & \text{if } i = N \end{cases} \quad (5.7)$$

where y_i are random variables extracted with flat distribution in $[-3, 0]$ and Q_B is setted by hand and represents the size of the breather introduced in the initial conditions. Then the $q_i(0)$ are normalized so that their sum is fixed to:

$$\sum_{i=1}^N q_i(0) = Q \quad (5.8)$$

The simulations are performed varying the size of the initial breather, i.e. the value of Q_B ; as Q_B grows, the value of $e/2a^2$ also grows.

5.1 Classical stochastic model results

In this paragraph we report the results of the numerical simulations performed using the algorithm presented in the previous section. We are interested in determining how the system evolves depending on the initial condition and in particular on the size of the breather. An interesting quantity to determine is the correlation function, defined as:

$$\begin{aligned} \mathcal{C}^{(i)}(\tau) &= \langle q_i(t+\tau)q_i(t) \rangle - \langle q_i(t+\tau) \rangle \langle q_i(t) \rangle = \\ &= \frac{1}{T-\tau} \int_0^{T-\tau} dt q_i(t)q_i(t+\tau) - \frac{1}{(T-\tau)^2} \int_0^{T-\tau} dt q_i(t) \int_0^{T-\tau} dt' q_i(t'+\tau) \end{aligned} \quad (5.9)$$

and then averaged over all sites:

$$\mathcal{C}(\tau) = \frac{1}{N} \sum_{i=1}^N \mathcal{C}^{(i)}(\tau) \quad (5.10)$$

It will be interesting to determine whether the correlation functions have a power-law or an exponential decay. Therefore, we will fit them using a fitting function with both power-law and exponential contributions, that is:

$$\mathcal{C}(\tau) \propto \tau^{-\theta} e^{-\gamma\tau} \quad (5.11)$$

Moreover, an overlap between these two behaviours may be a relevant sign for a transition from localized to non-localized phases. This is qualitatively justified by the fact that, in a non-localized phase, the correlation function is expected to have an exponential decay. In the presence of a localized phase, however, the correlation function is expected to have a weaker decay because of the presence of the breather-like excitation. The correlation functions $\mathcal{C}(\tau)$ obtained with the numerical simulations are plotted in Fig. (5.2) and Fig. (5.3).

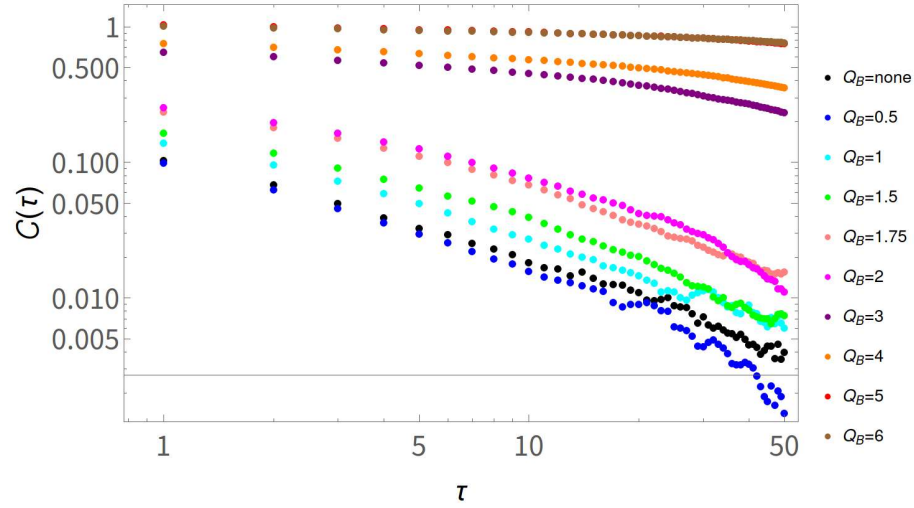


Figure 5.2: Correlation function $\mathcal{C}(\tau)$ for different sizes of the breather with $N = 32$, $Q = 20$ ($\hbar = 0$).

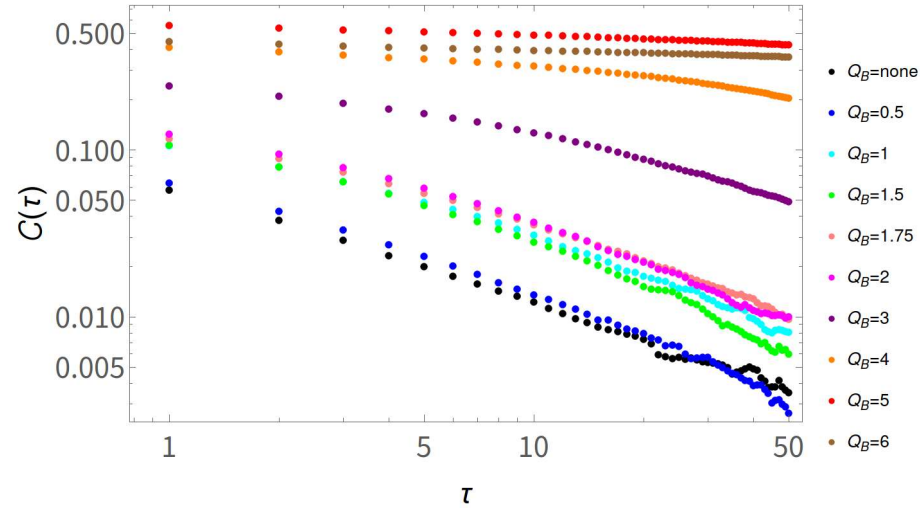


Figure 5.3: Correlation function $\mathcal{C}(\tau)$ for different sizes of the breather with $N = 64$, $Q = 30$ ($\hbar = 0$).

For illustrative purpose, we present the result obtained when:

1. we have different runs of the numerical simulation keeping fixed the values of Q , N and Q_B . The results are reported in Fig. (5.4);

2. we use the same initial condition, i.e., the $q_i(0)$ are the same for all the simulations. The differences in the correlation functions are due to the stochastic part of the algorithm. In Fig. (5.5) we report the results.

The difference between these two cases is that, in case (1.), the value of $e/2a^2$ changes between two different runs of the simulation while in case (2.) the value of $e/2a^2$ is always the same having the same initial conditions.

For the case (1.) we performed ten runs and the mean value of $e/2a^2$ registered

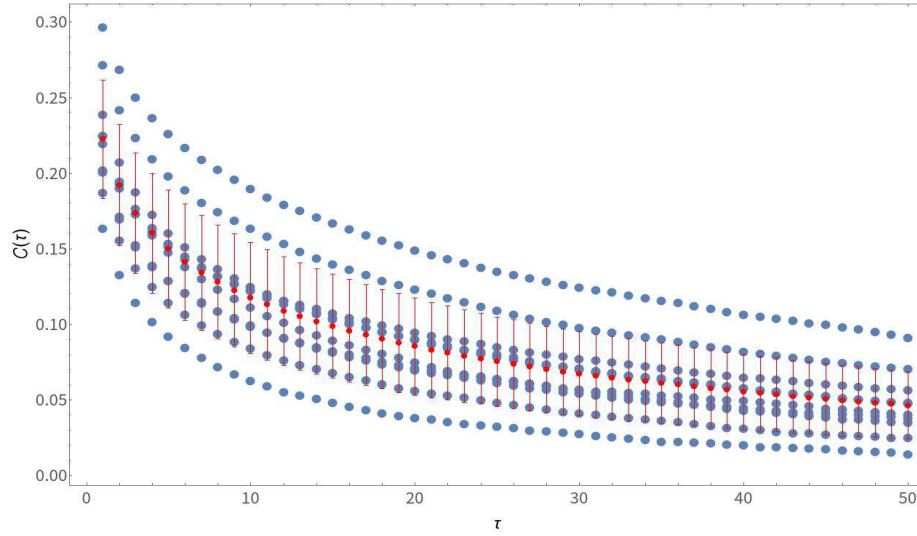


Figure 5.4: Correlation function $\mathcal{C}(\tau)$ obtained setting $Q = 30$, $N = 64$ and $Q_B = 3$ ($\hbar = 0$). The correlation functions obtained at each run are represented in blue, while the mean value of $\mathcal{C}(\tau)$ with the relative standard deviation is represented in red.

is:

$$\left(\frac{e}{2a^2}\right)_1 = 1.21 \pm 0.10 \quad (5.12)$$

For the case (2.) we have

$$\left(\frac{e}{2a^2}\right)_2 = 1.32 \quad (5.13)$$

and in Fig. (5.5) we plot also the fitting line for the mean correlation function, that has the expression:

$$\log \bar{\mathcal{C}}(\tau)_{\text{fit}, 50} = (0.11 \pm 0.06) - (0.00245 \pm 0.00006)\tau - (0.617 \pm 0.014) \log(\tau) \quad (5.14)$$

The correlation function has been fitted with a weighted fit in the interval $\tau \in$

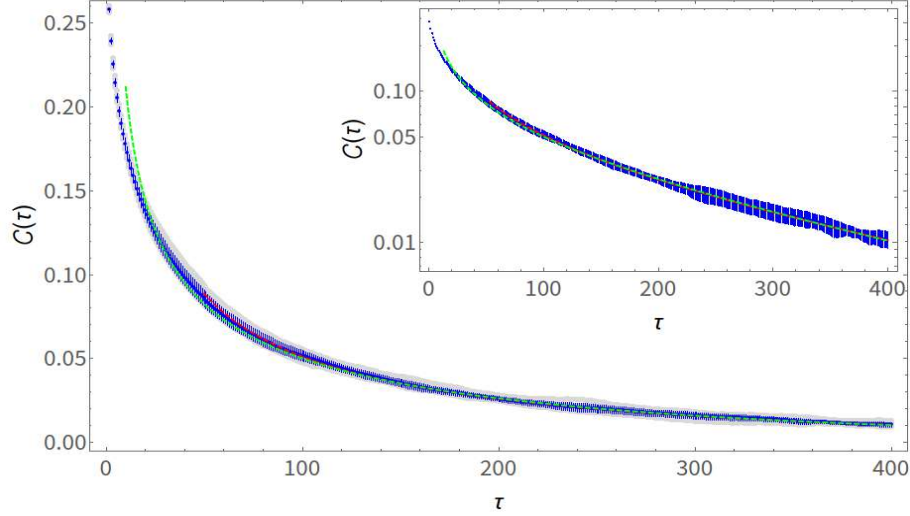


Figure 5.5: Correlation function $\mathcal{C}(\tau)$ obtained setting $Q = 30$, $N = 64$ ($\hbar = 0$) and fixing the initial condition. The correlation functions obtained at each run are represented in grey, while the mean value of $\mathcal{C}(\tau)$ with the relative standard deviation is represented in blue. The red and green dashed line are the fit curves for the mean correlation function (see Eq. (5.14) and Eq. (5.15) respectively). In the inset we represent the correlation function in a log-linear plot, where the exponential decay for large τ is evident.

$[50, 400]$, in order to avoid the transient part for small values of τ . If we fit the same correlation function, but $\tau \in [10, 400]$, we get:

$$\log \bar{\mathcal{C}}(\tau)_{\text{fit}, 10} = -(0.34 \pm 0.02) - (0.00289 \pm 0.00005)\tau - (0.513 \pm 0.009) \log(\tau) \quad (5.15)$$

For both $\log \bar{\mathcal{C}}(\tau)_{\text{fit}, 50}$ and $\log \bar{\mathcal{C}}(\tau)_{\text{fit}, 10}$ we indicated the 95% confidence intervals. Notice that for large values of τ the exponential contribution becomes always more relevant: from the fit we can extrapolate that it will be the leading contribution for $\tau \simeq 1200$.

Therefore, from this paragraph we can conclude that the greater is the value of Q_B the slower is the decay of the correlation function. Moreover, the correlation function has a power-law decay for small values of τ and exponential for large values of τ ; as we already mentioned, this reflects the decay of the breather-like excitation present in the initial condition.

5.2 Quantum stochastic model results

In this section we report the results obtained with a modified version of the stochastic model introduced in the previous section. In particular, in order to account for the quantum nature of the system we want to simulate, we added a random move on the triplet of Eq. (5.3) and Eq. (5.4). It consists of a random permutation of the values of the q 's that happens with probability proportional to $\exp[-\mathcal{A} \log \mathcal{A}]$, with $\mathcal{A} = \sum_{i=1}^3 q_i$. This choice is done having in mind the Q dependence of the reflection coefficient (and tunnelling time) that we performed in Sec. (4.3). Also in this case, we evaluated the correlation function $\mathcal{C}(\tau)$ defined in Eq. (5.10)

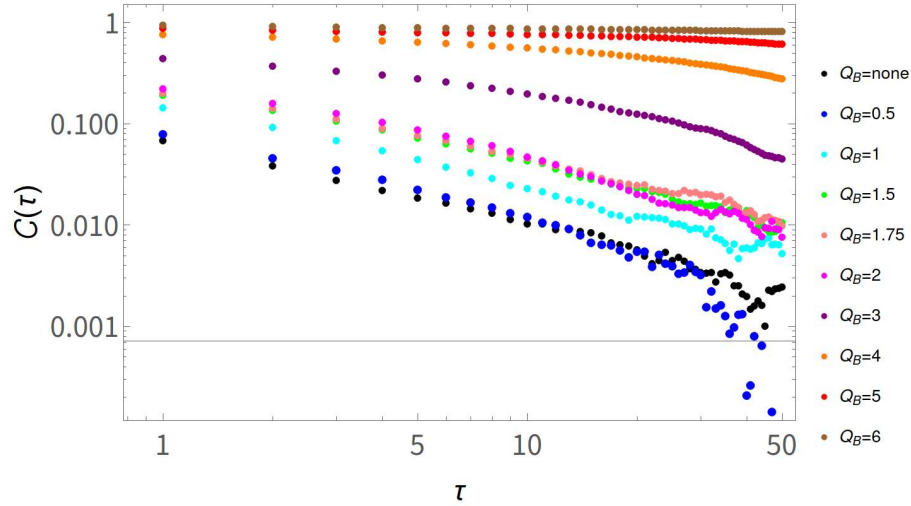


Figure 5.6: Correlation function $\mathcal{C}(\tau)$ for the quantum stochastic model for different sizes of the breather with $N = 32$, $Q = 20$ and $\hbar = 1$.

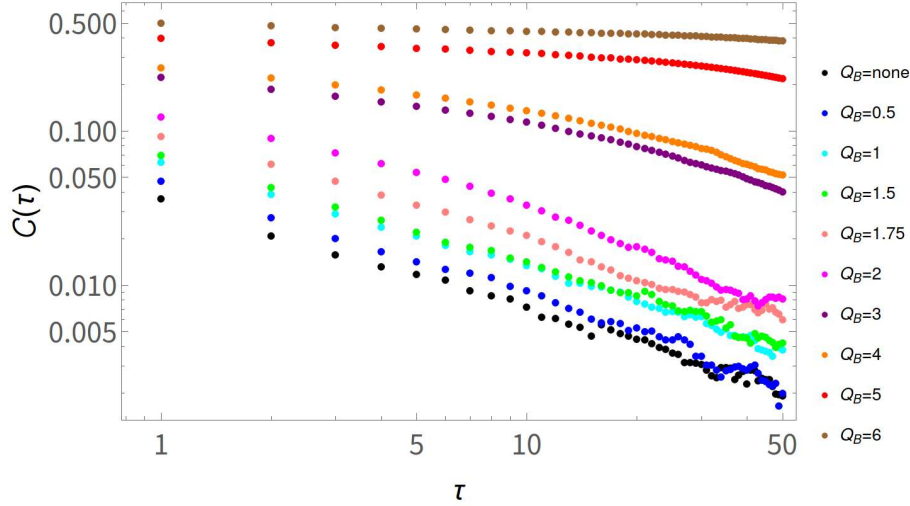


Figure 5.7: Correlation function $\mathcal{C}(\tau)$ for the quantum stochastic model for different sizes of the breather with $N = 64$, $Q = 30$ and $\hbar = 1$.

5.2.1 Varying \hbar

We present here the result obtained by introducing a new parameter λ in the probability for tunnelling in the quantum stochastic model, i.e., with probability equal to $p(\lambda) = e^{-\lambda \mathcal{A} \log \mathcal{A}}$ and by varying it. This is equivalent to vary the value of \hbar , that enters in the semiclassical probability as $p = e^{-\frac{1}{\hbar} \mathcal{A} \log \mathcal{A}}$. In Fig. (5.11) and Fig. (5.12) we report the results for $\lambda = 0.1$, that generates a higher probability of tunnelling with respect to $\lambda = 1$. We can also focus on a particular case ($Q = 30$, $N = 64$) as we did for the classical version and we study in detail the correlation function for different values of \hbar , which is equivalent to change the tunnelling probability in our model. The results are plotted in Fig. (5.8).

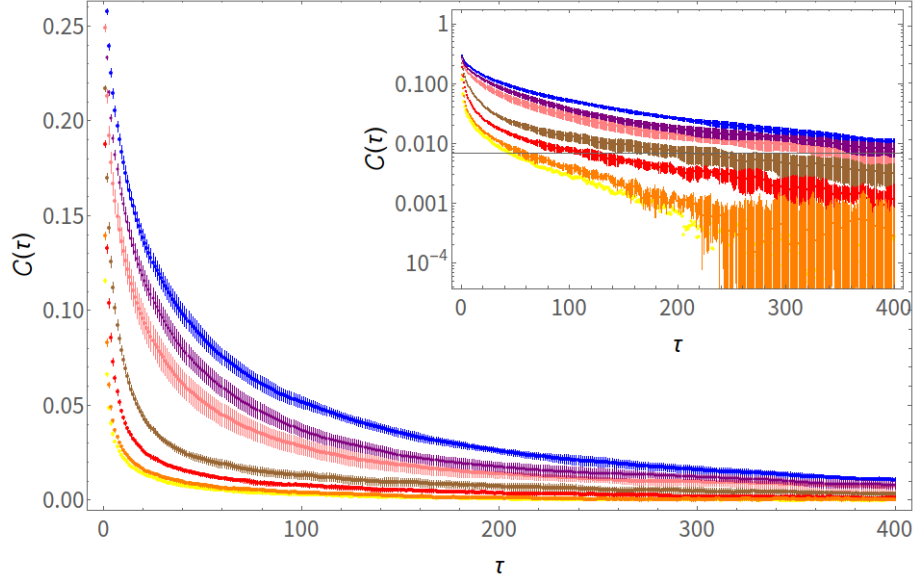


Figure 5.8: Correlation function $\mathcal{C}(\tau)$ obtained setting $Q = 30$, $N = 64$ and fixing the initial condition for different values of \hbar . For each value of \hbar we did six runs and we represent here the mean value of $\mathcal{C}(\tau)$ with the relative standard deviation. Yellow $\rightarrow \hbar = 10$, Orange $\rightarrow \hbar = 6$, Red $\rightarrow \hbar = 3$, Brown $\rightarrow \hbar = 2$, Pink $\rightarrow \hbar = 1$, Purple $\rightarrow \hbar = 0.5$, Blue $\rightarrow \hbar = 0$ (classical model). In the inset we represent the correlation function in a log-linear plot, where the exponential decay for large τ is evident.

The fits for the different values of \hbar are given by:

$$\log \bar{\mathcal{C}}(\tau)_{\text{fit}} = \kappa - \gamma\tau - \theta \log(\tau) \quad (5.16)$$

\hbar	κ	γ	θ
10	$-(2.6 \pm 1.2)$	0.012 ± 0.002	0.4 ± 0.3
6	$-(1.1 \pm 0.5)$	0.0052 ± 0.0008	0.88 ± 0.12
3	$-(2.08 \pm 0.12)$	0.0042 ± 0.0002	0.51 ± 0.03
2	$-(1.16 \pm 0.05)$	0.00159 ± 0.00009	0.656 ± 0.013
1	0.37 ± 0.09	0.00049 ± 0.00011	0.86 ± 0.02
0.5	$-(0.02 \pm 0.09)$	0.00178 ± 0.00013	0.68 ± 0.02
0	$-(0.34 \pm 0.02)$	0.00289 ± 0.00005	0.513 ± 0.009

Table 5.1: Fit coefficients for Eq. (5.16)

These fits have been done for $\tau \in [10, 400]$ and 95% confidence intervals.

Referring to Eq. (5.11) we show in Fig. (5.9) and Fig. (5.10) the dependence of γ and θ on \hbar for the fits of Eq. (5.16) and Table (5.1).

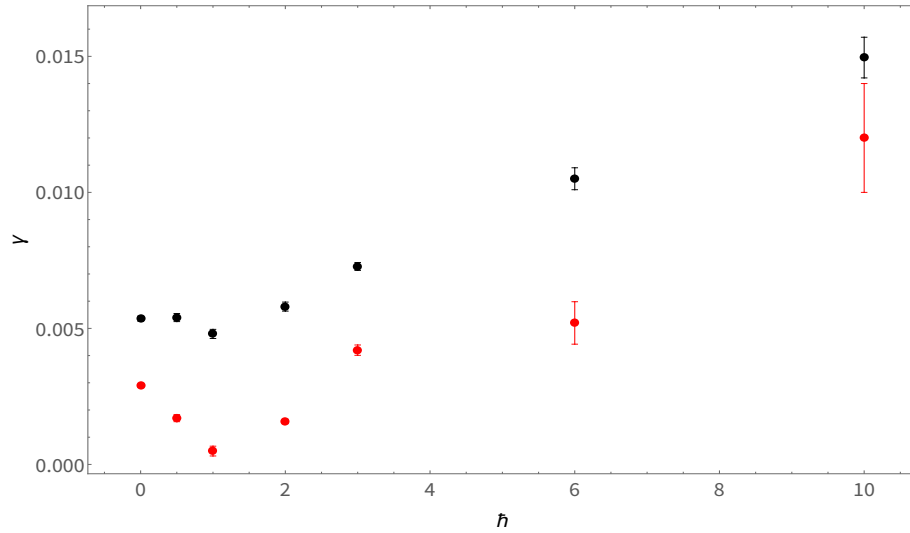


Figure 5.9: γ dependence on \hbar obtained for Eq. (5.16) (in red). The error bars are given by the fits with 95% confidence intervals. In black we plot the value of γ obtained if the fit in Eq. (5.16) is done without the parameter θ .

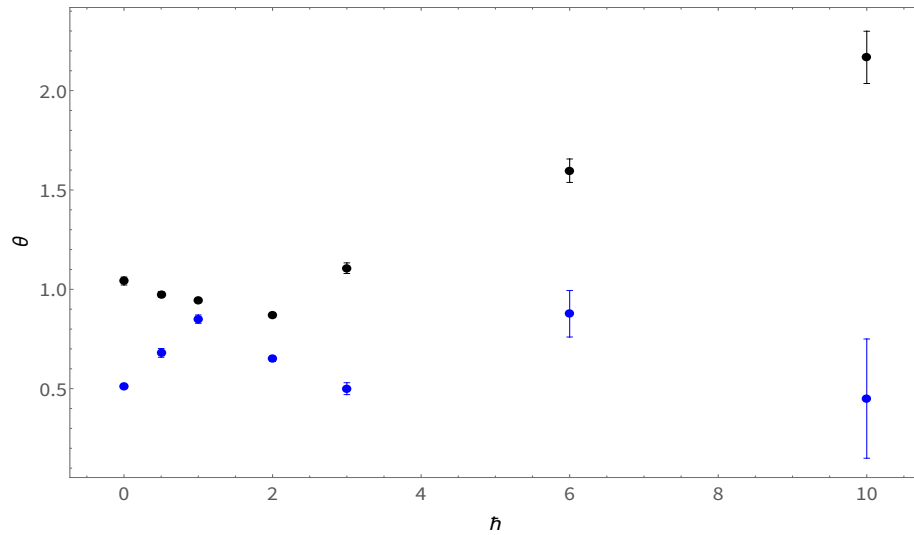


Figure 5.10: θ dependence on \hbar obtained for Eq. (5.16). The error bars are given by the fits with 95% confidence intervals. In black we plot the value of θ obtained if the fit in Eq. (5.16) is done without the parameter γ .

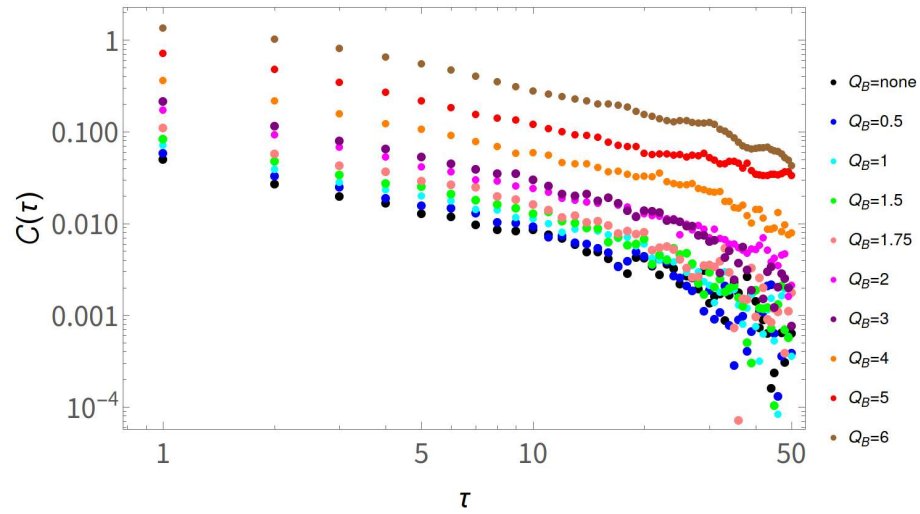


Figure 5.11: Correlation function $\mathcal{C}(\tau)$ for the quantum stochastic model for different sizes of the breather with $N = 32$, $Q = 20$ and $\hbar = 10$.

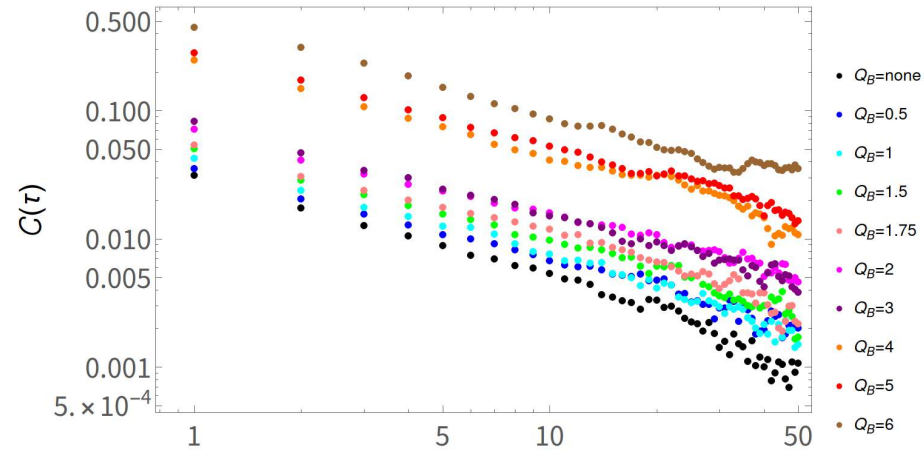


Figure 5.12: Correlation function $\mathcal{C}(\tau)$ for the quantum stochastic model for different sizes of the breather with $N = 64$, $Q = 30$ and $\hbar = 10$.

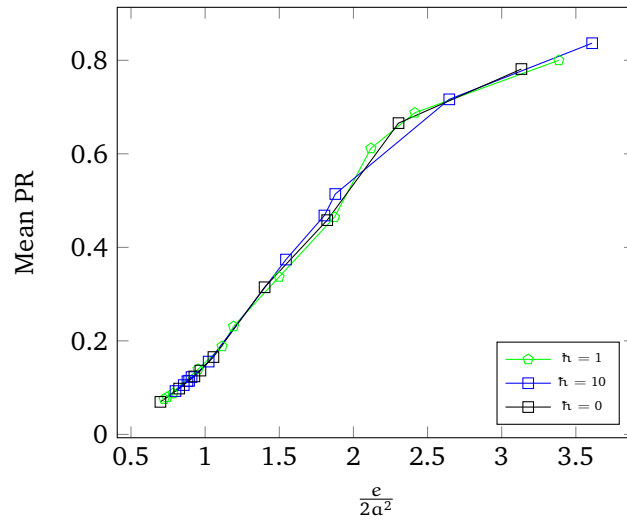


Figure 5.13: Plot of the behaviour of the mean value of the PR Y_2^{-1} as a function of $\frac{e}{2a^2}$ for different values of h for $Q = 20$, $L = 32$. The mean PR is obtained for a number of steps equal to $N_{\text{steps}} = 5L \cdot 10^3$.

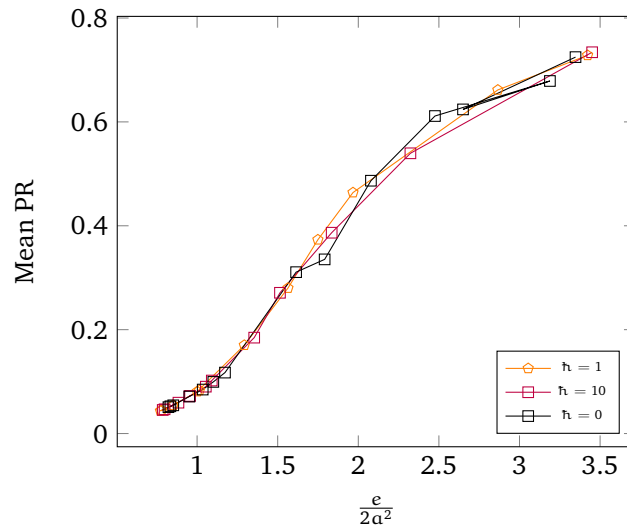


Figure 5.14: Plot of the behaviour of the mean value of the PR Y_2^{-1} as a function of $\frac{e}{2a^2}$ for different values of h for $Q = 30$, $L = 64$. The mean PR is obtained for a number of steps equal to $N_{\text{steps}} = L \cdot 10^4$.

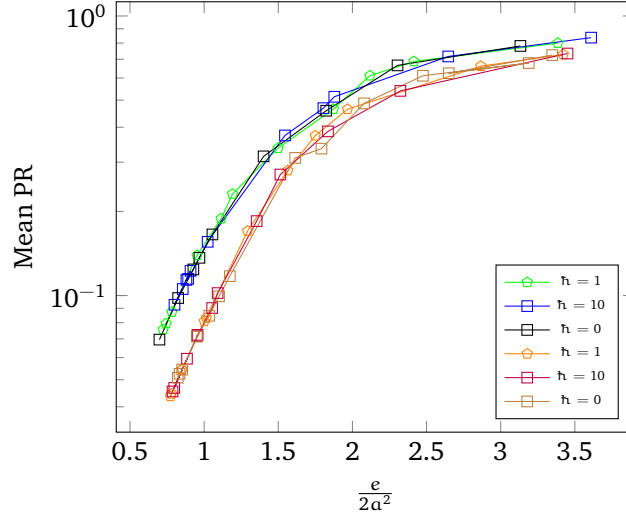


Figure 5.15: Plot of the behaviour of the mean value of the PR Y_2^{-1} as a function of $\frac{e}{2a^2}$ for different values of \hbar for $Q = 20$, $L = 32$ (in blue, green and black) and for $Q = 30$, $L = 64$ (in purple, orange and brown)

From this preliminary investigation it seems clear that, by increasing the tunnelling probability, the breather can move more easily on the lattice: this can be seen by comparing the correlation functions and observing that for $\hbar = 10$ it decays much faster than when $\hbar = 1$. However the size of the breather does not change significantly varying \hbar , since from Fig. (5.13), Fig. (5.14) and Fig. (5.15) we see that the dependence of the mean value of the Participation Ratio (PR) as a function of $e/2a^2$ is not affected significantly by the value of \hbar . This means that the breather moves along the lattice as the systems evolves in time, without changing its size.

5.3 Universality

In this section we would like to better investigate the behaviour of the correlations functions: in particular we are interested in the crossover between the power-law and the exponential decay that we found in the previous sections. In order to point out the connection between these two regimes, we would like to find an appropriate universal law:

$$\mathcal{C}(\tau) = A(Q_B) f\left(\frac{\tau}{\tau(Q_B)}\right) \quad (5.17)$$

that describes, for different values of Q_B , the correlation functions found previously. In particular, we are interested in the finding appropriate $A(Q_B)$ and $\tau(Q_B)$ such that all the correlation functions collapse in a unique curve. The first, natural step is to rescale $\mathcal{C}(\tau)$ so that all the curves have the same starting point, so we will plot $\mathcal{C}(\tau)/\mathcal{C}(0)$. Then we choose proper values of $\tau(Q_B)$ to obtain our purpose. We show the results in Fig. (5.16), Fig. (5.17), Fig. (5.18). We have, therefore, found the appropriate values of $\tau(Q_B)$ for different values

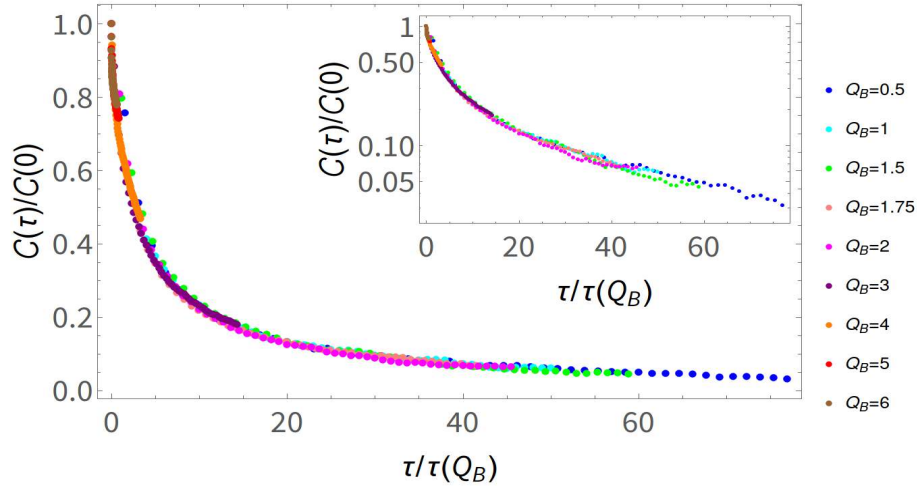


Figure 5.16: Rescaled correlation function for the classical stochastic model with $N = 64$, $Q = 30$ ($\hbar = 0$).

of Q_B so that, keeping the correlation function for $Q_B = 0$ as reference, all the others collapse on it. We can perform a fit of the universal correlation function obtained for the different values of \hbar .

In Fig. (5.19) we show the values of $\tau(Q_B)$ used to obtain the appropriate rescaling in Fig. (5.16), Fig. (5.17) and Fig. (5.18). Notice that the values of $\tau(Q_B)$ decrease as \hbar increases (see below for details): in particular, for $\hbar = 10$, $\tau(Q_B)$ is almost independent of Q_B reflecting the fact that, having a high tunnelling probability, the correlation function is insensible to the size of the breather, at least for values of Q_B smaller than $Q_B \sim 10$.

For completeness, let us fit the universal correlation functions we have just found for different values of \hbar : we use the same fit form of Eq. (5.16). The coefficients of the fitting functions are shown in Table (5.2). Notice that the coefficients presented in Table (5.2) seem to be in contradiction with the predicted behaviour of γ and θ as \hbar varies: however, remember that the correlation func-

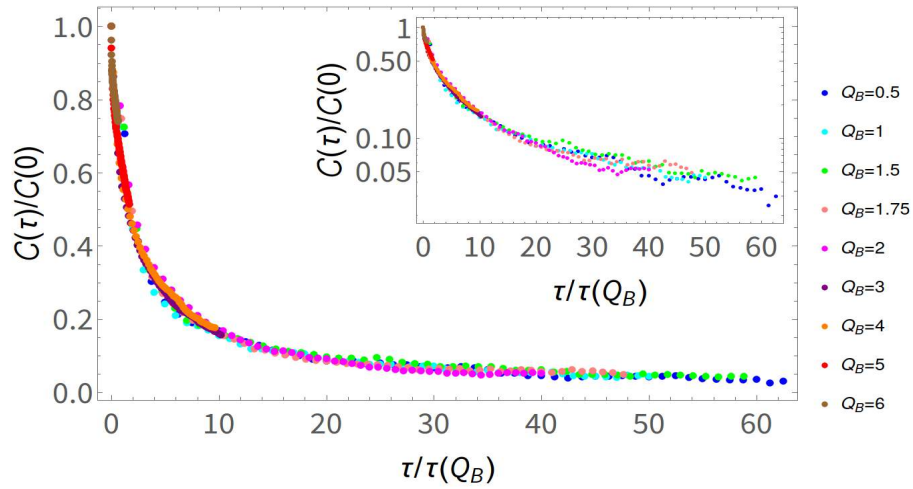


Figure 5.17: Rescaled correlation function for the quantum stochastic model with $N = 64$, $Q = 30$ and $\hbar = 1$.

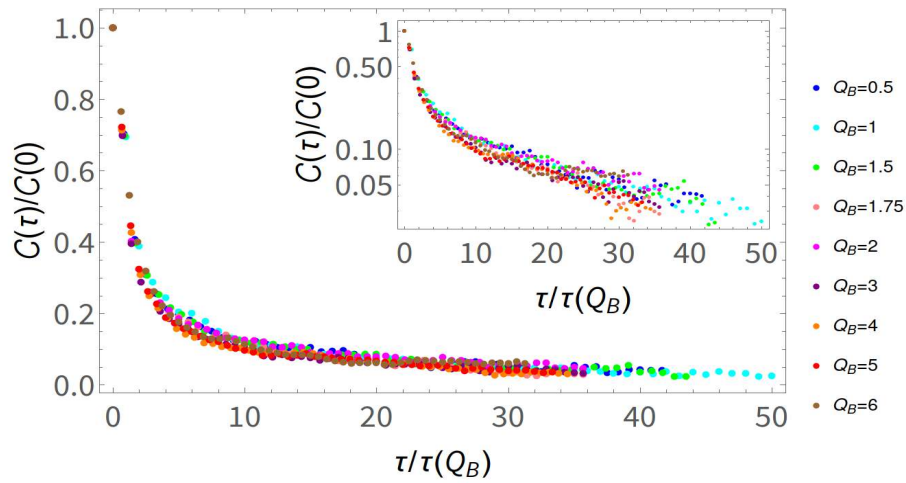


Figure 5.18: Rescaled correlation function for the quantum stochastic model with $N = 64$, $Q = 30$ and $\hbar = 10$.

tions that we are fitting are rescaled, both on the y - and the x -axis; therefore the relation between the coefficients does not reflect the one we had already found.

Now we can do the same also for the correlation functions obtained at fixed

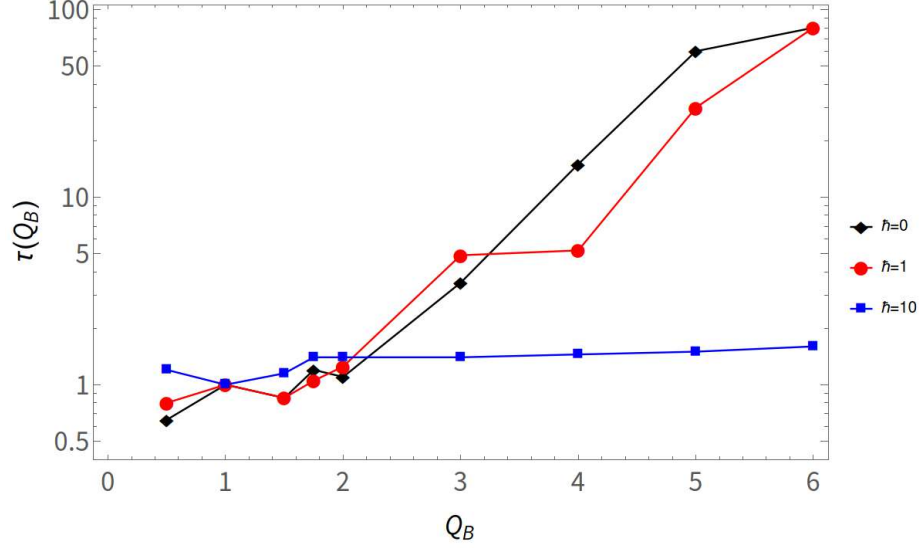


Figure 5.19: Values of $\tau(Q_B)$ used to obtain the rescaling of the correlation functions in Fig. (5.16), Fig. (5.17), Fig. (5.18).

\hbar	κ	γ	θ
0	-0.52	0.027	0.27
1	-0.66	0.024	0.36
10	-0.60	0.0094	0.64

Table 5.2: Fit coefficients for the correlation functions of Fig. (5.16), Fig. (5.17), Fig. (5.18): the form of the fitting function is given by Eq. (5.16)

initial condition and varying \hbar , so that we can extract the dependence of τ on the strength of the quantum effects. To do so, we take as reference Fig. (5.8), that was obtained by fixing the initial condition with $Q_B = 3$ and varying \hbar . If we operate a proper rescaling on the x -axis we get Fig. (5.20). Notice that in Fig. (5.20) we have not rescaled $\mathcal{C}(\tau)$ since all the curves have the same initial condition. As we did previously, we now show in Fig. (5.21) the values of $\tau(\hbar)$ used to obtain the rescaling in Fig. (5.20).

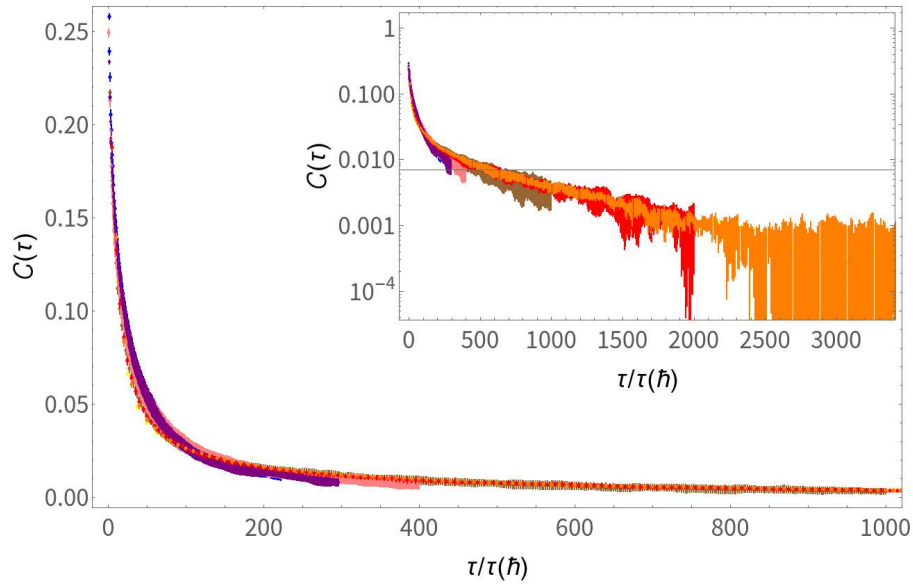


Figure 5.20: Rescaled correlation function for fixed initial condition and different values of \hbar ; Yellow $\rightarrow \hbar = 10$, Orange $\rightarrow \hbar = 6$, Red $\rightarrow \hbar = 3$, Brown $\rightarrow \hbar = 2$, Pink $\rightarrow \hbar = 1$, Purple $\rightarrow \hbar = 0.5$, Blue $\rightarrow \hbar = 0$ (classical model).

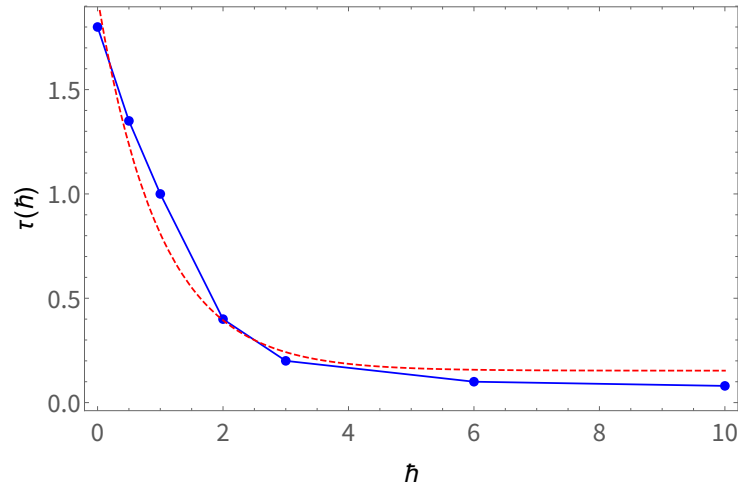


Figure 5.21: Dependence of $\tau(\hbar)$ on \hbar . The dashed red line is the fit given by Eq. (5.18)

For completeness, we also present a fit for the points in Fig. (5.21); it turns

out that an exponential function is a good fitting line and we get:

$$\tau(\hbar) = 0.15 + 1.8 e^{-\hbar} \quad (5.18)$$

5.3.1 Interpretation of the results

In the previous section we found that, after a proper rescaling, the correlation functions collapse on a unique curve. The rescaling is done by normalizing $\mathcal{C}(\tau)$ with its value for $\tau = 0$, that is $\mathcal{C}(\tau)/\mathcal{C}(0)$. Then we have rescaled τ , dividing it by a proper function $\tau(Q_B, \hbar)$, which is proportional to the time after which the correlation functions are dominated by an exponential decay and no more by a power law decay. In other words, $\tau(Q_B, \hbar)$ is proportional to the time for which the breather-like excitation is stable; for larger times the correlation function has an exponential decay, which means that the excitation is no more stable and localization is lost. The interesting feature we found is that $\tau(Q_B, \hbar)$ depends on Q_B and \hbar as we have shown in Fig. (5.19) and Fig. (5.21). In particular, from Fig. (5.19) we see that, for $Q_B \gtrsim 2$ (that is, for Q_B a few time bigger than the typical size of the charges $\sim Q/N \simeq 1/2$ in our case) $\tau(Q_B, \hbar)$ is a monotonic increasing function of Q_B for fixed \hbar . From Fig. (5.19) we may also expect that, for fixed Q_B , $\tau(Q_B, \hbar)$ is a decreasing function of \hbar ; this is investigated in Fig. (5.21), where we can clearly see that $\tau(Q_B, \hbar)$ is a monotonic decreasing function of \hbar for fixed Q_B .

These behaviours of $\tau(Q_B, \hbar)$ have a physical interpretation; the dependence on Q_B is clear: for larger values of the size of the breather-like excitation in the initial configuration, the ratio $e/2a^2$ gets bigger and the system moves toward a non-Gibbs state (negative temperature state). Consequently, the excitation is more stable and much more off-resonance with its neighbouring charges, and thus the characteristic time of decay increases (ergodization time).

The dependence on \hbar , instead, reflects the fact that, in the quantum regime, thanks to the tunnelling effect, the breather-like excitation can move more freely than in the classical regime. This means that there is a higher probability that the excitation is resonant with its neighbours and thus it becomes unstable in a smaller characteristic time with respect to the classical case.

6 | Conclusions and outlooks

In this thesis work we focused on the Discrete Non-Linear Schrödinger Equation, both in its classical and quantum regimes. We also addressed the Josephson Junction Array model, described by a modified version of the DNLSE hamiltonian. In particular, we were interested in the statistical mechanical properties of such systems, since from few years it is known that they display a peculiar phase characterized by localization and, maybe, ergodicity breaking.

Recent works (see [2] for example) showed that the DNLSE presents a localized phase in the high energy regime, where the system is described by non-Gibbs states. This seemed to yield also to the breakdown of ergodicity, even if in [19] the authors give evidence for the absence of ergodicity breaking in correspondence of the non-Gibbs transition line. Moreover, the JJA model seemed to have the same phenomenology, but contradictory results were found in different works (compare [3] and [21]).

In our work we have been able to compute the partition function of the JJA model in the high energy limit, showing that there are no non-Gibbs states, as the authors in [21] numerically showed. Furthermore, we introduced a geometric picture for visualizing the variable-space of both the DNLSE and the JJA systems. Using the properties of such construction, we have been able to show that the non-Gibbs regime of the DNLES is not phase of broken ergodicity and we confirmed that the JJA does not display a localized phase.

Subsequently, we addressed the quantum version of the DNLSE, with the purpose of investigating the presence and the intensity of the localization present in the classical regime also in the quantum case. To this aim we calculated the tunnelling coefficients between different configurations of the system, showing that the tunnelling probability decreases faster than an exponential as the energy of the involved sites grows. This means that the quantum regime presents a weaker localization phenomenon compared to its classical analogue, but the

difference becomes soon negligible as the size of the more energetic sites grows. Finally, we used the knowledge gained in the study of the classical and quantum system to build a stochastic-driven algorithm to simulate the DNLSE. Instead of using the full equations of motion to study the dynamics, we introduced a random move for the evolution of the system. This algorithm has been used to study the correlation functions of the system in different regimes; they have then been properly rescaled in order to obtain a unique curve. Studying the rescaling coefficient we have been able to confirm numerically that the relaxation time of the excitations depends both on the size of the most energetic site and on the intensity of the quantum effects. In particular, as the size of the site becomes larger, also the “ergodization time” gets larger, while, for increasing values of \hbar (i.e. going deep in the quantum regime) the “ergodization time” becomes smaller, accounting for the higher mobility of the energy of each site due to tunnelling.

The results obtained in this thesis work are both analytical and numerical, and they allowed us to give a complete qualitative understanding of the high-energy phase of our models and also quantitative results have been found. For future investigations on the subject, it may be interesting to improve the numerical simulations, performing extensive investigations of the DNLSE for larger times in order to have a further confirm of our results. Moreover, also an analytic computation of the partition function of the Bose-Hubbard model could be tried, at least in some proper approximation, to confirm our qualitative understanding and gain some further quantitative properties.

7 | Acknowledgements

This thesis is the last step of my course of study at the University of Milan. I have found here many good professors and students.

I want to thank, firstly, my supervisor professor Sergio Caracciolo, who has been a constant point of reference and a source of inspiration. I am grateful to my external supervisor, professor Antonello Scardicchio, for having constantly followed the evolution of this thesis work and for the chance he gave me at the beginning of this year, when I spent a month at ICTP in Trieste. I would like to thank professors Claudio Arezzo, Rosario Fazio, Sergej Flach and Giacomo Gradenigo for fruitful discussions during this thesis work.

I will forever be deeply grateful to my family, for the complete support they gave me and for the beautiful times we have spent together so far.

I would also thank all my friends, for the moments spent together and for the closeness they always demonstrate.

A | Large Deviation Principle

We are interested in finding the probability distribution $d_N(z)$ of the variable $z := \sum_{i=1}^N x_i$ in the region where the probability of an event is very small, i.e. we are interested in large deviations from the mean. Suppose that x_i are i.i.d. random variables with probability distribution $\mathcal{P}(x_i)$. Our purpose is to determine $d_N(z)$ in the large- N limit for large values of z . To be more specific, we are interested in the probability of the event $z = \bar{z}$, where $\bar{z} = \lambda N$, for $N \rightarrow \infty$. The probability for this event will be very small, thus we expect:

$$d_N(\bar{z}) \sim e^{NS(\lambda)} \quad (\text{A.1})$$

where $S(\lambda)$ will be a decreasing function of λ . We have defined:

$$S(\lambda) \equiv \lim_{N \rightarrow \infty} \frac{\log(d_N(N\lambda))}{N} \quad (\text{A.2})$$

which is usually called "rate function". Let us determine it.

We introduce the Fourier transform of the probability distribution $d_N(z)$:

$$d_N(z) = \frac{1}{2\pi} \int dq e^{-izq} \tilde{d}_N(q) \quad (\text{A.3})$$

Since the random variables x_i are i.i.d., then:

$$\tilde{d}_N(q) = \tilde{\mathcal{P}}(q)^N = e^{N \log \tilde{\mathcal{P}}(q)} \quad (\text{A.4})$$

Consequently we get:

$$d_N(z) = \frac{1}{2\pi} \int dq e^{-izq} e^{N \log \tilde{\mathcal{P}}(q)} \quad (\text{A.5})$$

$$d_N(\bar{z}) = \frac{1}{2\pi} \int dq e^{N[\log \tilde{\mathcal{P}}(q) - i\lambda q]} \quad (\text{A.6})$$

For large N , we can solve this integral applying the saddle-point method (see Appendix (B)). In particular we have to identify the value of q for which the argument of the exponential is maximum. This is done solving the equation:

$$\frac{d \log \tilde{\mathcal{P}}(q)}{dq} = i\lambda \quad (\text{A.7})$$

We call $\bar{q}(\lambda)$ the solution of Eq. (A.7), and thus we get:

$$d_N(N\lambda) \propto e^{N[\log \tilde{\mathcal{P}}(\bar{q}) - i\lambda \bar{q}(\lambda)]} \quad (\text{A.8})$$

If the saddle-point Eq. (A.7) does not have solution, the probability distribution $d_N(z)$ goes to zero faster than an exponential or is everywhere zero.

B | Saddle Point Method

Here we give an heuristic derivation of the saddle-point method for evaluating integrals of exponential functions, being very common in statistical physics. We will focus, for simplicity, on the case of real functions. Consider the integral:

$$I(N) = \int_a^b dx f(x) e^{Ng(x)} \quad (\text{B.1})$$

where f and g are two real functions and $a < b$. If g has a peaked maximum in $x_0 \in (a, b)$, the integral is dominated by the value of the integrand at the point where the maximum is located. Suppose we can expand g in series as:

$$g(x) = g(x_0) - \frac{|g''(x_0)|}{2}(x - x_0)^2 + \mathcal{O}((x - x_0)^3) \quad (\text{B.2})$$

since we know that x_0 is a maximum point for g . Let us perform the following change of variables:

$$u := \sqrt{\frac{N|g''(x_0)|}{2}}(x - x_0) \quad (\text{B.3})$$

and thus obtaining:

$$I(N) = e^{Ng(x_0)} \int_{u_a}^{u_b} du \sqrt{\frac{2}{N|g''(x_0)|}} f\left(x_0 + u\sqrt{\frac{2}{N|g''(x_0)|}}\right) e^{-u^2 + R} \quad (\text{B.4})$$

where $R = \mathcal{O}((x - x_0)^3)$. We now take the limit $N \rightarrow \infty$, use the expansion $f(x) = f(x_0) + \epsilon f'(x_0) + \frac{f''(x_0)}{2}\epsilon^2 + \mathcal{O}(\epsilon^3)$ and perform the Gaussian integral,

obtaining:

$$\begin{aligned}
I(N) &\stackrel{N \rightarrow \infty}{\cong} e^{Ng(x_0)} \int_{-\infty}^{\infty} du \sqrt{\frac{2}{N|g''(x_0)|}} \left(f(x_0) + \right. \\
&\quad \left. + u \sqrt{\frac{2}{N|g''(x_0)|}} f'(x_0) + \frac{f''(x_0)}{2} u^2 \frac{2}{N|g''(x_0)|} + \mathcal{O}\left(u \sqrt{\frac{2}{N|g''(x_0)|}}\right)^3 \right) e^{-u^2} = \\
&= e^{Ng(x_0)} \left(\sqrt{\frac{2\pi}{N|g''(x_0)|}} f(x_0) + \frac{1}{2} f''(x_0) \sqrt{\frac{2\pi}{(N|g''(x_0)|)^3}} + \mathcal{O}(N^{(-5/2)}) \right)
\end{aligned} \tag{B.5}$$

At first order we get the familiar expression:

$$I(N) \stackrel{N \rightarrow \infty}{\cong} e^{Ng(x_0)} f(x_0) \sqrt{\frac{2\pi}{N|g''(x_0)|}} \propto e^{Ng(x_0)} f(x_0) \tag{B.6}$$

C | Condensation Phenomena from the Large Deviation Theory

In this section we are interested in showing how condensation phenomena occur in systems described by stochastic evolution: for this purpose we will focus on *Mass Transport* problems ([20], [25]) that present the same features of our problem. In particular, we will show how the condensation phenomena can be explained simply studying the sum of i.i.d. random variables.

C.1 Zero Range Process

The *Zero Range Process* (ZRP) is the simplest analytically solvable model of mass transport that exhibits a real-space condensation phenomenon in a certain range of its parameters. For simplicity, we will consider the ZRP problem on a 1D lattice with L sites; at any instant of time, each site of the lattice has a certain number of particles, say m_i at site i , where $m_i \geq 0$. A configuration of the system is completely determined by the number of particles at all sites $\{m_1, m_2, \dots, m_L\}$. Suppose that, at the beginning, the total number of particles is $M = \sum_{i=1}^L m_i$ and that the subsequent dynamics will preserve the total number of particles, or, equivalently, the density $\rho = M/L$. The evolution of the system is described by the following continuous-time stochastic dynamics:

- in a small interval dt a single particle is transported from site i with m_i particles to site $i + 1$ with probability $U(m_i)dt$, provided $m_i \geq 1$;
- nothing happens with probability $1 - U(m_i)dt$;

and here $U(m)$ is an arbitrary positive function with the condition $U(0) = 0$. As the system evolves under this dynamics, the probability of a given configuration $P(m_1, m_2, \dots, m_L, t)$ evolves in time and, when $t \rightarrow \infty$, it approaches a time-independent stationary joint distribution $P(m_1, m_2, \dots, m_L)$. Since every quantity of interest in the stationary state can, in principle, be computed by this distribution, it is our quantity of interest. In the ZRP problem, this quantity can be easily computed and assumes the simple factorized form:

$$P(m_1, m_2, \dots, m_L) = \frac{1}{Z_L} f(m_1) f(m_2) \dots f(m_L) \delta \left(\sum_{i=1}^L m_i - M \right) \quad (\text{C.1})$$

where the weight function $f(m)$ is defined as

$$f(m) = \begin{cases} \prod_{k=1}^m \frac{1}{U(m)} & \text{for } m \geq 1 \\ 1 & \text{for } m = 0 \end{cases} \quad (\text{C.2})$$

The delta function in Eq. (C.1) expresses the total mass conservation and $Z_L(M)$ is a normalization that ensures that the total probability is unity and satisfies

$$Z_L(M) = \sum_{m_i} \prod_{i=1}^L f(m_i) \delta \left(\sum_{i=1}^L m_i - M \right) \quad (\text{C.3})$$

Notice that Eq. (C.3) is identical to Eq. (2.15) and this is why we study ZRP problem in order to show how condensation works also in the DNLSE. Finally, we can obtain the single site mass distribution function as the marginal of the joint distribution probability:

$$p(m) = \sum_{m_2, m_3, \dots, m_L} P(m, m_2, m_3, \dots, m_L) = f(m) \frac{Z_{L-1}(M-m)}{Z_L(M)} \quad (\text{C.4})$$

C.2 Condensation in models with factorisable steady state

The factorization property Eq. (C.1) is quite general and is common to many models of interest. What follows does not depend on the particular model under scrutiny, but only on the form of the joint probability distribution. In particular, Eq. (C.1) allows us to find an easy criterion for a condensation transition

working in the Gran Canonical ensemble (GCE). Within this framework, it can be introduced a fugacity e^{-sm} , where s is the negative of the chemical potential associated with each site. This is equivalent to taking the Laplace transform of Eq. (C.1) with respect to M (s is the Laplace variable), which allow us to perform the integration, replacing the delta function by $e^{-s[m_1+m_2+\dots+m_L]}$. Then s is chosen such that the constraint $M = \sum m_i$ is satisfied. We obtain:

$$\tilde{P}(m_1, m_2, \dots, m_L) = \frac{1}{Z_L} f(m_1)e^{-sm_1} f(m_2)e^{-sm_2} \dots f(m_L)e^{-sm_L} \quad (C.5)$$

where \tilde{P} is the Laplace transform of P . Now each site has a mass distribution $p(m) = f(m)e^{-sm}$, and thus the equation that fixes the value of s for a given $M = \rho L$ is:

$$\rho = \rho_s \equiv \frac{\int_0^\infty dm m f(m) e^{-sm}}{\int_0^\infty dm f(m) e^{-sm}} \quad (C.6)$$

The criterion for condensation can be derived by analysing the function $\rho(s)$ defined in Eq. (C.6). If, for a given ρ , it can be found a solution to the equation $s = s^*$ such that the single site mass distribution is normalizable, i.e. $\int dm p(m) = \int dm f(m) \exp[-sm]$ is finite, then there is no condensation because, for all ρ , the single site mass distribution has an exponential tail and there is no special site that needs to lodge extra mass. On the other hand, it may be that, for some choices of $f(m)$, as one increases ρ , there may be a critical value ρ_C below which one finds a good solution s to Eq. (C.6), but such a solution no more exist for $\rho > \rho_C$. This will signal the onset of a condensation because for $\rho > \rho_C$, the system needs to break up into two parts: (a) a critical background, consisting of $(L - 1)$ sites with an average density which is critical (ρ_C) and (b) a single condensate site which contains the additional mass $(\rho - \rho_C)L$.

As an example, consider $f(m)$ that decays slower than an exponential, but faster than $1/m^2$ for large m . Because $f(m)$ decays slower than an exponential, the possible solution s^* of Eq. (C.6) can not be negative, in order that the single site mass distribution $p(m) = f(m)e^{sm}$ is normalizable (i.e. $\int dm p(m)$). Thus the the minimum possible solution is $s^* = 0$. As $s \rightarrow 0$, the function $\rho(s)$ in Eq. (C.6) approaches a critical value,

$$\rho_C = \rho(s \rightarrow 0) = \frac{\int_0^\infty dm m f(m)}{\int_0^\infty dm f(m)} \quad (C.7)$$

which is finite because we supposed that $f(m)$ decays faster than $1/m^2$ for large m . Therefore, as long as $\rho < \rho_C$, by solving Eq. (C.6) a positive solution s^* can be found and hence no condensation occurs. As $\rho \rightarrow \rho_C$ from below, $s^* \rightarrow 0$ from above. But for $\rho > \rho_C$, no positive solution s^* to Eq. (C.6) can be found, which signals the onset of a condensation transition.

A detailed analysis of Eq. (C.6) shows that, in order to have condensation, the weight function $f(m)$ must have a large m tail that lies above an exponential but below $1/m^2$, i.e.

$$e^{-cm} < f(m) < \frac{1}{m^2} \quad (\text{C.8})$$

for large m , with some positive constant $c > 0$.

C.3 Interpretation as sum of Random Variables

We have just seen how the condensation phenomenon occurs studying the behavior of the density ρ . The same results can be obtained considering the probability distribution for the sum of i.i.d. random variables. First we note that, if $f(m)$ is normalized, then $\prod_{i=1}^L f(m_i)$ is the probability that the L random variables assume the values m_1, m_2, \dots, m_L . Moreover we notice that the partition function defined as:

$$Z_L(M) = \sum_{m_i} \prod_{i=1}^L f(m_i) \delta \left(\sum_{i=1}^L m_i - M \right) \quad (\text{C.9})$$

(Eq.(C.3)) is the probability that the sum of the random variables equals M . Therefore, the problem of understanding the presence of condensation reduces to studying the behavior of the largest of the L random variables.

Let us introduce the momenta of the distribution, defined as

$$\mu_k = \int_0^\infty dm m^k f(m) \quad (\text{C.10})$$

If the mean of the distribution μ_1 exists and it happens that $L\mu_1 > M$, we expect that all the masses are of order $\mathcal{O}(1)$, while if $L\mu_1 < M$ then $L-1$ masses are of order $\mathcal{O}(1)$ and one is of order $\mathcal{O}(M)$. Thus we expect that, if $f(m) \sim m^{-\gamma}$ with $\gamma > 2$ there is condensation at the critical density $\rho_C = \mu_1$, exactly as we found in Eq. (C.7) and Eq. (C.8).

D | Generation of the basis elements for the Quantum DNLSE and the Hamiltonian

In Sec. (4) we introduced the quantum version of the DNLSE and we are interested in simulating the time evolution generated by the Hamiltonian Eq. (4.3). We pointed out that a natural choice of basis is the occupation number one. In order to generate all the basis element in the algorithm we have to find a way of ordering the elements of the basis. This can be done using the lexicographic order, as introduced in [26]. Given two different basis vectors $|n_1, n_2, \dots, n_N\rangle$ and $|n'_1, n'_2, \dots, n'_N\rangle$ there must exist an index $k \in [1, N - 1]$ such that $n_i = n'_i$ for $1 \leq i \leq k-1$ and $n_k \neq n'_k$. Therefore, we will say that $|n_1, n_2, \dots, n_{k-1}, n_k, \dots, n_N\rangle$ is superior (interior) to $|n_1, n_2, \dots, n_{k-1}, n'_k, \dots, n'_N\rangle$ if $n_k > n'_k$ ($n_k < n'_k$). Starting from the vector $|N_b, 0, \dots, 0\rangle$ we can build up the whole basis by means of the following procedure. Given the basis vector $|n_1, n_2, \dots, n_N\rangle$ with $n_N < N_b$ (otherwise it is the last element of the basis), the next basis vector is obtained with the following rule: suppose $n_k \neq 0$ while $n_i = 0 \forall k+1 \leq i \leq N-1$, then the next basis vector $|n'_1, n'_2, \dots, n'_N\rangle$ is such that:

- $n'_i = n_i \forall 1 \leq i \leq k - 1$;
- $n'_k = n_k - 1$;
- $n'_{k+1} = N_b - \sum_{i=1}^k n'_i$ and $n'_i = 0 \forall i \geq k + 2$.

In order to implement the Hamiltonian in matrix form, we have to build separately the interaction term and the hopping term. The first one is easy since it is diagonal in the basis of the eigenstates of the number operators \hat{n}_i (see code Listing (D.2)). The hopping term is instead more complicated, since it is not diagonal in the basis of the eigenstates of the number operator. The code shown in Listing (D.3) solves this problem; basically `kineticPart []` removes all the zero contribution to the hopping term. The function `opADagAState []` finds the components of $\psi_i^\dagger \psi_{i+1}$ and `opADagAValue []` calculates their coefficients. The final Hamiltonian is a sparse matrix and this code uses this property to make the calculations faster. This can be seen plotting the output of `getMatrix []`.

Listing D.1: Hamiltonian

```

1  getMatrix[basis_, couplingConst_] :=
2  With[{basisNumRange = Range@Length@basis},
3  SparseArray@
4  Join[kineticPart [basis, AssociationThread[basis -> basisNumRange],
5  basisNumRange],
6  interactionPart [basis, couplingConst, basisNumRange]]]

```

Listing D.2: Potential part

```

1  interactionPart [basis_, couplingConst_, basisNumRange_] :=
2  MapThread[{#1, #1} -> #2 &, {basisNumRange,
3  0.5*couplingConst*Sum[i*i, {i, #}]} & /@ basis}

```

Listing D.3: Hopping part

```

1  kineticPart [basis_, positionMap_, basisNumRange_] :=
2  Catenate@MapThread[
3  kineticPartMapFunc@{Apply[{positionMap[#1], #2} &,
4  DeleteCases[_ , 0.]} /@
5  Transpose[{opADagAState[basis], opADagAValue[basis]}, {3, 1,
6  2}], {2}], basisNumRange}
7  opADagAState[basis_] :=
8  With[{len = Length@First@basis},
9  Outer[Plus, basis, #, 1] &@
10 Catenate[
11 NestList[RotateRight, PadRight[#, len],
12 len - 1] & /@ {{1, -1}, {-1, 1}}]]
13 opADagAValue[basis_] :=
14 Sqrt[{#1 + 1.}*#2] & @@@ (Join[#, Reverse[#, {2}]]] &@
15 Partition [#, 2, 1, 1]) & /@ basis
16 kineticPartMapFunc[stateValuePairs_,
17 index_] := ({index, #1} -> #2) & @@@ stateValuePairs

```

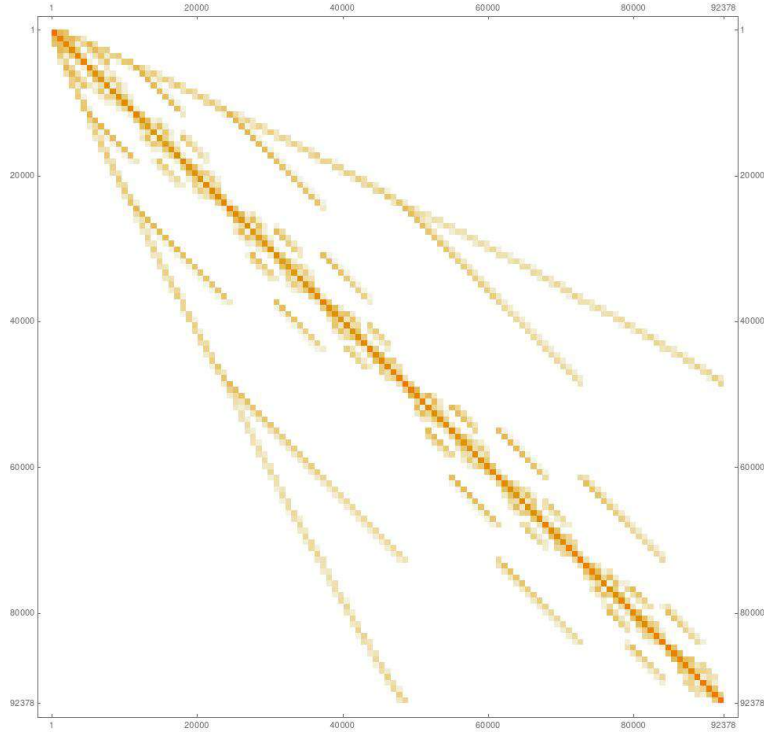


Figure D.1: A plot of the matrix form of the Hamiltonian produced by the code explained above. In this case we set the number of bosons $N_b = 10$ and the number of sites $N = 10$. The dimension of the Hilbert space is therefore $D_{\mathbb{H}} = 92378$. The coloured squares are the non-negative entries of the matrix, therefore it is evident that it is a sparse matrix.

In Sec. (4.2.1) we pointed out that, in order to study the dynamics of the 3-site system, we have to look into the quantity $n(k, t)$ defined in Eq. (4.16). To do this in our algorithm, we remind that the Hamiltonian is computed associating to each element of the basis $|n_1, n_2, n_3\rangle$ a vector of the form $(0, \dots, 0, 1, 0, \dots, 0)^T$. For example, for $N = 2$ and $N_b = 2$ we have:

$$\begin{aligned}
 |2, 0, 0\rangle &\rightarrow (1, 0, 0, 0, 0, 0)^T \\
 |1, 1, 0\rangle &\rightarrow (0, 1, 0, 0, 0, 0)^T \\
 |1, 0, 1\rangle &\rightarrow (0, 0, 1, 0, 0, 0)^T \\
 |0, 2, 0\rangle &\rightarrow (0, 0, 0, 1, 0, 0)^T \\
 |0, 1, 1\rangle &\rightarrow (0, 0, 0, 0, 1, 0)^T \\
 |0, 0, 2\rangle &\rightarrow (0, 0, 0, 0, 0, 1)^T
 \end{aligned}
 \tag{D.1}$$

Therefore, the result of the time evolution will be a normalized (the time evolution operator is unitary) linear superposition of vectors like $(0, \dots, 0, 1, 0, \dots, 0)^T$, that is a result of the form

$$\Phi(t) = \sum_{i=1}^{D_{\mathbb{H}}} \alpha_i(t) (0, \dots, 0, \underset{i\text{-th place}}{1}, 0, \dots, 0)^T \quad (\text{D.2})$$

with

$$\sum_{i=1}^{D_{\mathbb{H}}} |\alpha_i(t)|^2 = 1 \quad (\text{D.3})$$

and thus $|\alpha_i(t)|^2$ represents the probability that, at time t , the system is in the state $(0, \dots, 0, \underset{i\text{-th place}}{1}, 0, \dots, 0)^T$. Therefore the probability in Eq. (4.16) is:

$$p(n_1, n_2, n_3; t) = |\alpha_i(t)|^2 \quad (\text{D.4})$$

where the relation $(n_1, n_2, n_3) \leftrightarrow i$ is given by the ordering of the basis vectors, i.e. by associations as Eq. (D.1)

E | Reflection above a barrier

Here we will derive the formula Eq. (4.32) used to find the probability for charge transfer between two vertices of the simplex. This formula can be found in the book of Landau and Lifschitz [27], even though we will use an alternative derivation (proposed in [28]) that is more intelligible and that yields to the same result.

We will derive the formula Eq. (4.32) by transforming the problem of the reflection above a barrier in coordinate space to a problem of barrier penetration in momentum space. To this aim, we assume for simplicity that the potential is a symmetric function $V(x) = V(-x)$, so that $V_{\text{max}} = V(0)$ (as in our case). Let us consider the classical motion of a particle in the inverted harmonic potential (therefore $V(0) = 0$) and suppose that the particle is incident from the left with $E > 0$. As x increases toward zero, p decreases and reaches its minimum $p_0 = \sqrt{2mE}$ at $x = 0$. If it is transmitted, the momentum increases as it moves off to the right. Therefore the momentum at the beginning was large and positive, it became smaller while moving towards its minimum and then grew again to positive values. This means that the particle has been reflected from a barrier in momentum space located at p_0 . If, instead, the particle is reflected by the barrier in coordinate space, it must make a transition to negative momentum $-p_0$ and then continue to ever more negative momentum. The values of momentum between p_0 and $-p_0$ can not occur classically, and thus this transition occurs as a "tunnelling" in momentum space.

In order to derive Eq. (4.32), we write the Schrodinger equation in momentum space:

$$\left(\frac{p^2}{2m} + V \left(i\hbar \frac{d}{dp} \right) \right) \Phi(p) = E\Phi(p) \quad (\text{E.1})$$

and suppose that the WKB approximation is valid. We can write then:

$$\Phi(p) = \exp\left(\frac{i}{\hbar}\sigma(p) + \mathcal{O}(\hbar^0)\right) \quad (\text{E.2})$$

and substituting into Eq. (E.1) we get, at leading order in \hbar :

$$\frac{p^2}{2m} + V(x(p)) = E \quad (\text{E.3})$$

where $x(p) = -\frac{d\sigma}{dp}$. Solving for $\sigma(p)$ we get:

$$\sigma(p) = -\int^p dp' V^{-1}\left(E - \frac{p'^2}{2m}\right) \quad (\text{E.4})$$

In the classically forbidden region of momentum space, $-\sqrt{2mE} < p < \sqrt{2mE}$, the inverse function $V^{-1}(\xi)$ must be defined by analytic continuation from the domain $\xi < V_0$ where it is defined. Since the domain of $V(x)$ is the whole real axis, then the real part of $V^{-1}(\xi)$ vanishes when we are out of the classically allowed region. This means that V^{-1} is always imaginary in the classically forbidden region. Therefore, the probability of reflection above the barrier (in coordinate space) is the probability of barrier penetration in momentum space, that is obtained by integrating $\int dp x(p)$ from $-p_0$ to p_0 and choosing the sign of $x(p)$ that corresponds to exponential suppression:

$$|\mathcal{R}(E)|^2 = \exp\left(-\frac{2}{\hbar} \mathcal{I} \int_{-p_0}^{p_0} dp V^{-1}\left(E - \frac{p^2}{2m}\right)\right) \quad (\text{E.5})$$

In order to arrive at Eq. (4.32) we have to perform an integration by parts. In particular, let us remind that, for a generic z complex variable, we have $p(z) = \sqrt{2m(e - V(z))}$ and we define z_0 as the value of z in the upper-half z -plane for which $p(z_0) = 0$. For a symmetric potential with maximum at $x = 0$, z_0 is on the imaginary z -axis and thus we set $z_0 = iy_0$. We observe that the following integration by parts relation holds:

$$\int_0^{y_0} dy p(iy) = yp(iy) \Big|_0^{y_0} + \int_0^{p_0} dp y(p) \quad (\text{E.6})$$

The surface term vanishes because $p(iy_0) = 0$, while $p(0)$ is the classical momentum at $y = 0$, so $p(y = 0) = \sqrt{2mE} = p_0$. The function $y(p)$ is the solution to Eq. (E.3) with $x = iy$: $p^2/2m + V(iy) = E$ which means that

$y = -iV^{-1}(E - p^2/2m)$. Using these facts and substituting into Eq. (E.5) we find the desired result:

$$|\mathcal{R}(E)|^2 = \exp\left(-\frac{4}{\hbar} \mathcal{J} \int_0^{y_0} i dy p(iy)\right) = \exp\left(-\frac{4}{\hbar} \int_0^{y_0} dy \sqrt{2m(E - V(iy))}\right) \quad (\text{E.7})$$

that is the desired expression.

F | Microcanonical random variables

In this section we show that, if the random variables E_i 's are distributed with $p(E_i) = \beta e^{-\beta E_i}$, then the variables $x_i = \frac{E_i}{\sum_{i=1}^N E_i}$ are distributed with $\bar{p}(x_i) = \Gamma(N)\delta(1 - \sum_{i=1}^N x_i)$. This can be easily done by performing the mean value of a function $F = F\left(\frac{E_i}{E}\right)$:

$$\begin{aligned}
 \langle F \rangle &= \int d^N E \beta^N e^{-\beta E_F} \left(\frac{E_i}{E} \right) = \\
 &= \beta^N \int d^N E \int_0^\infty d\xi \delta\left(\xi - \sum_{i=1}^N E_i\right) e^{-\beta E_F} \left(\frac{E_i}{E} \right) = \\
 &= \beta^N \int_0^\infty d\xi \xi^{N-1} e^{-\beta \xi} \int d^N x \delta\left(1 - \sum_{i=1}^N x_i\right) F(x_i) = \\
 &= \Gamma(N) \int d^N x \delta\left(1 - \sum_{i=1}^N x_i\right) F(x_i)
 \end{aligned} \tag{F.1}$$

as we wanted to show. Notice for instance that, if we choose $F(x_i)$ as the constant function $F(x_i) = 1$ we get the useful formula:

$$\frac{1}{\Gamma(N)} = \int d^N x \delta\left(1 - \sum_{i=1}^N x_i\right) \tag{F.2}$$

F.1 An application

As an example, let us give a rough estimate for the probability of having two breathers in a microcanonical configuration of variables, compared with the

probability of having only one breather. We have just seen that microcanonical variables are obtained via an exponential distribution. Suppose then to have variables x_i distributed as:

$$P(x) = e^{-x}, \quad x > 0 \quad (\text{F.3})$$

We wonder what is the probability for the sum of N such random variables, i.e. what is the probability that their sum is equal to λN . This is easily obtained performing:

$$P_N(\lambda) = \int \prod_{i=1, N} dx_i \delta\left(\sum_{i=1, N} x_i - N\lambda\right) e^{-\sum_{i=1, N} x_i} \quad (\text{F.4})$$

Using Eq. (F.2) this is easily done and we get:

$$P_N(\lambda) = \frac{(N\lambda)^{N-1}}{(N-1)!} e^{-N\lambda} \quad (\text{F.5})$$

Therefore, the probability of getting $N - 1$ variables of order $\mathcal{O}(1)$ and one variable of order $\mathcal{O}(N)$ is given by Eq. (F.5) with $\lambda \simeq 2$, while the probability of getting $N - 2$ variables of order $\mathcal{O}(1)$ and two variables of order $\mathcal{O}(N)$ is obtained setting $\lambda' \simeq 3$. The second case is thus suppressed with respect to the first by a factor e^{-N} :

$$p(2 \text{ breathers}) \simeq \left(\frac{\lambda'}{\lambda}\right)^{N-1} p(1 \text{ breather}) e^{-N(\lambda' - \lambda)} \quad (\text{F.6})$$

Bibliography

- [1] E. Fermi, P Pasta, S Ulam, and M Tsingou. Studies of the nonlinear problems.
- [2] Giacomo Gradenigo, Stefano Iubini, Roberto Livi, and Satya N. Majumdar. Localization in the discrete non-linear schrödinger equation: mechanism of a first-order transition in the microcanonical ensemble, 2019.
- [3] Manuel Pino, Lev B. Ioffe, and Boris L. Altshuler. Nonergodic metallic and insulating phases of josephson junction chains. *Proceedings of the National Academy of Sciences*, 113(3):536–541, 2016.
- [4] P. W. Anderson. Absence of diffusion in certain random lattices. *Phys. Rev.*, 109:1492–1505, Mar 1958.
- [5] Antonello Scardicchio and Thimothée Thiery. Perturbation theory approaches to anderson and many-body localization: some lecture notes, 2017.
- [6] Rahul Nandkishore and David A. Huse. Many-body localization and thermalization in quantum statistical mechanics. *Annual Review of Condensed Matter Physics*, 6(1):1538, Mar 2015.
- [7] C. Sulem and P.L. Sulem. *The Nonlinear Schrödinger Equation: Self-Focusing and Wave Collapse*. Applied Mathematical Sciences. Springer New York, 1999.
- [8] Vladimir Evgen'evich Zakharov. Collapse and self-focusing of langmuir waves. 1983.

- [9] Miguel Onorato, Alfred R. Osborne, Marina Serio, and Serena Bertone. Freak waves in random oceanic sea states. *Phys. Rev. Lett.*, 86:5831–5834, Jun 2001.
- [10] R. Morandotti, H. S. Eisenberg, Y. Silberberg, M. Sorel, and J. S. Aitchison. Self-focusing and defocusing in waveguide arrays. *Phys. Rev. Lett.*, 86:3296–3299, Apr 2001.
- [11] R. Morandotti, U. Peschel, J. S. Aitchison, H. S. Eisenberg, and Y. Silberberg. Dynamics of discrete solitons in optical waveguide arrays. *Phys. Rev. Lett.*, 83:2726–2729, Oct 1999.
- [12] H. S. Eisenberg, Y. Silberberg, R. Morandotti, and J. S. Aitchison. Diffraction management. *Phys. Rev. Lett.*, 85:1863–1866, Aug 2000.
- [13] D. Mandelik, R. Morandotti, J. S. Aitchison, and Y. Silberberg. Gap solitons in waveguide arrays. *Phys. Rev. Lett.*, 92:093904, Mar 2004.
- [14] Nikos K. Efremidis, Suzanne Sears, Demetrios N. Christodoulides, Jason W. Fleischer, and Mordechai Segev. Discrete solitons in photorefractive optically induced photonic lattices. *Phys. Rev. E*, 66:046602, Oct 2002.
- [15] Segev M. Efremidis N. et al. Fleischer, J. Observation of two-dimensional discrete solitons in optically induced nonlinear photonic lattices. *Nature*, 422:147–150, 2003.
- [16] S Burger, F. S Cataliotti, C Fort, P Maddaloni, F Minardi, and M Inguscio. Quasi-2d bose-einstein condensation in an optical lattice. *Europhysics Letters (EPL)*, 57(1):16, Jan 2002.
- [17] S Iubini, R Franzosi, R Livi, G-L Oppo, and A Politi. Discrete breathers and negative-temperature states. *New Journal of Physics*, 15(2):023032, feb 2013.
- [18] K. Ø. Rasmussen, T. Cretegny, P. G. Kevrekidis, and Niels Grønbech-Jensen. Statistical mechanics of a discrete nonlinear system. *Phys. Rev. Lett.*, 84:3740–3743, Apr 2000.
- [19] Thudiyangal Mithun, Yagmur Kati, Carlo Danieli, and Sergej Flach. Weakly nonergodic dynamics in the gross-pitaevskii lattice. *Phys. Rev. Lett.*, 120:184101, May 2018.

- [20] M. R. Evans, Satya N. Majumdar, and R. K. P. Zia. Canonical analysis of condensation in factorised steady states. *Journal of Statistical Physics*, 123(2):357390, Apr 2006.
- [21] Thudiyangal Mithun, Carlo Danieli, Yagmur Kati, and Sergej Flach. Dynamical glass and ergodization times in classical josephson junction chains. *Phys. Rev. Lett.*, 122:054102, Feb 2019.
- [22] Alexander Yu. Cherny, Thomas Engl, and Sergej Flach. Non-gibbs states on a bose-hubbard lattice. *Phys. Rev. A*, 99:023603, Feb 2019.
- [23] K. Ø. Rasmussen, T. Cretegny, P. G. Kevrekidis, and Niels Grønbech-Jensen. Statistical mechanics of a discrete nonlinear system. *Phys. Rev. Lett.*, 84:3740–3743, Apr 2000.
- [24] Juraj Szavits-Nossan, Martin R Evans, and Satya N Majumdar. Condensation transition in joint large deviations of linear statistics. *Journal of Physics A: Mathematical and Theoretical*, 47(45):455004, Oct 2014.
- [25] Satya N. Majumdar. Real-space condensation in stochastic mass transport models, 2009.
- [26] J M Zhang and R X Dong. Exact diagonalization: the bosehubbard model as an example. *European Journal of Physics*, 31(3):591602, Apr 2010.
- [27] L.D. Landau and E.M. Lifshitz. *Quantum Mechanics (Volume 3 of A Course of Theoretical Physics)*. 1965.
- [28] R. L. Jaffe. Reflection above the barrier as tunneling in momentum space. *American Journal of Physics*, 78(6):620623, Jun 2010.